Dissertation ETH Number 18292

Magnetic Field Assisted Biomaterials Processing

A dissertation submitted to the

Swiss Federal Institute of Technology Zurich

for the degree of

Doctor of Sciences

presented by

Paul Beck

Dipl.-Ing. ETH Zurich

born March, 29, 1979

citizen of Switzerland

accepted on the recommendation of

Prof. Erich J. Windhab, examiner

Prof. Peter Walde, Dr. Peter Fischer and Dr. Joachim Kohlbrecher, co-examiner

2009

Magnetic Field Assisted Biomaterials Processing

To my parents and my sister

Earthlings had to figure it all out for themselves. Slowly, agonizingly, humans learned how the universe worked, abandoning most of the fanciful beliefs they carried through their long, dark loneliness.

Brightness Reef, by David Brin (1995)

Acknowledgments

Als Erstes möchte ich mich bei meinem Doktorvater Prof. Erich J. Windhab bedanken. Prof. Windhab hat mir viel wissenschaftlichen Freiraum gelassen und mich immer unterstützt, meine Ideen zu verwirklichen. Seine Visionen und Anregungen haben mich sehr motiviert. Besonders danke ich Prof. Windhab für die Erlaubnis und Unterstützung, neben der Doktorarbeit ein Nachdiplomstudium in Wirtschaft zu absolvieren.

Prof. Peter Walde, Dr. Peter Fischer und Dr. Joachim Kohlbrecher danke ich bestens für die Übernahme des Korreferats. Prof. Walde hat mich in die faszinierende Welt der Vesikel und der Self-Assembly Systems im Allgemeinen eingeführt und mich an seinem breiten Wissen und seiner grossen Erfahrung teilhaben lassen. Ich danke ihm für die vielen spannenden Diskussionen und auch für die Möglichkeit, sein Labor zu nutzen. Dr. Peter Fischer danke ich für die Betreuung meiner Arbeit. Die Tür zu ihm war jederzeit offen für ein Gespräch und seine unkomplizierte Art, Probleme aus der Welt zu schaffen, hat mich immer wieder erfreut. Dr. Joachim Kohlbrecher bin ich dankbar für die Geduld, mit der er mir wiederholt die Theorie hinter der Neutronenstreuung erklärte, bis am Schluss tatsächlich etwas hängen blieb. Ebenfalls danke ich ihm für die Hilfe beim Fitten der SANS Daten. Es waren auch die SANS Versuche, die den ersten Magnetfeld-Effekt zu Tage förderten.

Während dieser Arbeit war ich auf die Unterstützung anderer Institute angewiesen. Prof. Takashi Ishikawa danke ich für die tollen cryo-TEM Aufnahmen. Besonders diejenigen, die in der Kälte des Kühlraumes entstanden. Dr. Heinz Rüegger danke ich bestens für die Hilfe und Unterstützung bei den NMR Messungen. Martin Colussi danke ich für die Hilfe bei den DSC Messungen. Dr. Helmut Zepik danke ich für die Hilfe bei der Synthese meiner Wunschmoleküle.

Der Aufbau des Magnetlabors wäre ohne die Hilfe von Daniel Kiechl, Jan Corsano, Bruno Pfister und Peter Bigler nicht möglich gewesen. Ich habe viel von ihnen gelernt und konnte mich immer auf sie verlassen. Dafür danke ich ihnen ganz herzlich. Bernhard Koller danke ich für die IT-Unterstützung.

Ich möchte mich auch beim gesamten VT Team für die tolle Arbeitsatmosphäre bedanken. Ich habe den Humor und die angeregten Diskussionen bei Kaffeepausen und Mittagessen sehr genossen. Besonderer Dank für die Freundschaft geht an meine beiden Bürogenossen, Muriel Graber und André Braun.

Ich hatte viel Glück mit "meinen" StudentInnen und Hilfswissenschafter, denen ich sehr dankbar bin für Ihre tatkräftige Mitarbeit. Es sind Eric Egli, Erich Staubli, Melanie Wagner und Marianne Liebi. Es freut mich sehr, dass Marianne Liebi mein Nachfolgeprojekt übernehmen wird. Ich wünsche ihr alles Gute und viel Erfolg dabei.

Ganz besonders bin ich meiner Mutter, meinem Vater und meiner Schwester für ihre Unterstützung und ihr Vertrauen dankbar.

Contents

List of Figures

List of Figures

List of Tables

Notation

Latin Symbols

Symbol	Unit	Denotation
$A_{sphere\ cap}$	nm^2	area of sphere cap shaped domain
A_{oblate}	nm^2	area of an oblate vesicle
B	G ($=10^{-4}$ T)	magnetic flux density
d	nm	vesicle membrane thickness
K	dyne	membrane bending elastic modulus
E_M	J	magnetic energy
E_T	J	thermal energy
H	Oe	magnetic field strength
I	cm^{-1}	neutron scattering intensity
I_{cycl}	cm^{-1}	neutron scattering intensity of a flat cylinder
J_1		first order Bessel function of the first kind
k	erg k^{-1}	Boltzmann constant
L	nm	length of cylinder / thickness of bilayer
L_α		liquid disordered phase of phospholipids
$L_{\beta'}$		solid ordered phase of phosopholipids
N		aggregation number
$\vec{n}$		cylinder axis
P_L		Legendre polynomial

Symbol	Unit	Denotation
Q	Å^{-1}	neutron momentum transfer
q	Å^{-1}	neutron momentum transfer
Q_0		cumulative size distribution
q_0		probability density function
$\vec{q}$		scattering vector
R	nm	vesicle radius
R	nm	bicelle radius
r	nm	vesicle radius
R_0	nm	bicelle radius
r_d	nm	domain radius
r_G	nm	radius of gyration
r_H	nm	hydrodynamic radius
r_s	nm	vesicle short radius (in direction of domain)
r_v	nm	vesicle radius
T_m	°C	phase transition temperature of phospholipids
III		cocoa butter crystal form

Greek Symbols

Symbol	Unit	Denotation
α		cocoa butter crystal form
β_{IV}		cocoa butter crystal form
β_{V}		cocoa butter crystal form
β_{VI}		cocoa butter crystal form
η	cm^{-2}	scattering length density
$\Delta\chi$	$erg\ cm^{-3}\ G^2$	diamagnetic anisotropy
$\chi_{\parallel}$	$erg\ cm^{-3}\ G^2$	diamagnetic susceptibility parallel to MF
$\chi_{\perp}$	$erg\ cm^{-3}\ G^2$	diamagnetic susceptibility perpendicular to MF
γ		cocoa butter crystal form
γ	rad	orientation relative to scattering vector
κ	J	membrane curvature energy
θ, ϕ	rad	polar coordinates of cylinder axis
ψ		scattering vector in the plane of the detector

Abbrevations

Symbol	Denotation
Ce	cerium
CHAPSO	3-[(3-cholamidopropyl)dimethylammonio]-2-hydroxy-1-propanesulfonate
cryo-TEM	cryo transmission electron microscopy
DHPC	1,2-dihexanoyl-*sn*-glycero-3-phosphocholine
DLS	dynamic light scattering
DMPC	1,2-dimyristoyl-*sn*-glycero-3-phosphocholine
DMPG	1,2-dimyristoyl-*sn*-glycero-3-[phospho-rac-(1-glycerol)]
DMPE-DTPA	1,2-dimyristoyl-*sn*-glycero-3-phosphoethanolamine diethylene triamine pentaacetate

Symbol	Denotation
DSC	differential scanning calorimetry
Dy	dysprosium
Er	erbium
Eu	europium
Ho	holmium
La	lanthanum
MeOH	methanol
MF	magnetic field
Na	sodium
Nd	neodymium
NMR	nuclear magnetic resonance
PEEK	polyetheretherketone
POPC	1-palmitoyl-2-oleoyl-sn-glycero-3-phosphocholine
POPE-DTPA	1-palmitoyl-2-oleoyl-sn-glycero-3-phosphoethanolamine diethylene triamine pentaacetate
Pr	praseodymium
SANS	small angle neutron scattering
Sm	samarium
SOPE-DTPA	1-stearoyl-2-oleoyl-sn-glycero-3-phosphoethanolamine diethylene triamine pentaacetate
TAC	triacylglycerol
Tb	terbium
Tm	thulium
Yb	ytterbium
2D	two-dimensional
3D	three-dimensional

Abstract

Within the scope of this work, a magnet rheometer laboratory was set up and used to investigate the influence of strong magnetic fields on biomolecular assemblies formed by two types of glycerol based lipids. The first was the triacylglyceride mixture of cocoa butter, the second was phosphatidylcholine forming vesicles and bicelles. The experiments made in the magnet rheometer laboratory were complemented by SANS measurements under magnetic field, ^{31}P-NMR, differential scanning calorimetry (DSC), dynamic light scattering (DLS), and cryo transmission electron microscopy (cryo-TEM). Molecular assemblies are more promising to react to magnetic fields than individual molecules, because the randomizing thermal fluctuation, kT, is much larger than the magnetic energy acting on a single molecule.

The magnet rheometer set up consisted of a superconductive magnet with a shear cell in the bore. A rheometer was positioned above the magnet and connected to the shear cell over a prolonged shaft. A laser beam was passed through the shear gap and the intensity was logged.

In the first part of this work, the crystallization dynamics of cocoa butter under shear were investigated with and without magnetic field by monitoring the decrease of laser intensity as well as the increase in viscosity. Additionally, crystal transformation of unsheared samples with and without magnetic field was investigated with differential scanning calorimetry (DSC). At the conditions tested, no significant magnetic field effect on cocoa butter was found. Possible reasons are discussed.

The second part of this work deals with magnetic field effects on two different phospholipid structures, vesicles and bicelles. Phospholipids are amphiphilic molecules forming self-assembly systems in water and are important components of biological membranes. Vesicles are self-closed phospholipid bilayers with a spherical shape, and are used as a model system to study physico-chemical properties of lipid membranes. In particular lipid rafts and domain formation on vesicles have received a lot of attention in recent research. Bicelles, which have the shape of small disks, are usually formed by mixtures of long and short chain phospholipids and are of interest as membrane mimics for the study of membrane proteins with NMR-spectroscopy.

In this work magnetic fields were used as a structuring force on such phospholipid systems using paramagnetic lanthanide ions as magnetic handles. Different lipid mixtures in concentration of 15 mM were studied with SANS in magnetic fields of up to 8 T and temperatures from 2.5 °C to 30 °C. The same samples were analyzed with Cryo-TEM, and were frozen from two different temperatures (5 °C and 22 °C). Additional information was gained by ^{31}P-NMR spectroscopy, DLS, and permeability measurements with and without magnetic fields of calcein, a water soluble fluorescence marker.

A number of different vesicle formulations was investigated. The basic sample consisted of a mixture of the phospholipid 1-palmitoyl-2-oleoyl-*sn*-glycero-3-phosphocholine (POPC) and a chelator lipid, 1,2-dimyristoyl-*sn*-glycero-3-phospho-ethanolamine-diethylene-triamine-pentaacetate (DMPE-DTPA) with complexed lanthanides. In addition to the commercially available DMPE-DTPA, two other chelator lipid were synthesized in house and used to form vesicles: 1-stearoyl-2-oleoyl-*sn*-glycero-3-phospho-ethanolamine-diethylene-triamine-pentaacetate (SOPE-DTPA), and 1-palmitoyl-2-oleoyl-*sn*-glycero-3-phospho-ethanolamine-diethylene-triamine-pentaacetate (POPE-DTPA). Domain formation was observed on small unilamellar vesicles consisting of POPC and a chelator lipid, DMPE-DTPA with complexed lanthanides. Lipid segregation was temperature dependent and the solid domains were orientable in magnetic fields. Parallel orientation of the domain normal to the magnetic field was observed if thulium was used and perpendicular orientation if dysprosium was used. The orientation of phospholipid domains could help to examine such domains with SANS without the need of chain-deuterated phospholipids.

One formulation consisting of a mixture of 1,2-dimyristoyl-*sn*-glycero-3-phosphocholine (DMPC) and DMPE-DTPA with complexed lanthanides did not yield vesicles, but formed bicelles. The bicellar system reported here formed without the need of a short chain lipid to cover the edges. In order to obtain bicelles with a diameter of about 40 nm, extrusion through membranes with a pore size of 100 nm was important. Cooling the sample for several hour to about 5 °C caused an increased monodispersity of the bicelle size. It is assumed that DMPC builds the planar center of such bicelles, whereas DMPE-DTPA with a complexed lanthanide forms the highly curved edge of the disk, due to the large head group of this molecule. SANS fits with a model for partly aligned flat cylinders indicate that bicelles containing thulium are slightly orientable in a magnetic field of 8 T with the bilayer normal parallel to the magnetic field.

Kurzfassung

Im Rahmen dieser Arbeit wurde ein Magnet-Rheometer-Labor aufgebaut und verwendet, um den Einfluss starker Magnetfelder auf Biomoleküle zu untersuchen. Es wurden Versuche mit zwei verschiedenen Arten von Glycerin-basierten Lipiden durchgeführt. Als Erstes wurde ein Gemisch von Triacylglyceriden in der Form von Kakaobutter und als Zweites Vesikel und Bicellen bestehend aus Phosphatidylcholin untersucht. Die Experimente, welche mit dem Magnet-Rheometer durchgeführt wurden, wurden ergänzt durch Kleinwinkel-Neutronenstreuung im Magnetfeld (SANS), ^{31}P-NMR-Spektroskopie, Dynamische Differenzkalorimetrie (DSC), Dynamische Lichtstreuung (DLS) und Cryo-Transmissionselektronenmikroskopie (Cryo-TEM). Magnetfelder haben praktisch keinen Einfluss auf einzelne Moleküle, da die thermische Fluktuation, kT, viel höher ist als die magnetische Energie des Einzelmoleküles. Aus diesem Grund wurden Molekülaggregate untersucht.

Der Magnet-Rheometer-Aufbau besteht aus einem Supraleitmagneten mit einer Scherzelle in der Bohrung. Ein Rheometer wurde über der Magnetbohrung positioniert und über einen verlängerten Schaft mit der Scherzelle verbunden. Ein Laserstrahl passiert den Scherspalt und die Intensität wird aufgezeichnet. Als Erstes wurde die Kristallisationskinetik von Kakaobutter unter Scherung mit und ohne Magnetfeld untersucht, indem die Abnahme der Laserintensität, sowie die Zunahme der Viskosität über der Zeit verfolgt wurde. Zusätzlich wurde die Umkristallisation von Kakaobutter mit und ohne Magnetfeld mit DSC untersucht. Unter den untersuchten Bedingungen wurde kein signifikanter Effekt des Magnetfeldes beobachtet. Mögliche Gründe dafür werden diskutiert.

Der zweite Teil dieser Arbeit behandelt Magnetfeld-Effekte auf Phospholipid-Strukturen. Phospholipide sind amphiphile Moleküle, die sich in Wasser zu Aggregaten zusammenlagern und den Hauptbestandteil von biologischen Membranen ausmachen. Zwei Arten von Phospholipid-Aggregaten- Vesikel und Bicellen- wurden in dieser Arbeit untersucht. Vesikel sind in sich geschlossene Lipid-Doppelschichten, die als Modellsysteme zur Untersuchung der physikalisch-chemischen Eigenschaften von Lipidmembranen dienen. Insbesondere die Domänenbildung in Vesikeln findet grosse Beachtung in der aktuellen Forschung. Bizellen sind scheibenförmige Phospholipidaggregate, welche in der Regel aus einer Mischung kurz- und langkettiger Phospho-

lipide bestehen. Sie werden in der NMR-Spektroskopie als Membranimitation zur Untersuchung von Membranproteinen verwendet.

In dieser Arbeit wurde untersucht, ob magnetische Felder solche Phospholipidsysteme, versetzt mit paramagnetischen Lanthaniden, beeinflussen können. Verschiedene Lipidmischungen in einer Konzentration von 15 mM wurden mit Kleinwinkelneutronenstreuung (SANS) in einem magnetischen Feld von bis zu 8 T und Temperaturen von 2.5 °C bis 30 °C untersucht. Von den selben Proben wurden Cryo-TEM-Aufnahmen gemacht, wofür die Proben bei zwei verschiedenen Temperaturen (5 °C und 30 °C) eingefroren worden waren. Zusätzliche Informationen wurden durch Permeabilitätsmessungen mit und ohne Magnetfeld, ^{31}P-NMR Spektroskopie und DLS gewonnen.

Es wurde eine Reihe von Vesikel-Formulierungen untersucht. Die Grundformulierung war Vesikel bestehend aus den Phospholipiden 1-Palmitoyl-2-Oleoyl-*sn*-Glycero-3-Phosphocholin (POPC) und 1,2-Dimyristoyl-*sn*-Glycero-3-Phosphoethanolamin-Diethylentriaminpentaessigsäure (DMPE-DTPA). Zusätzlich zum käuflichen Chelator-Lipid DMPE-DTPA wurden im Rahmen dieser Arbeit zwei weitere Chelator-Lipide synthetisiert und für die Herstellung von Vesikeln verwendet: 1-Stearoyl-2-Oleoyl-*sn*-Glycero-3-Phosphoethanolamin-Diethylentriaminpentaessigsäure (SOPE-DTPA) und 1-Palmitoyl-2-Oleoyl-*sn*-Glycero-3-Phosphoethanolamin-Diethylentriaminpentaessigsäure (POPE-DTPA). In Vesikeln bestehend aus POPC und DMPE-DTPA mit komplexierten Lanthaniden wurde Domänenbildung beobachtet. Die Domänen bildeten sich durch temperaturabhängige Lipid-Entmischung und waren in magnetischen Feldern orientierbar. Mit komplexiertem Thulium war die Orientierung der Domänen-Normalen parallel, mit Dysprosium senkrecht zum magnetischen Feld. Diese Orientierung von Phospholipiddomänen könnte deren Untersuchung mit SANS vereinfachen, weil auf den Einsatz von deuterierten Lipiden verzichtet werden kann.

Eine der untersuchten Formulierungen, eine Mischung aus DMPC und DMPE-DTPA mit komplexierten Lanthaniden, bildete keine Vesikel, sondern Bizellen. Dieses bizelläre System benötigt keine kurzkettigen Lipide, um die Ränder abzudecken. Für die Herstellung entscheidend war eine Extrusion durch Membranen mit einer Porengrösse von 100 nm. Eine mehrstündige Abkühlung der Probe auf 5 °C führte zu einer erhöhten Monodispersität der Bizellengrösse. Es wird vermutet, dass DMPC das planare Zentrum der Bizellen bildet, während sich DMPE-DTPA mit komplexierten Lanthaniden aufgrund der grossen Kopfgruppe in den stark gekrümmten Rändern befindet. SANS-Kurven konnten mit einem Modell für teilweise ausgerichtete flache Zylinder gefittet werden. Dies zeigt, dass Bizellen mit Thulium in einem magnetischen Feld von 8 T leicht orientiert sind, mit der Flächennormalen parallel zum magnetischen Feld.

1 Introduction

The general scope of this work is the use of strong magnetic fields as a structuring force on biomolecules. While biomolecules are generally considered not magnetic, they do exhibit a weak form of magnetism, called diamagnetism. Magnetism as experienced in daily life with ferromagnetic materials such as iron is a rare phenomenon and applies to only about 1 % of all known compounds (Maret and Dransfeld, 1985). Magnetic fields however do interact with all matter.

Maybe the most dramatic proof of magnetic field interaction with biological molecules is an effect called diamagnetic levitation. In strong magnetic fields with a very strong gradient, any diamagnetic system, such as a drop of water, a strawberry, or even a living organism can begin to hover in mid air. The magnetic field induces a gyration in the orbits of the electrons of diamagnetic materials, creating small persistent currents which oppose the external magnetic field (Yamaguchi and Tanimoto, 2006). Diamagnetic levitation is achieved when the repulsive force imposed by the magnetic field equals the gravitational force. Fig. 1.1 shows a flying frog inside the bore of a 16 T magnet (Simon and Geim, 2000). Such strong magnetic field gradients are used to simulate micro- or zero gravity on earth. As an example, they have been used to crystallize proteins in a free floating water droplet (Wakayama, 2003). The quality of the crystals was significantly enhanced, mainly due to two advantages of micro gravity environment: Natural convection due to density differences in the sample is damped, and no heterogeneous crystallization can be induced from a container wall.

In homogeneous magnetic fields, diamagnetic molecules are not repulsed, but try to adopt a minimal energy level by orienting themselves inside the magnetic field in a position where the electron shell experiences least interaction with the magnetic field. This is because diamagnetic molecules usually have anisotropic magnetic susceptibilities (Hong, 1995). For example, the diamagnetic susceptibility of phosphatidylcholine is larger along the long molecular axis than perpendicular to it. It will therefore exhibit a preferred orientation with the long molecular axis perpendicular to the magnetic field. While such orientation is not observed for individual molecules due to the disorienting thermal fluctuation energy kT, in self-assembly systems, where molecules are oriented parallel to each other, the magnetic orientation energy of each molecule is summed up, and can overcome the disorienting Brownian motion (Qiu
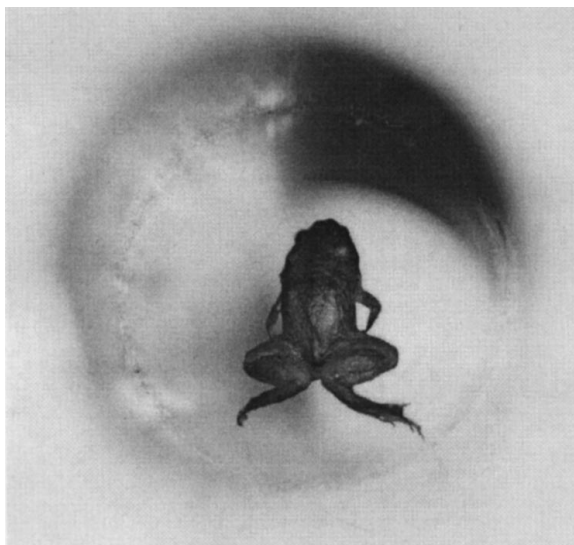
Figure 1.1: Diamagnetic levitation, experienced by a frog in the bore of an 18 T magnet (Simon and Geim, 2000).

et al., 1993). This effect is called magnetic orientation. It has been observed for a number of diamagnetic crystals, polymer gels, liquid crystals and carbon nanotubes (Katsaras *et al.*, 2005; Yamaguchi and Tanimoto, 2006). One application of magnetic orientation is the use of magnetically aligned lamellar sheets consisting of long and short chain phospholipids as a medium for structure determination of membrane proteins by solid-state NMR spectroscopy (e.g. De Angelis and Opella (2007)). Another application is the enhancement of crystal quality in homogeneous magnetic fields, which is thought to be due to parallel orientation of merging and knitting subcrystals (Lin *et al.*, 2000).

In this work, the effects of magnetic fields on two types of lipidic biomolecular systems were investigated. The first was cocoa butter, which consists mainly of triacylglycerides. A few dispersed observations and results can be found in literature, which may suggest a magnetic field effect on the crystallization behavior of cocoa butter and pure triacylglycerides. Magnetic field controlling of cocoa butter crystallization would be of great interest to industry, because conventional tempering of cocoa butter melts is an energy and time consuming process. To obtain more fundamental information on the subject, cocoa butter melts were exposed to homogeneous static magnetic fields during crystallization with or without superimposed shear flow fields. Of interest was whether the magnetic field can influence crystallization kinetics or the crystal quality.

The second system consisted of self-assembly structures composed of phospholipids. Phospholipids can form a variety of structures, depending on the experimental conditions used. Here, vesicles with a diameter of around 100 nm were used, consisting of a self-enclosed phospholipid bilayer. In order to enhance the responsiveness of the vesicles to magnetic fields, modified phospholipids with complexed lanthanide ions were interspersed into the membrane. A variety of different vesicle formulations and experimental conditions were tested. One formulation was found, which did not yield vesicular structures, but a novel disk-like structure. This structure was also investigated in more detail.

The work reported here is organized in seven chapters. The second chapter gives background information about the work presented in chapters three to six. The third chapter describes an experimental set up which was created to act on liquid samples via a flow field and/or a magnetic field, allowing on line gathering of information on sample properties. The fourth chapter describes the crystallization experiments under magnetic field of cocoa butter. The fifth chapter reports on the effects of magnetic fields on lanthanide doped phospholipid vesicles. The sixth chapter reports on the disk shaped nano structure and its behavior in magnetic fields. The four main chapters, three to six, are each presented with an own introduction and materials and methods section and should be understandable if read individually.

2 Background

2.1 Phospholipids: Chemical Structure and Phase Transition

Phospholipids are important components of biological membranes. Artificial phospholipid bilayers are a widely studied system in medicinal and biological research as mimics of biological membranes or as system used for drug delivery. The phospholipids used in this work are phosphatidylcholines. They are amphiphilic lipids in which two hydrophobic acyl hydrocarbon chains are linked by a glycerol backbone with the hydrophilic head group. In case of phosphatidylcholine the polar head group consists of phosphocholine (see Fig. 2.1).
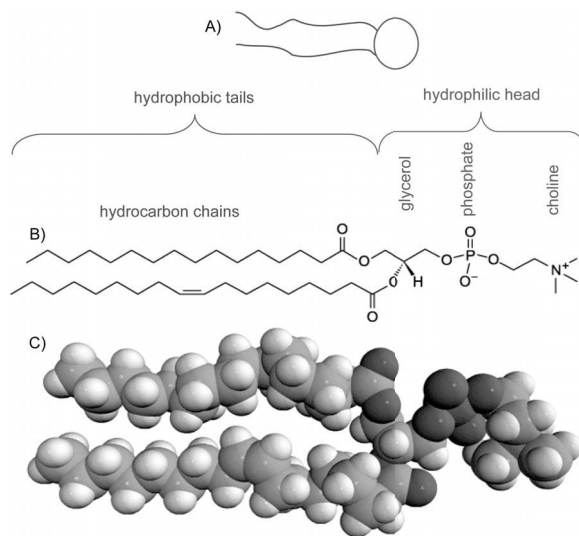
Figure 2.1: Phospholipid symbol (A), structural formula (B) and space-filling model(C) of a phosphatidylcholine. (http://www.avantilipids.com)

A phospholipid which is present in biological membranes and often used for vesicle preparation is 1-palmitoyl-2-oleoyl-*sn*-glycero-3-phosphocholine (POPC). POPC is a

long chain phosphatidylcholine with one saturated (palmitoyl, 18:0) and one unsaturated (oleoyl, 18:1) fatty acid (Walde and Ichikawa, 2001). For the chemical structure see table 2.1. POPC is the main phospholipid used in this work.

The main phase transition temperature of phospholipid membranes T_m is the transition from the crystalline-analogue state, also called gel or $L_{\beta'}$ phase, to the liquid-analogue state, also called liquid-crystalline or L_α phase. As shown in Fig. 2.2 the fatty acids are in a extended all *trans* conformation below T_m. Above the main phase transition temperature the lipid chains are rather disordered making the bilayer fluid (Walde and Ichikawa, 2001).
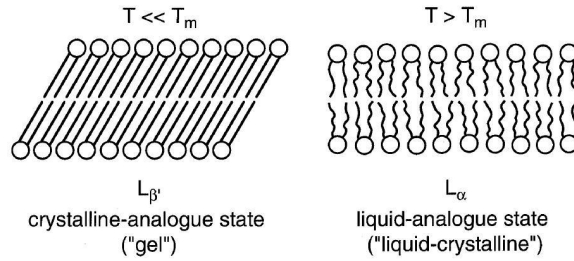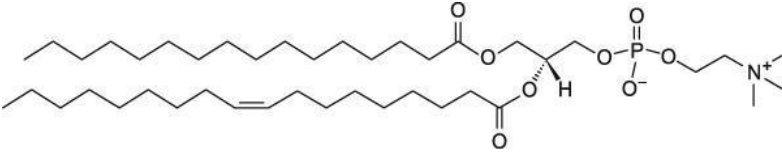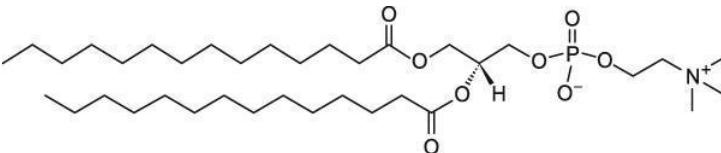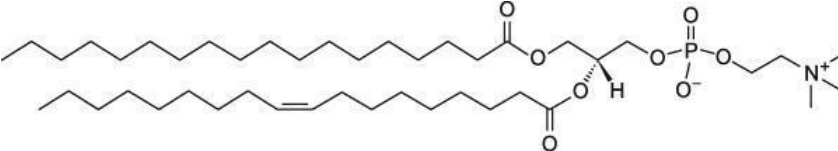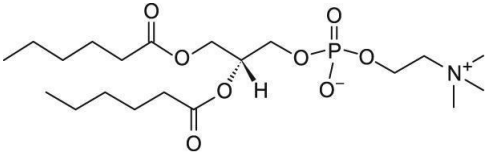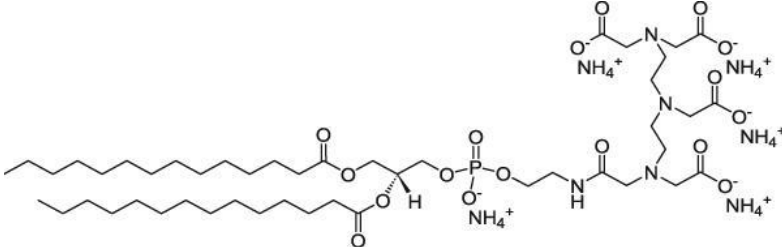
Figure 2.2: Schematic illustration of the phospholipid arrangement in a planar bilayer below and above the main phase transition temperature T_m (Walde and Ichikawa, 2001).

The phase transition temperature is strongly influenced by the chain length of the lipids. The longer the hydrocarbon chain, the higher is T_m. Furthermore T_m is affected by the degree of unsaturation: the phase transition temperature of POPC with one unsaturated fatty acid is much lower compared to the fully saturated phospholipid DMPC. Phase transition temperatures of the phospholipids used are listed in table 2.1. 1,2-dihexanoyl-*sn*-glycero-3-phosphocholine (DHPC) forms micelles, not bilayers in dilute aqueous solutions, and therefore does not exhibit a clear phase transition temperature. For DMPE-DTPA expected values are given.

Table 2.1: Phospholipids used: Abbreviation, nomenclature according to IU-PAC, phase transition temperature T_m and chemical structure (sources: http://www.avantilipids.com; T_m taken from Walde and Ichikawa (2001)).

Abbreviation	IUPAC Nomenclature	T_m
POPC	1-palmitoyl-2-oleoyl-*sn*-glycero-3-phosphocholine	-2.5 $\pm$ 2.4 °C

| DMPC | 1,2-dimyristoyl-*sn*-glycero-3-phosphocholine | 23.6 $\pm$ 1.5 °C |

| SOPC | 1-stearoyl-2-oleoyl-*sn*-glycero-3-phosphocholine | 6.9 $\pm$ 2.9 °C |

| DHPC | 1,2-dihexanoyl-*sn*-glycero-3-phosphocholine | |

| DMPE-DTPA | 1,2-dimyristoyl-*sn*-glycero-3-phospho-ethanolamine-diethylene-triamine-pentaacetate | 25 °C |

2.2 Self-assembly Structures of Phospholipids: Micelles, Vesicles and Bicelles

Due to their amphiphilic character, the phospholipids arrange spontaneously into minimum energy assemblies. In an aqueous environment, phospholipids tend to form self-assembly structures where the fatty acid chains are shielded from water by the polar head groups. Depending on the specific properties of the phospolipids, they form a variety of structures. Some of these structures, which are relevant to this work, are shown in Fig. 2.3.
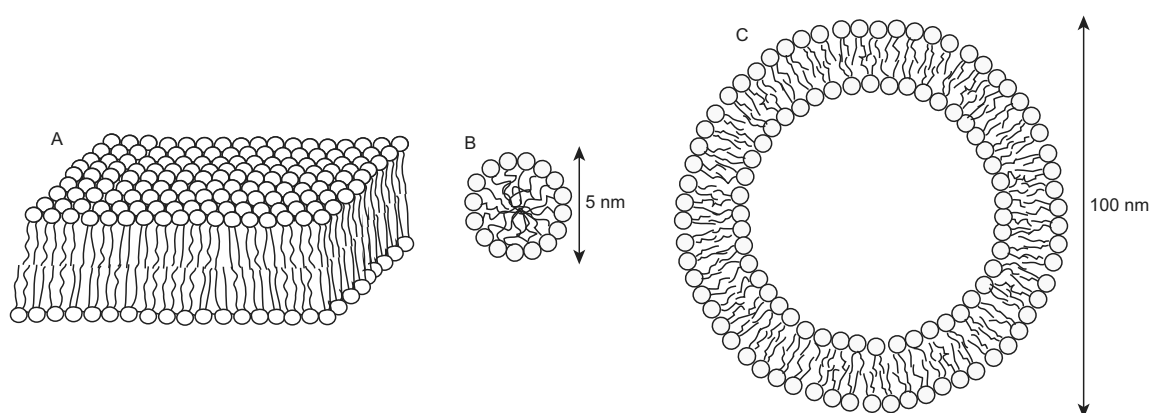
Figure 2.3: Typical self-assembly structures of amphiphilic lipids: bilayer sheet (A), micelle (B), and bilayer vesicle (C).

Which aggregate is formed depends on the chemical structure and geometry of the phospholipid units: wedge-shaped lipids tend to build curved surfaces found e.g. in micelles, whereas more cylindrical units prefer to build planar bilayers. Self-closed bilayers form vesicles in aqueous solutions. Depending on the method of preparation, lipid vesicles can be multi-, oligo- or unilamellar (Walde and Ichikawa, 2001). The type of structure furthermore depends on the temperature, the concentration of lipids and the solvent.

For lipid mixtures the type of structure formed is highly dependent on the miscibility of the two lipids. Lateral segregation in vesicles above a certain miscibility temperature can lead to domain formation. Veatch and Keller (2002) showed for giant unilamellar vesicles consisting of a ternary mixture of saturated, unsaturated phospholipids and cholesterol three distinct phase morphologies, detected by fluorescence microscopy. At low cholesterol composition and low temperature a solid-liquid coexistence occurs where the solid domains show a behavior of rigid bodies. When

the cholesterol content is increased, the domains become liquid as well. The domains fuse and form a small number of large domains. If the cholesterol content is further increased (to $50 - 55$ mol%) or the temperature is increased, the third phase occurs, which is a uniform liquid where domains are no longer observed. Pencer *et al.* (2005a) and Masui *et al.* (2006) found such lipid domains also for small unilamellar vesicles by small-angle neutron scattering (SANS) using contrast matching technique with chaindeuterated phospholipids.

If mixtures of short-chain (DHPC) and long-chain (DMPC) Phospholipids are used, different self-assembly structures are found (Triba *et al.*, 2005). DHPC tends to be in regions with a high curvature whereas DMPC prefers to be in planar areas. The resulting structure has been described as a bicelle (Sanders and Prosser, 1998): a disc shaped bilayer of DMPC with the edges covered by DHPC (Fig. 2.4 left). Recently different authors (Katsaras *et al.*, 2005; Nieh *et al.*, 2002; Triba *et al.*, 2005, 2006; van Dam *et al.*, 2004, 2006) have shown that the phase diagram of a DMPC/DHPC mixture is much more complex and highly depends on the molar ratio, the concentration and the temperature (Fig. 2.4 right).
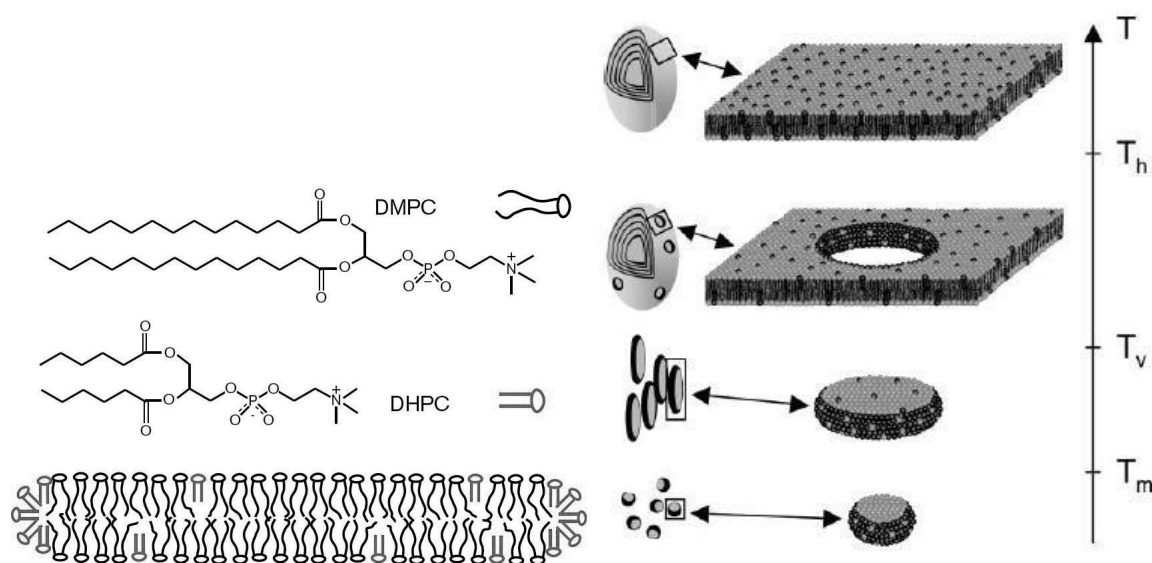
Figure 2.4: Self-assembly structures of a DMPC/DHPC lipid mixture. Bicelle according to Sanders and Prosser (1998) (left). Temperature dependent structure: small segregated bicelles, larger interacting mixed bicelles, large perforated multilamellar vesicles, large mixed multilamellar vesicles according to Triba *et al.* (2005) (right, bottom to top).

2.3 Magnetic Anisotropy and Magnetic Alignment

Phospholipids have a slight diamagnetic anisotropy $\Delta\chi$. According to Eq. 2.1 the diamagnetic anisotropy is the difference between the diamagnetic susceptibility of molecules oriented parallel ($\chi_{\parallel}$) and perpendicular ($\chi_{\perp}$) to the magnetic field (Qiu *et al.*, 1993). In strong magnetic fields, this results in a torque acting on the molecule which is minimal when the molecule is oriented with the long molecular axis perpendicular to the magnetic field for negative $\Delta\chi$, and parallel for positive $\Delta\chi$.

$$\Delta\chi = \chi_{\parallel} - \chi_{\perp} \tag{2.1}$$

Because the diamagnetic anisotropy of phospholipids is slightly negative, they prefer to orient with the long axis (i.e. the fatty acid chain) perpendicular to the magnetic field. However the Brownian motion induced by the randomizing thermal energy kT is much higher than the orienting force and therefore orientation of single molecules is impossible at currently realizable magnetic field strengths.

In self-assembly systems, where molecules are grouped and oriented parallel to each other, the magnetic orientation energy of each molecule is summed up, and macroscopic orientation becomes possible (Eq. 2.2) (Qiu *et al.*, 1993).

$$\frac{E_M}{E_T} = \frac{N \cdot \Delta\chi \cdot H^2}{k \cdot T} \tag{2.2}$$

N is the aggregation number, i.e. the number of molecules with the same orientation, and H is the magnetic field strength.

In this work, paramagnetic lanthanides were added to the phospholipid systems in order to enhance $\Delta\chi$ and therefore the responsiveness to magnetic fields. The lanthanides were anchored to the membrane using DMPE-DTPA, a phospholipid with a chelating agent attached to its headgroup (see Tab. 2.1). As the molecular magnetic anisotropies of DMPC and DMPE-DTPA·Tm have been determined, it is possible to calculate the minimal amount of oriented lipids needed to equalize kT at a given magnetic field strength. $\Delta\chi$ of DMPE-DTPA·Tm is $+90 \times 10^{-8} erg\,cm^{-3}\,G^{-2}$ (Prosser *et al.*, 1998b). $\Delta\chi$ of DMPC is $-0.58 \times 10^{-8} erg\,cm^{-3}\,G^{-2}$ (Scholz *et al.*, 1984). The molecular volume of DMPE-DTPA·Tm is around 1209Å^{-3} (volume of DMPC plus volume of DTPA obtained from D'Arceuil *et al.* (2004)), and around 1101Å^{-3} for DMPC (Nagle and Tristram-Nagle, 2000). According to Eq.2.2 with

$k = 1.3806 \times 10^{-16} \, \text{erg K}^{-1}$, the magnetic field needed to orient a single molecule of DMPE-DTPA·Tm at room temperature would be in the range of 620 Tesla. At 8 T, an aggregate of around 6000 molecules of DMPE-DTPA·Tm would be needed to overcome kT. A flat disk shaped bilayer formed of 6000 DMPE-DTPA·Tm molecules would have a diameter of just under 50 nm, assuming an area per molecule of $0.6 \, \text{nm}^2$. For DMPC, the aggregation number needed to overcome kT would be around 1×10^6, the corresponding disk diameter would be around 600 nm.

Following the same principle, phosphatidylcholine vesicles are slightly deformed from spherical to prolate spheroid or cigar shape in magnetic fields, because in a deformed vesicle more membrane molecules can acquire a perpendicular orientation to the magnetic field (Brumm *et al.*, 1992; Helfrich, 1973; Kiselev *et al.*, 2006, 2008; Reinl *et al.*, 1992). Along with the deformation goes magnetic orientation of the vesicle with the major axis in direction of the magnetic field. Counteracting the deformation is the membrane rigidity, κ. According to Helfrich (1973), the deformation of a vesicle in a magnetic field can be calculated as follows:

$$\frac{\Delta R}{R} = \frac{R^2 d \Delta \chi H^2}{12\kappa} \tag{2.3}$$

The deformation of an idealized magneto-responsive vesicle, assuming a vesicle purely made of DMPE-DTPA·Tm, a large radius R of 100 nm, standard membrane rigidity, and a large magnetic field strength of 14 T was calculated using Eq. 2.3. The parameters converted to the CGS unit system are listed below:

$$\left. \begin{aligned} R &= 1 \times 10^{-5} \, \text{cm} \\ \Delta \chi &= 90 \times 10^{-8} \\ H &= 140\,000 \, \text{Oe} \\ \kappa &= K \cdot d \\ K &= 10^{-6} \, \text{dyne} \end{aligned} \right\} \Rightarrow \Delta R = b - a = -9.8 \, \text{nm} \tag{2.4}$$

Unlike a pure phospholipid vesicle, a vesicle doped with Tm is deformed from a sphere to an oblate and not to a prolate spheroid, because of the positive sign of the magnetic anisotropy conferred by the lanthanide ion (see Chapter 2.4). The half-axis difference of the so formed spheroid, ΔR, is only about 10 nm. Assuming a constant surface area, the actual dimensions of the deformed vesicle can then be calculated.

$$A_{vesicle} = constant = 4\pi R^2 = 125\,664\,\text{nm}^2 \tag{2.5}$$

$$A_{oblate} = 2\pi \left(a^2 + \frac{b^2}{\sin\left(\arccos\left(\frac{b}{a}\right)\right)} \right) \times \ln \left(\frac{\cos\left(\arccos\left(\frac{b}{a}\right)\right)}{1 - \sin\left(\arccos\left(\frac{b}{a}\right)\right)} \right) \tag{2.6}$$

$$\Rightarrow \quad \begin{aligned} a &= 103\,\text{nm} \\ b &= 93\,\text{nm} \end{aligned} \tag{2.7}$$

The volume difference between the sphere and deformed vesicle is then

$$\Delta V = \frac{4}{3}\pi \left(R^3 - a^2 b \right) = 1.38\% \tag{2.8}$$

The commonly used vesicles within this work had $20\,\text{mol}\%$ chelator lipid and a diameter of $100\,\text{nm}$, and were exposed to a magnetic field of about $6\,\text{T}$. The magnetic deformation for these vesicles would roughly be 160 times smaller than in the calculation above. For these relatively small unilamellar vesicles it therefore does not appear promising to expect a large deformation in a magnetic field.

2.4 Lanthanides

Lanthanides are the chemical elements with the atomic numbers of 57 to 71. Lanthanides are chemically similar to each other and most of them occur as trivalent cations. Most have a very large magnetic anisotropy $\Delta\chi$ (Binnemans and Gorller-Walrand, 2002). Ce^{3+}, Pr^{3+}, Nd^{3+}, Sm^{3+}, Tb^{3+}, Dy^{3+} and Ho^{3+} confer a large negative magnetic anisotropy to the phospholipid membrane, whereas the second group (Eu^{3+}, Er^{3+}, Tm^{3+}, Yb^{3+}) confer a large positive magnetic anisotropy, leading to a preferred orientation with the long molecular axis perpendicular to the magnetic field. Thulium (Tm^{3+}) has the largest positive $\Delta\chi$ among the lanthanides, dysprosium (Dy^{3+}) the largest negative $\Delta\chi$. Lanthanum (La^{3+}) is diamagnetic (Binnemans and Gorller-Walrand, 2002). Lanthanides are anchored into the phospholipid bilayer by a chelator (Diethylenetriaminepentaacetate, DTPA) covalently bound to a phospholipid head group (Prosser *et al.*, 1998b). Lanthanum anchored by DMPE-DTPA to phospholipid membranes does not influence their magnetic orientation but can be used for NMR-spectroscopy without restriction, in contrast to paramagnetic lanthanides, which cause line shift and broadening of the NMR-spectra.

2.5 Cocoa Butter

Cocoa butter, like most edible oils and fats, mainly consists of a mixture of triacylglycerols (TAGs). Like phosphatidylcholine, TAGs belong to the group of glycerol based lipids. While phosphatidylcholine consists of a glycerol molecule which is esterified with two fatty acids and linked to a phosphocholine, a TAG is a triester of glycerol with three fatty acid molecules. Fig. 2.5 shows the general chemical structure of a triacylglycerol (comp. Tab. 2.1 for the chemical structure of phosphatidylcholines). R1, R2 and R3 stand for the three acyl chains. Fatty acids consist of a hydrocarbon chain terminated by a carboxylic acid group. TAGs are commonly denoted by a three letter code, each letter representing one of the fatty acids. The main fraction of cocoa butter consists of POS, SOS and POP, all with two saturated acyl chains in the outer positions, and one unsaturated acyl chain in the middle (Foubert *et al.*, 2004). P stands for the saturated palmitic acid, O for the monounsaturated oleic acid, and S for the saturated stearic acid. In Tab. 2.1, these fatty acids are depicted esterified to the glycerol backbone of a phosphocholine.
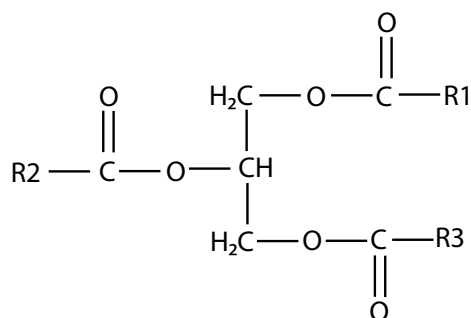
Figure 2.5: Structure of a triacylglyceride

.

When molten cocoa butter is cooled down, the fatty acids of the TAGs adopt an all trans configuration and form a crystalline structure, which is in principle comparable to the phase transition of phospholipid membranes as described in chapter 2.1. For TAG systems as well as for phospholipid membranes, the fatty acid composition strongly influences the crystallization behavior. Because of the mixed TAG composition of cocoa butter, cocoa butter can form up to six different crystal modifications, which differ in melting range and chain packing. See a review of Himawan *et al.* (2006) for the possible chain packing models of the different crystal forms. In Tab. 2.2 the nomenclature used in this work for the six crystal modifications is listed along with the corresponding melting ranges (Zeng, 2000).

Table 2.2: Cocoa butter crystal modifications, melting range, and crystal packing information (Himawan *et al.*, 2006)

Polymorph type	Melting range [℃]	Crystal packing
γ	13.0-18.0	mixed
α	18.0-22.5	hexagonal
III	22.5-27.0	mixed
βIV	27.0-29.0	orthorhombic
βV	29.0-33.5	tricline
βVI	33.5-37.5	tricline

Besides the heterogeneous TAG composition, the main reason for the complex crystal phase behavior of cocoa butter is the presence of the oleic acid in the middle position of the most prominent TAGs. The double bond of the unsaturated olein represents an inflexible kink in the acyl chain which gives steric hindrance to the crystal packing (Himawan *et al.*, 2006). Cocoa butter tends to crystallize in the lower melting and unstable forms γ, α, III and βIV, and then recrystallize to the higher melting and more stable forms βV and finally βVI. For edible products such as chocolate, the type of crystal form present in the finished product greatly affects its physico-chemical properties (Bolliger *et al.*, 1999; Windhab, 1999).

3 Set Up of a Magnet Rheometer Laboratory

3.1 Introduction

The aim of the magnet rheometer set up is to combine the influences of a strong magnetic field with a structuring or destabilizing flow field, and to allow on line gathering of information on the sample properties. For this a set up was constructed which comprises a superconducting magnet with a controlled stress rheometer situated above the magnet bore, driving a temperature controlled concentric cylinder shear cell inside the bore. Additionally, an optical measurement system with a laser beam passing through the couette gap was installed. Information on the material properties can be gathered over the rheological data obtained from the rheometer, as well as the scattering pattern and the intensity of a laser beam passing through the shear gap.

3.2 Description of the Magnet Rheometer Laboratory Components

3.2.1 Magnet and Rheometer

The base of the set up is formed by a cryogen free super conductive magnet (Cryogenic, London, UK). "Cryogen free" is an industrial term used to denote a magnet which is not cooled by liquid helium, but by a gas state helium refrigeration cycle. Compressed helium is expanded in two stages in a cold head unit, which is situated close to the magnet coil. The cold head cools down the magnet coil to a temperature of $6.5\,\mathrm{K}$, at which the Nb_3Sn coil is super conductive. A current of up to $100\,\mathrm{A}$ is passed through the coil, giving a maximal field strength of $5.66\,\mathrm{T}$. The heated helium

is compressed in a cryocompressor and the heat passed on to a coolant water cycle. Cold compressed helium gas is returned to the cold head via flex lines. The magnet has a vertical room temperature bore with a diameter of 78 mm and generates a vertical, adjustable, rampable field. The magnet is mounted onto four aluminum pillars, keeping it away from the ground and allowing access to the bore from the bottom.

The magnet slightly vibrates because of the cold head movement. The rest of the set up is therefore mounted without direct contact to the magnet. Fig. 3.1 shows the principle of the set up. A separate instrument stand was constructed which allowed components to be mounted on top and below the magnet bore on two arms (see Fig. 3.2). The arms can be positioned vertically with the help of pneumatic levers, allowing precise and adjustable positioning of the shear cell and other sample holders in the magnet bore, as well as easy sample removal. Mounted to the top arm are the rheometer and the laser detector. The bottom arm holds the laser and the shear cell over a vertical shaft reaching into the magnet bore from the bottom.
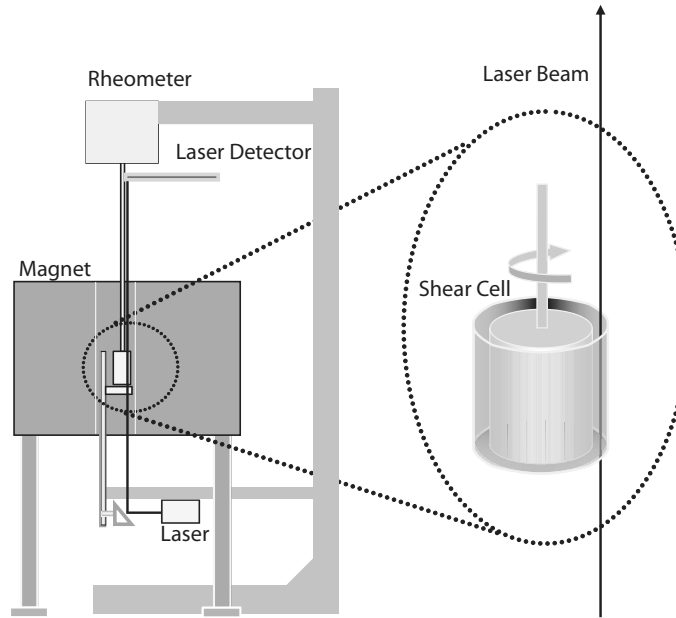
Figure 3.1: Sketch of the magnet rheometer set up (left), and a close up of the principle of the shear cell (right). The shear cell, rheometer and laser installation are mounted to a separate stand without touching the magnet.
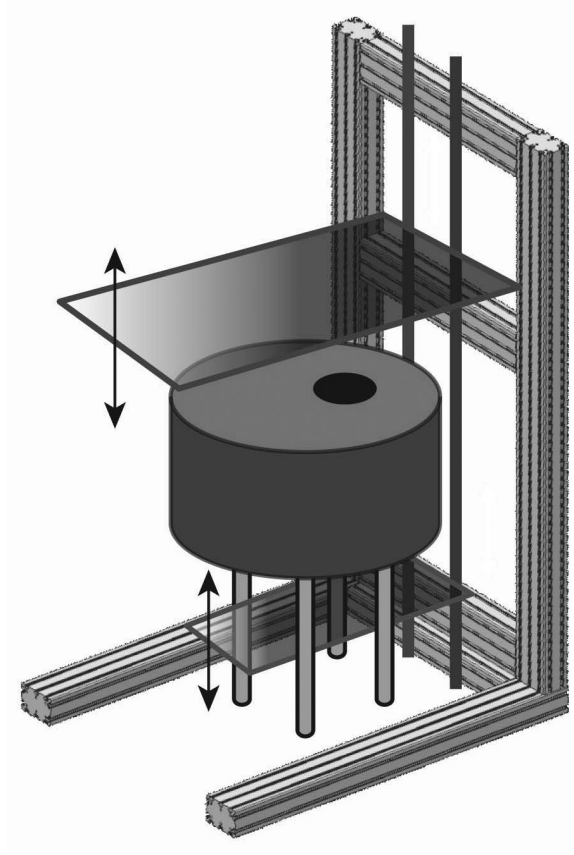
Figure 3.2: Principle of the separate stand of the magnet rheometer set up. The rheometer, laser installation and shear cell are mounted on two arms which are vertically adjustable (arrows) without touching the magnet.

A controlled stress rheometer (Bohlin CS 50, Malvern Instruments, Worcestershire, UK) was installed, allowing for measurements in a torque range of $1\,\mu$Nm to $50\,$mNm. The base of the rheometer was sawed off, and the rheometer head was mounted to the upper arm of the rheometer stand. In order to keep its drag cup motor away from high magnetic field strengths, it is connected to the shear cell by a prolonged $25\,$cm aluminum shaft. Great care in production and handling of the rheometer shaft was taken to avoid wobbling due to concentricity deviations. Fig. 3.3 shows two pictures of the magnet rheometer, one with the shear cell outside the magnet bore (left picture) and one with the shear cell inside the bore (right picture).

Figure 3.3: Pictures of the magnet rheometer set up, showing the rheometer, the super conductive magnet, the rheometer stand, as well as the shear cell. Left: Shear cell outside the magnet bore. Right: Shear cell lowered into the magnet bore

3.2.2 Shear Cell

Fig. 3.4 shows a picture of the shear cell (left), and a corresponding cut off figure (right), with arrows indicating the different components. The shear cell consists of a double walled outer cylinder (arrow a) and a rotating inner cylinder (arrow b), here called rheometer bob. The shear cell is temperature controlled over a water bath, the water flowing inside of the double walled outer cylinder. The outer cylinder is mounted to the bottom arm of the instrument stand. The inner cylinder is connected to the rheometer by the rheometer shaft. The sample is sheared in the gap between the outer and the inner cylinder. Two optical glass inserts in the outer cylinder assure that the laser beam passes the sample without being deviated on an uneven surface (arrows c). An acrylic glass insert isolates the top of the sample from exposure to room temperature (arrow e). A temperature sensor is inserted through this insert and penetrates the top 3 mm of the shear gap (arrow d). Fig. 3.5 shows a technical drawing with the lengths indicated in mm (left), and a close up of the central part of the shear cell (right), where arrows show in more detail the optical glass inserts with passing laser beam (a), the level to which the sample is filled into the shear cell (b), and the temperature sensor (c).
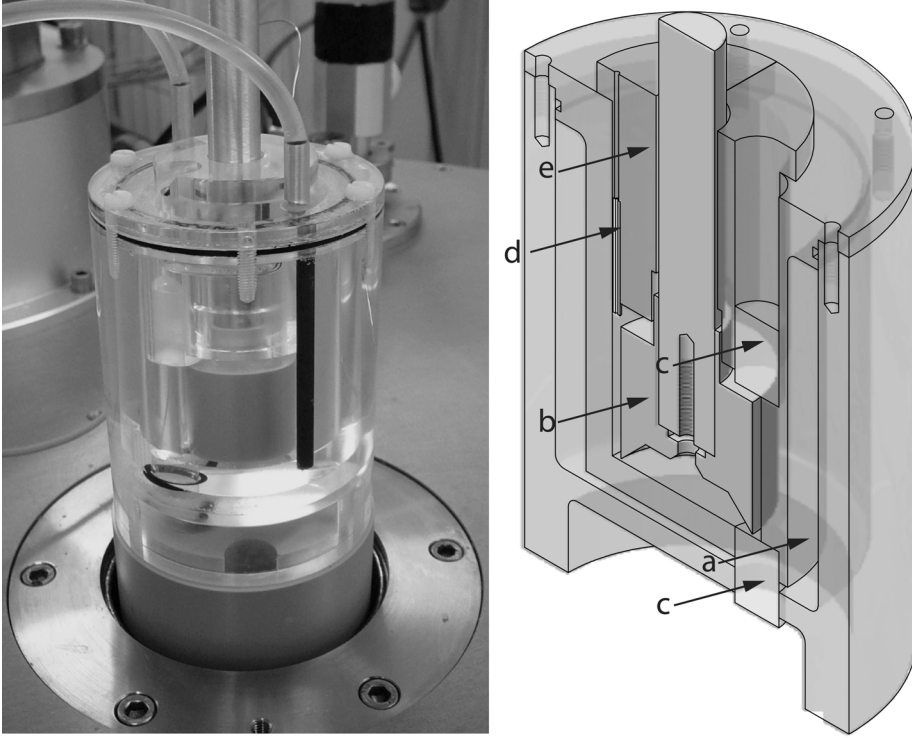
Figure 3.4: A picture of the shear cell (left), and a cut off drawing (right). Arrows show the double walled outer cylinder (a), the inner cylinder (rheometer bob) (b), the optical glass inserts for the laser beam (c), the sleeve for the 0.5 mm thick temperature sensor (d), and the acrylic glass cover (e).

The inner cylinder has a height of 26 mm and a diameter of 30 mm. The shear gap between outer and inner cylinder is 2 mm. The gap from the bottom of the bob to the bottom of the shear cell is 0.5 mm. The rheometer bob is screwed to the rheometer shaft from the bottom. As can be seen in Fig. 3.4 (right), the bottom of the rheometer bob is not flat, but has a conical cut out. When the bob is lowered into the sample, an air pocket is trapped under the bob, thus minimizing the shear force on the sample on the bottom of the shear cell. The top of the bob has a collar enclosing the rheometer shaft, shielding the sample from contact with the aluminum rheometer shaft, which has a high thermal conductivity. The rheometer bob is made from polyetheretherketone (PEEK). PEEK is a chemically inert and mechanically stable thermoplastic with a low heat transfer coefficient (about 0.25 W/mK). The outer cylinder consists of acrylic glass. All the materials used inside the bore are non magnetic and non conductive, in order to minimize eddy currents. The only exceptions for stability reasons are the two aluminum tubes connecting the outer cylinder to the water cycle, and the rheometer shaft.
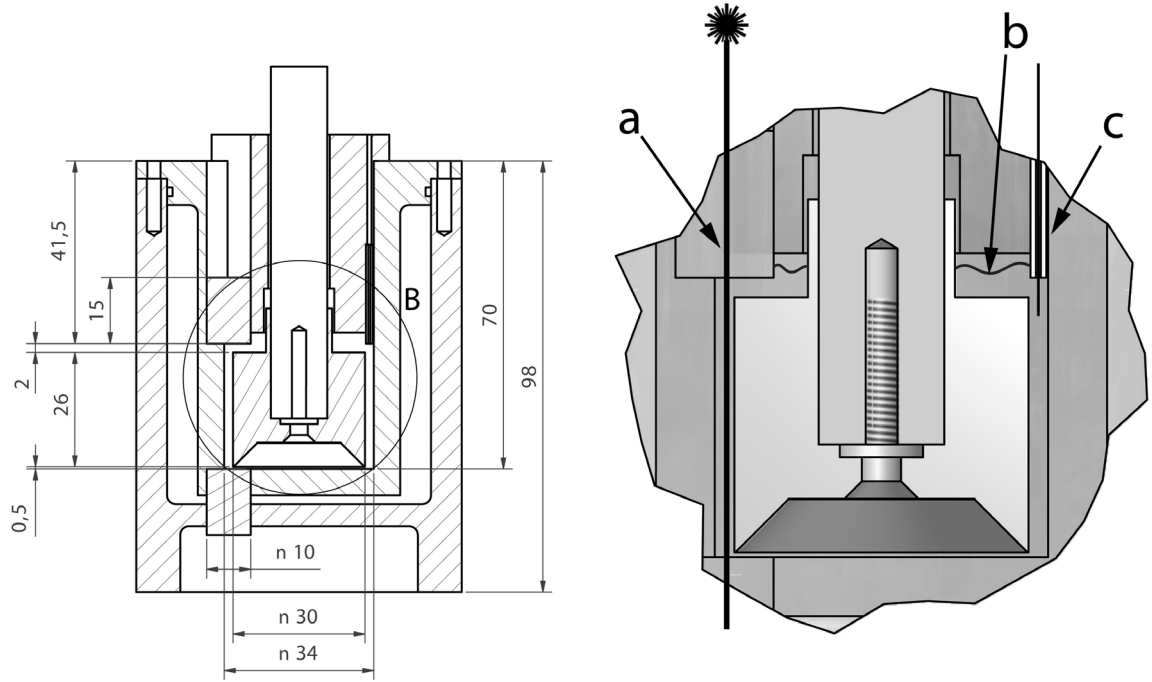
Figure 3.5: A technical drawing of the shear cell with lengths indicated in mm (left) and a close up of the central part of the shear cell (right). Arrows show the optical glass inserts with passing laser beam (a), the level to which the sample is filled into the shear cell (b), and the temperature sensor (c).

Fig. 3.6 show the position of the shear cell when it is lowered into the magnet bore in relation to the magnet coils. The magnetic field in the bore of the magnet was simulated with Maxwell SV (Ansoft LLC, USA), a finite element analysis software for electromagnetic problems. For the simulation a magnet coil of 12197 whorls with a height of 100 mm and a diameter of 85 mm was used, with a current of 100 A flowing through it. In Fig. 3.6, the magnetic flux density is plotted over a silhouette of the shear cell. According to the simulation, the sample in the shear cell is situated within a magnetic field ranging from 5.6 T to 5.4 T. The field homogeneity in the bore was also measured using a hall probe at a magnetic field strength of 3 T. It was not possible to measure the field homogeneity as precisely as the simulation predicted, but the measurements also indicated a high magnetic field homogeneity in the sample area.

A series of shear experiments was made to test the magnet rheometer set up. It was investigated, whether the new shear cell with the prolonged rheometer shaft still gave accurate rheological data, and whether the magnetic field had a negative influence on the rheometer. Sunflower oil was sheared under three different shear stresses at room temperature. At each shear stress, four measurements were made: without
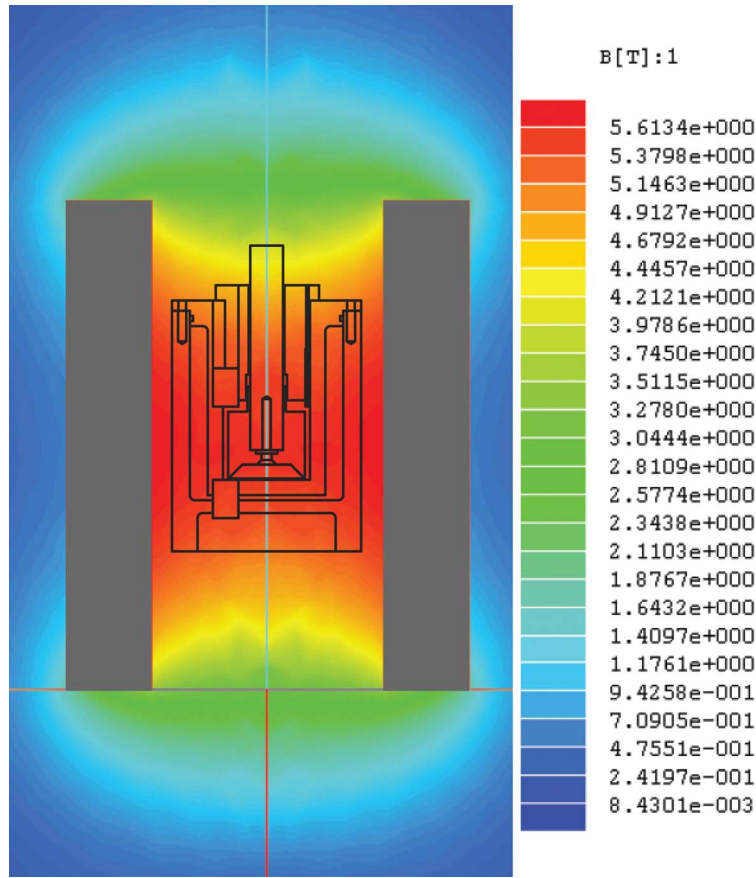
Figure 3.6: A simulation of the magnetic field in the magnet bore at a current of 100 A. A silhouette of the shear cell is shown in the correct size in relation to the magnet coil. The sample area is in a region of 95% homogeneity.

magnetic field, at $4\,\mathrm{T}$, at $4.5\,\mathrm{T}$, and at $5.6\,\mathrm{T}$. Sunflower oil is a Newtonian fluid, therefore the same viscosity should be obtained at all shear rates. Tab. 3.1 shows that the measured viscosity stayed constant, independent of the shear rate or the magnetic field strength, thus proving that the magnetic field does not influence the rheometer at these conditions. The geometrical parameters of the shear cell were then entered into the rheometer software. The software was calibrated to the new shear cell geometry with standard viscosity silicon oils, in order to obtain correct viscosity values.

Table 3.1: Shear tests with sunflower oil at RT in the magnet rheometer at different magnetic field strengths. The magnetic field did not influence the measured viscosity.

	0 T	4 T	4.5 T	5.66 T
Shear stress [Pa]	Viscosity [Pa s 10^{-2}]			
2.13	5.81	5.82	5.82	5.83
3.16	5.82	5.83	5.83	5.84
4.19	5.82	5.85	5.85	5.85

3.2.3 Laser optics

Fig. 3.1 shows the laser position and the path of the laser beam through the sample to the detector. All the components used for the laser set up were obtained from Newport (Irvine CA, USA). For the set up a diode laser with an adjustable optical output power of maximal 25 mW was used. The laser has a wavelength of 632 nm (red), and emits a circular beam of 1 mm diameter. Fig. 3.7 shows the bottom arm of the rheometer stand with the laser set up. The laser (arrow a) is mounted horizontally to the bottom arm with an aluminum bracket, which figures as a heat sink (arrow b). The laser is redirected into the magnet bore by a mirror (arrow c) mounted to an optical positioner (arrow d). It then passes the optical rod shaped glass inserts through the sample (Fig. 3.5 (right)), and hits the 100 mm² silicon chip of the intensity detector (arrow a in Fig. 3.8). The detector of the laser beam is mounted to the rheometer head on top of the magnet. The detector is secured to an X-Y-table for fine positioning (arrow b in Fig. 3.8). The measured voltage is converted into a digital signal and logged with Lab View software.
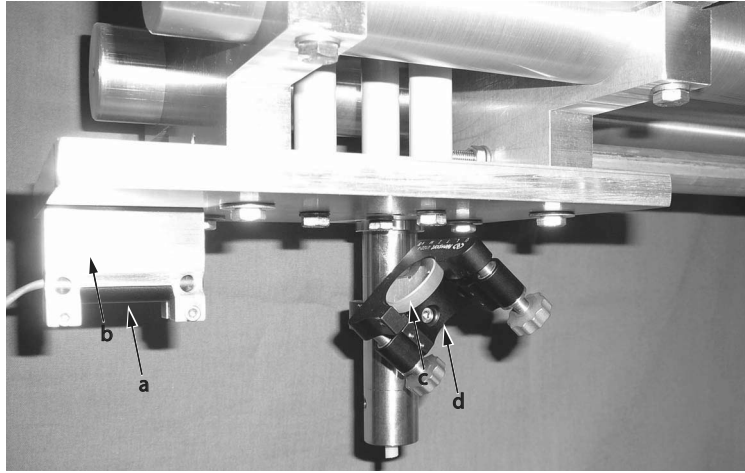
Figure 3.7: Installation of the diode laser (arrow a), the aluminum heat sink (b), the mirror redirecting the laser beam into the magnet bore (c), and the fine positioning mirror holder (c).
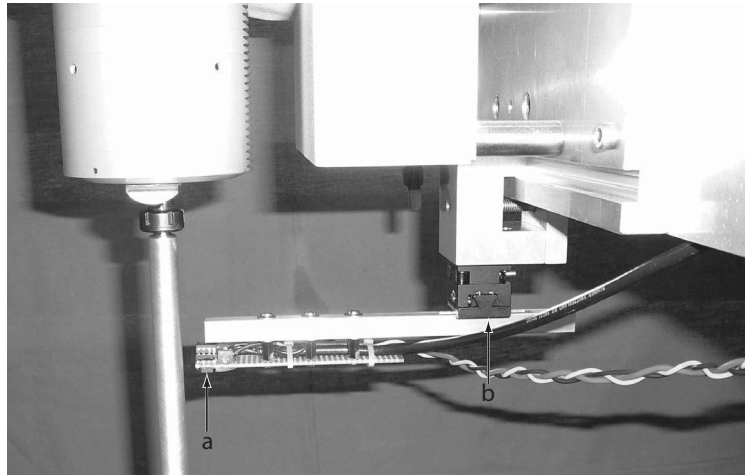
Figure 3.8: Installation of the laser detector. After passing the shear cell the laser hits the $100\,\text{mm}^2$ silicon chip (arrow a). The laser detector is mounted to the rheometer with an XY-table for fine positioning (arrow b).

3.2.4 Peripheral Instruments

The magnet rheometer set up as described above is encircled by a variety of peripheral components. Fig. 3.9 shows a picture of the whole magnet rheometer laboratory. The components are labeled in Fig. 3.10, which shows a schematic overview.
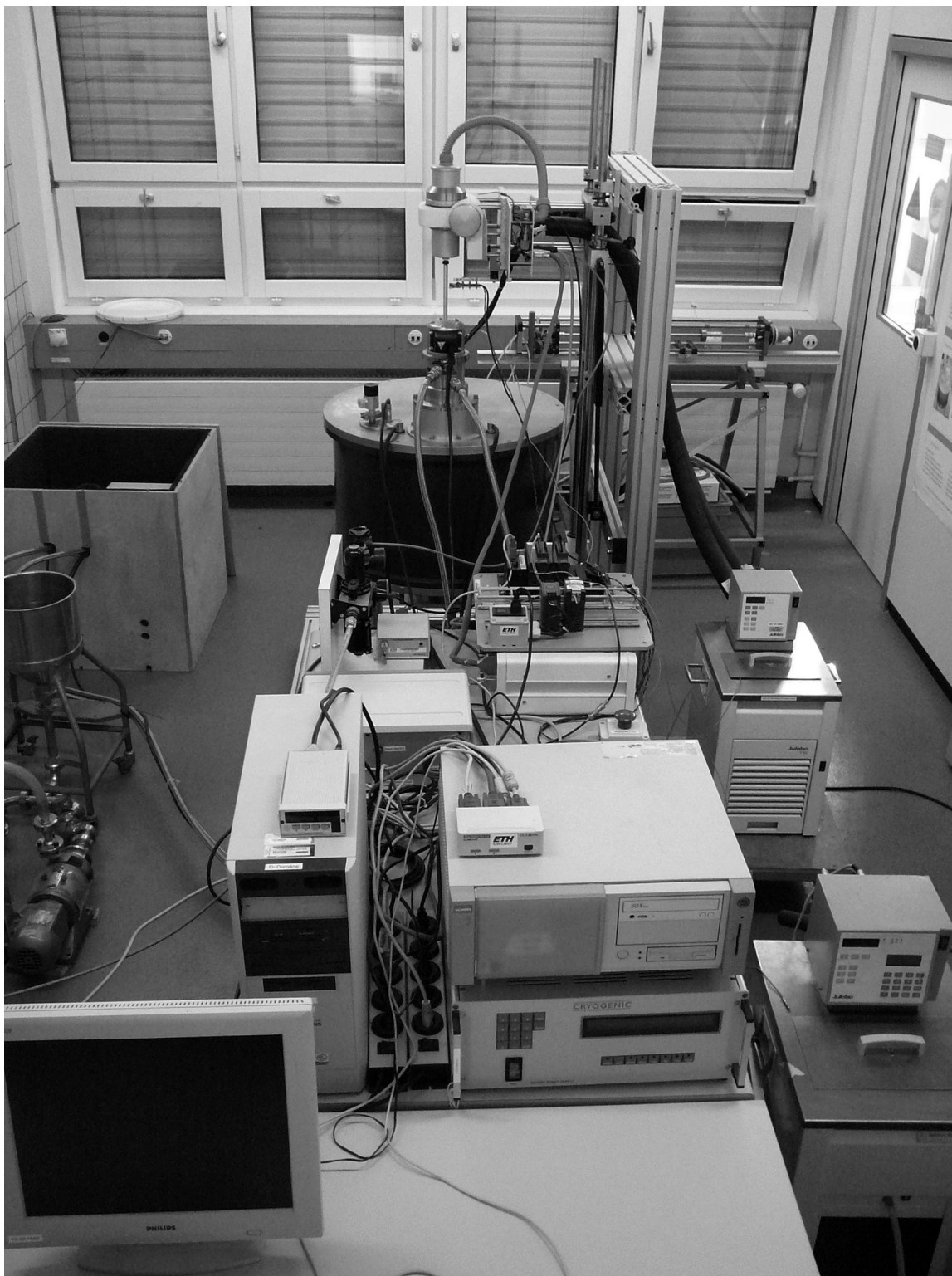
Figure 3.9: Picture of the magnet rheometer laboratory. See Fig. 3.10 for a labelled schematic overview.
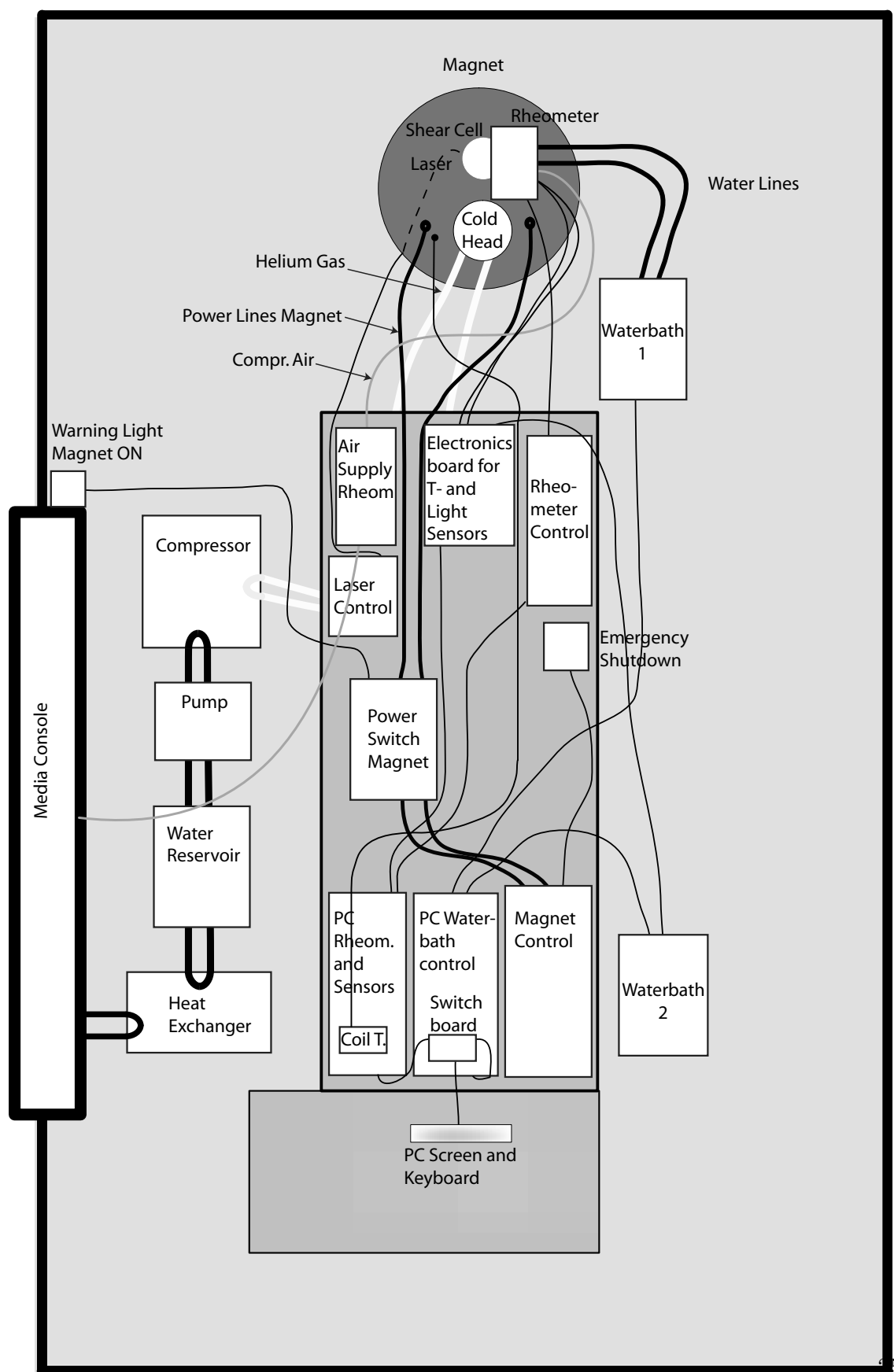
Figure 3.10: A schematic overview of the magnet rheometer laboratory.

In this chapter the peripheral components of the magnet rheometer laboratory are briefly described:

Pump, water reservoir, heat exchanger: As described in chapter 3.2.1, the heat removed from the magnet is given of to a coolant water cycle by the cryocompressor. Because the water running through the cryocompressor has to be free of impurities, a closed coolant water loop was installed. To minimize calcification, a 1:1 mixture of tab and deionized water is used, to which an anti fungal and antimicrobial component was added. The loop consists of a centrifugal pump, a water reservoir where air can escape from the loop, and a plate heat exchanger, where heat is transported to the in house cooling water cycle. As shown in Fig. 3.9, the cryocompressor is positioned inside a wooden box lined with sound dampening foam to reduce noise.

Air supply rheometer: Supplies the rheometer head with compressed air for the air bearing of the drag cup motor and its cooling. The air supply reduces the pressure of the compressed air, passes it through an oil and particle filter, and distributes it to the air bearing and the coolant inlet.

Laser control: Turns the laser on and off.

Magnet control: Sets the magnetic field strength and the ramping speed by controlling the current to the magnet coils.

Emergency shutdown: An interrupt switch which prompts the magnet control to ramp down the magnetic field at the maximal permissive speed without danger of quenching.

Power switch magnet and magnet warning light: One of the two magnet power lines runs through an induction ring in the power switch magnet. If current is detected in the power line, the magnet warning light shines red, indicating the presence of a magnetic field. If the magnet is turned on but no current flows to the coil it shines orange. If the magnet is turned off it shines green.

Water bath 1 and Water bath 2: Water bath 1 is connected to the shear cell over insulated water hoses. Water bath 2 is located away from the magnet and is used to temper samples without magnetic field. Water bath 2 is used when experiments with and without magnetic field are performed simultaneously. Both water baths are from Julabo (JULABO Labortechnik, Seelbach, Germany), and are controlled over the RS232 interface by the *PC waterbath*. The temperature stability is at least $\pm 0.03\,°C$ for both water baths.

Rheometer control: An advantage of the rheometer used in this set up is that the

control is not integrated into the rheometer head, where it could be influenced by the axial stray field of the magnet, but in a separate control box. The rheometer control box communicates with the rheometer software on the PC and controls the rheometer head.

Electronics box for temperature and light sensors: The voltages received from the temperature sensors and the laser intensity detector are converted to digital signals and sent to the *PC rheometer and sensors*, where they are logged with LabView software.

3.3 Conclusion

The set up as described above is the product of a number of optimizing constructive iterations. For example, the shear cell had to be redesigned, because earlier shear cell designs did not give a homogeneous temperature over the whole sample volume, were too slow to adapt to the set point temperature, and deviated the laser beam away from the detector when the temperature was lowered. However, the final configuration of the magnet rheometer as described above fulfills the requirements of an experimental set up, where flow- and magnetic fields can act individually or simultaneously on a sample, and information on the sample properties are obtained during the experiment. The rheometer sets the shear rate in the shear gap, and at the same time gathers accurate rheological data on the sample, with or without magnetic field. While linear rheology can be performed in high magnetic fields of up to 5.66 T, it is not possible to perform oscillatory rheology with the magnetic field turned on, most likely due to eddy currents induced by the change of rotational speed of the rheometer shaft. With the optical set up the laser intensity passing through the shear gap is measured, giving information about the turbidity of the sample. This set up may be upgraded to a more complex measurement set up in the future, where the detector is replaced by a CCD camera to gather orientational information of the sample over the scattering pattern of the laser beam, or to a measurement set up for birefringence and dichroism, which would require positioning of optical components such as polarizers, lenses, and a photoelastic modulator in the magnet bore.

In this work, the set up was used for shear crystallization of cocoa butter under magnetic field (see chapter 4) and permeability measurements of phospholipid vesicles (see chapter 5.2.8).

4 Cocoa Butter

4.1 Introduction

Cocoa butter is a main component of many ointments, toiletries, pharmaceuticals and food, chocolate in particular. Cocoa butter is polymorphic, which denotes the property of a substance to form different crystal modifications with different molecular packing configurations. Crystallization behavior of cocoa butter is complex, because it occurs from a melt of a mixture of triglycerides, and not from a pure solution (Himawan *et al.*, 2006). It is critical for cocoa butter containing products to obtain the right crystal composition, as the crystal type influences many physico-chemical properties such as melting temperature, contraction behavior, surface smoothness, and the tendency for crystal transformation and fat migration (Peschar *et al.*, 2004). Crystal transformation of cocoa butter occurs in general spontaneously from lower melting to higher melting and more compact crystal morphologies, thus influencing the shelf life of the products. Which polymorph form is obtained depends on the processing conditions used (Windhab, 1999).

For cocoa butter six different polymorph forms have been identified and widely accepted, whereas the nomenclature of these six forms is diverse (Dimick and Manning, 1987). The terms used in this work will be referring to the ones used by Beckett (1994) and Windhab (1999). The desired crystal type for chocolate is βV. To obtain the desired form V directly, chocolate is usually melted completely first, then cooled down below the crystallization temperature of the lower melting crystal types, and then tempered, which consists of melting out the undesired low melting crystal forms by reheating just below the melting temperature of βV (Beckett, 1994).

Other possibilities to influence the crystal morphology are cyclothermic tempering with various heating and cooling stages (Kleinert, 1970), seed-crystallization with βVI crystals (Windhab, 1999), shear crystallization (Bolliger *et al.*, 1998, 1999; Mazzanti *et al.*, 2003, 2005; Stapley *et al.*, 1999), and combinations thereof (Windhab, 1999). Industrial tempering of cocoa butter is a delicate, energy intensive and time consuming process. It would therefore be of interest to find additional possibilities

to influence the crystal morphology. In this work, it was investigated whether it is possible to influence the crystallization dynamics or the crystal type formed by applying a strong static magnetic field to the cocoa butter melt during crystallization. There are a few indications in the literature vaguely suggesting a possible magnetic field effect. Miura *et al.* (2004) showed an effect of a 5 T static magnetic field on the lowest melting polymorph of some pure triglyceride systems, and Beckett (PCT/EP1999/009567, 2002) submitted a patent application for magnetic field controlled cocoa butter crystallization. The available information is not conclusive, and no satisfying mechanism for the magnetic interaction has been proposed. The aim of the here proposed investigation was to gather fundamental results on the subject.

In this work, great care was taken to ensure close temperature control and sample conditions in order to exclude temperature effects. The set up described in chapter 3 was used, consisting of a superconductive magnet with a shear cell in the bore. A rheometer was positioned above the magnet with a prolonged shaft connecting to a shear cell in the magnet bore. A laser beam was passed through the shear gap and the intensity was logged. Crystallization dynamics under shear were investigated by monitoring the laser intensity as well as the viscosity. Additionally, crystal transformation of unsheared samples with and without magnetic field was investigated with differential scanning calorimetry (DSC).

4.2 Material and Methods

4.2.1 Cocoa Butter

Pure refined cocoa butter, obtained from ADM Cocoa B.V. (The Netherlands) was used for the experiments. Samples from the same production batch were used for all experiments to avoid any influence of the triglyceride composition. For the characterization of the cocoa butter a viscosity vs. temperature diagram was recorded with a rheometer with couette geometry (Paar-Physica, Stuttgart, Germany) at a shear rate of $100 \, s^{-1}$ (Fig. 4.1). The cocoa butter exhibits Newtonian flow properties, i.e. the viscosity is independent of the shear rate.
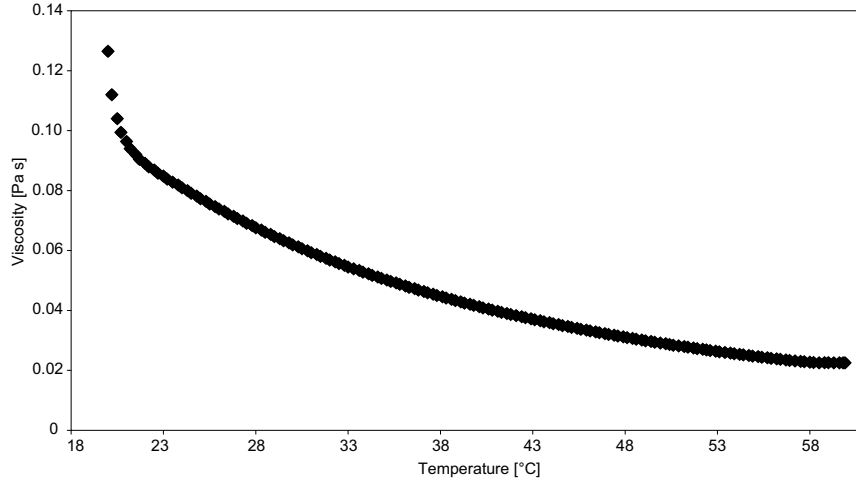
Figure 4.1: Temperature dependence of the viscosity of liquid cocoa butter at a shear rate of $100\,\mathrm{s}^{-1}$

Additionally, the main triacylglycerol composition of the cocoa butter was analyzed with gas chromatography by Mehrle (2007). The composition is shown in Tab. 4.1. The three letters stand for the fatty acids esterified to the glycerol backbone of the triglyceride. P stands for the saturated palmitic acid, $(CH_3(CH_2)_{14}COOH)$; O for the monounsaturated oleic acid $(CH_3(CH_2)_7CH=CH(CH_2)_7COOH)$; and S for the saturated stearic acid $(CH_3(CH_2)_{16}COOH)$. The main fraction of cocoa butter consists of POS, SOS and POP, all with two saturated acyl chains in the outer positions, and one unsaturated acyl chain in the middle. Although not measured here, cocoa butter also contains a variety of other triglycerides in small amounts.

Table 4.1: Triglyceride composition of the cocoa butter used for this work, as determined by gas chromatography (Mehrle, 2007).

Triglyceride	mol%
POS	44.3
SOS	32.8
POP	17.7
SOO	3.2
POO	2.0

4.2.2 Shear Crystallization

All experiments were made with the magnet-rheometer set up described in chapter 3. For each experiment, 100 ml of cocoa butter were heated to 55 °C in a heating cabinet and kept at this temperature until the experiment (for at least 1 h) to prevent any memory effects. The shear cell was brought to the desired temperature (26 °C or 21 °C) before the experiment was started by pumping water from a water bath through the double wall of the shear cell. The water was kept running and the temperature was kept constant during the whole experiment. 7.5 ml of cocoa butter were filled into the shear cell with a pre-heated syringe. The rheometer bob, the optical glass inserts, the temperature sensor and the acrylic glass cover were installed. The shear cell was then lowered into the magnet bore. The laser beam was switched on, and logging of the temperature, viscosity and laser intensity was started. The rheometer was set to the desired shear rate and the magnetic field was set to 5.66 T for experiments with magnetic field. The cocoa butter quickly cooled down to the temperature of the shear cell. The experiments were stopped when the viscosity of the cocoa butter had reached around 5 Pa s.

Shear crystallization tests were made at two conditions: At a shear rate of $89.4\,s^{-1}$ and a temperature of 26 °C, and at a shear rate of $150\,s^{-1}$ and temperature of 21 °C. For both conditions investigated, three experiments with and three without magnetic field were made. At a shear rate of $89.4\,s^{-1}$ and 26 °C three crystallization experiments were also made in a rheometer with couette set up (Paar Physica, Stuttgart, Germany) without magnetic field.

4.2.3 Static Crystallization

For static crystallization experiments, i.e. crystallization of unsheared cocoa butter, the cocoa butter was allowed to crystallize directly in DSC crucibles. Static crystallization experiments were also made with the set up described in chapter 3. Instead of the rheometer bob, an aluminum sample holder containing the DSC crucibles was inserted into the double walled acrylic glass shear cell. The sample holder is shown in Fig. 4.2.

Before the experiments, 100 ml of cocoa butter were melted in a heating cabinet at 55 °C. The DSC crucibles were then filled with 5 µl of liquid cocoa butter using a pipette. Each crucible was weighed to determine the exact sample mass. The crucibles were then sealed with an alloy lid and stacked in the eight equally spaced bores of the sample holder, allowing for a maximum of 80 samples per series of measurement. The

loaded sample holder was transferred back into the heating cabinet and kept for 2 h at 55 °C. The sample holder was then transferred into a water bath for 4 min to ensure a reproducible and rapid cooling to the crystallization temperature. Crystallization experiments were made at 20 °C and 22 °C, and the water bath temperature was set accordingly. The sample holder was then transferred into the shear cell which was pre-tempered to the crystallization temperature with another water bath. A temperature sensor was placed close to the crucibles in one bore, and an insulating soft foam lid was placed on top of the sample holder. The shear cell was then lowered into the magnet bore, and the magnetic field was set to 5.66 T for the experiments with magnetic field.

Figure 4.2: Crucible holder for static crystallization of cocoa butter in magnetic fields. Up to 10 crucibles can be stacked in each bore. For the crystallization at 22 °C both crucible holders were loaded at the same time. One was placed in the magnet bore, the other in a water bath with temperature set to the temperature measured close to the crucibles in the magnet. The crucibles were removed from the bore with a pre cooled contact lens remover and tweezers.
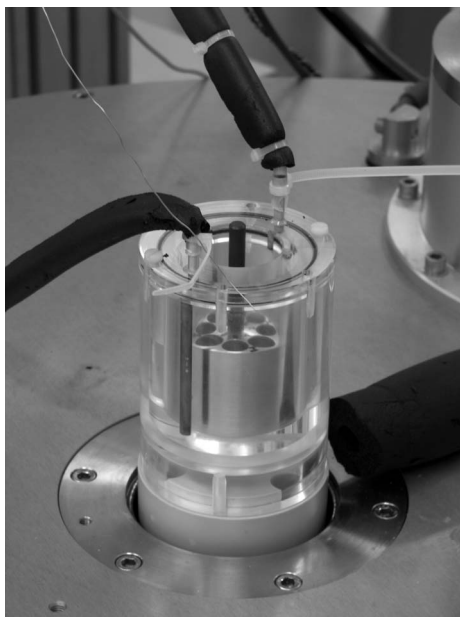
Figure 4.3: Crucible holder inserted into the shear cell. Also shown is the temperature sensor, the isolated leads to the water bath, and on the right side the lid of insulating black foam. For the experiment the lid was put on top of the crucible holder and the shear cell was lowered into the magnet bore.

The zero field measurement at 20 °C was done in the same way as the 5.66 T measurement, but without turning the magnetic field on. The zero field measurement at 22 °C was made at the same time as the 5.66 T measurement, using a second sample holder. The two sample holders were taken out of the heating cabinet at the same time and put into the water bath at 22 °C. While one sample holder was moved into the magnet, the other was kept in the water bath.

DSC crucibles were removed from the sample holder in periodic intervals, in order to follow the crystal development of the cocoa butter. Samples were transferred to the calorimeter in a pre cooled specimen holder. The crystal morphology of the samples was determined by DSC analysis (DSC 822e, Mettler Toledo, Greifensee, Switzerland). DSC curves were recorded from 20 °C to 45 °C with a heating rate of 4 °C per minute under a constant flow of nitrogen. All samples were measured in relation to their mass. For the 20 °C measurements, 6 samples were taken at each measuring time. At 22 °C 4 samples were taken at each measuring time, except at 28.5 h (3 samples) and 47.5 h (2 samples). The DSC curves from each measurement time were averaged to give one curve per measurement time.

4.3 Results and Discussion

4.3.1 Shear Crystallization

Fig. 4.5 shows the different stages of cocoa butter crystallization investigated in the shear cell of the rheometer. Pictures were taken without magnetic field, and without lowering the shear cell into the magnet. The cocoa butter reached the temperature of the shear cell within approximately one minute. The temperature of the cocoa butter stayed constant during the whole experiment. At first the cocoa butter was transparent, and the laser beam passed through without significant scattering. The cocoa butter then started to scatter the laser light, indicating formation of crystal nuclei. This did not affect the viscosity yet, which stayed constant. The cocoa butter then became increasingly turbid, and a sharp rise in viscosity occurred. The laser light no longer passed through the sample. The viscosity continued to rise, until the experiments were stopped at $5\,\mathrm{Pa\,s}$. The cocoa butter continued to harden out and the color changed from yellow to white. The cocoa butter then contracted, which is clearly visible in the last picture. This contraction is due to crystal transformation and was investigated in the static crystallization experiments with DSC in chapter 4.3.2.

Fig. 4.4 shows the decrease of the laser light intensity passing through the sample as well as the increase in viscosity, corresponding to the crystallization process as described above. This sample was crystallized at $21\,℃$ at a shear rate of $150\,\mathrm{s}^{-1}$. The laser intensity started to decrease right at the start of the measurement, indicating that cristal nuclei are formed right at the beginning of the experiment. This was true for all experiments, with and without magnetic field.
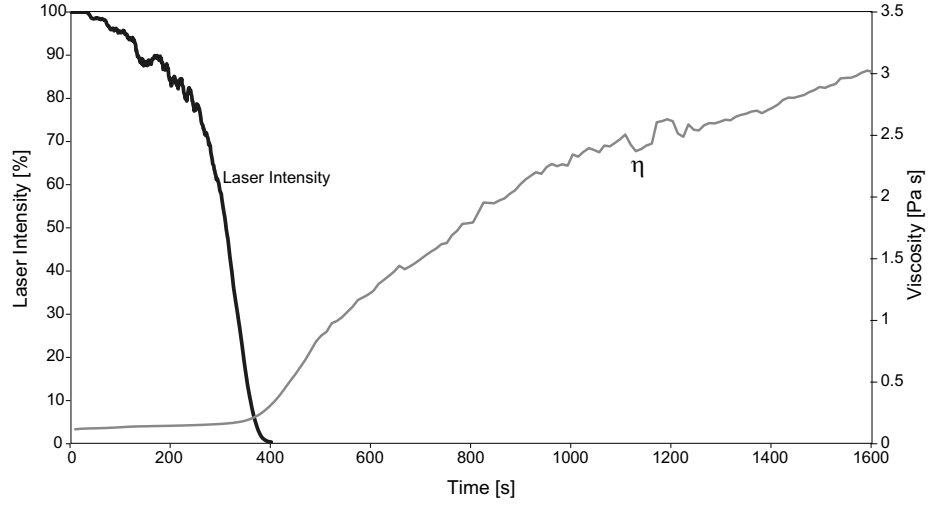
Figure 4.4: Crystallization of cocoa butter in the magnet rheometer at 21 °C and a shear rate of 150 s^{-1}, without magnetic field, corresponding to Fig. 4.5. Cocoa butter was filled into the sample holder at 50 °C and then cooled down. The laser intensity passing through the sample decreases from the start of the experiment, followed by an increase in viscosity.

For the shear crystallization experiments, the onset time of crystallization was determined as the time when the viscosity reached three times the averaged viscosity of the stationary phase, which was the initial viscosity at the beginning of the experiment. Average and standard deviation of three crystallizations with and three without magnetic field of 5.66 T were compared.

Fig. 4.6 shows the crystallization times obtained at a shear rate of 89.4 s^{-1} and a temperature of 26 °C. The crystallization time was 73.2±32.2 min without magnetic field, 48.5±22.4 min with magnetic field. The crystallization time obtained under the same conditions without magnetic field in a Physica rheometer was 165.3±7.3 min . At 150 s^{-1} and temperature of 21 °C the crystallization time was 8.6±0.1 min without magnetic field and 7.3±1.3 min at 5.66 T.

Figure 4.5: Crystallization of cocoa butter in the magnet rheometer at 21 °C and a shear rate of $150\,\mathrm{s^{-1}}$, without applied magnetic field. Cocoa butter was filled into the sample holder at 50°C and then cooled down. Top to bottom: liquid and transparent cocoa butter; liquid cocoa butter with crystal nuclei scattering the laser beam, solidifying cocoa butter with increasing viscosity, solid cocoa butter, solid cocoa butter after contraction
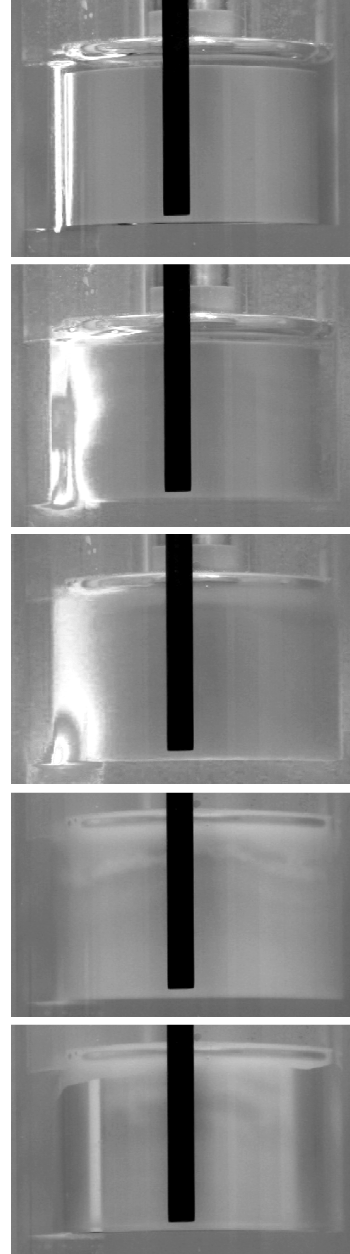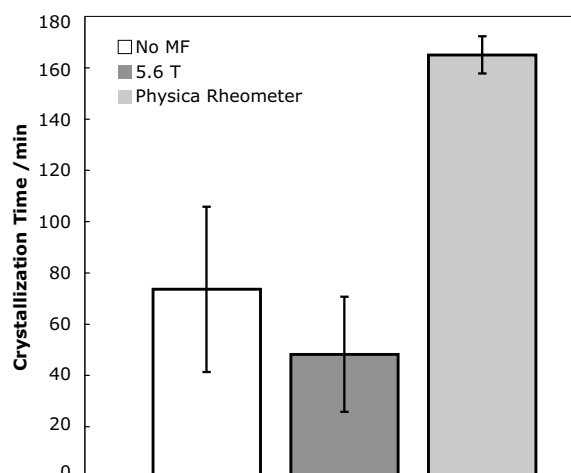
Figure 4.6: Onset of crystallization of cocoa butter sheared at $89.4\,\mathrm{s^{-1}}$ at $26\,℃$ with and without magnetic field in the magnet rheometer, as well as without magnetic field in a Physica rheometer, revealed by a sharp increase in viscosity. The onset of crystallization was determined as the time when the viscosity of the cocoa butter reached three times the average viscosity of the liquid cocoa butter during the stationary phase at the beginning of the experiment. MF; magnetic field.

For both conditions tested the average of the crystallization onset was earlier with magnetic field. However, the effect was smaller than the standard deviation, and can therefore not be considered to be significant. Comparison of the crystallization times obtained at the two conditions tested shows that, as expected, the crystallization happened a lot faster at a shear rate of $150\,\mathrm{s^{-1}}$ and temperature of $21\,℃$. In the Physica rheometer the crystallization times were more reproducible than in the magnet rheometer set up. The smaller standard deviation indicates that the temperature control of the Physica rheometer was still better than the one of the magnet rheometer. The temperature was logged for experiments made in the magnet rheometer, and was within a range of $0.3\,℃$ for all experiments made. The crystallization times were significantly higher in the Physica rheometer. This could be due to the fact that the Physica rheometer had no cover on top of the shear cell. The cocoa butter was therefore exposed to room temperature, which was well above $21\,℃$ at the time of the measurements.
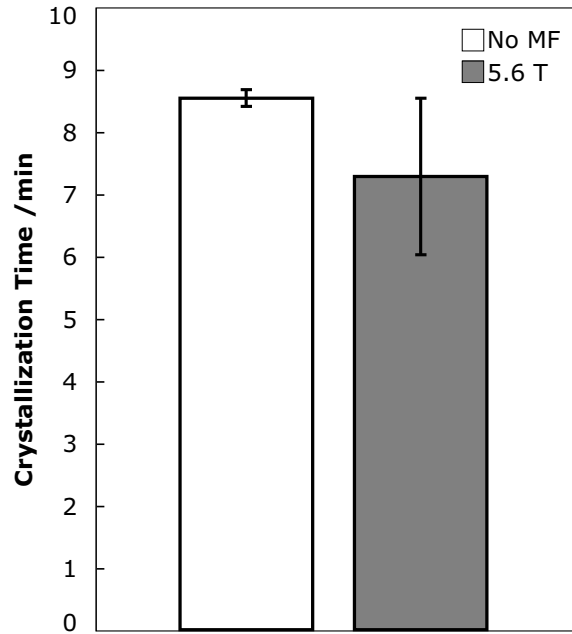
Figure 4.7: Onset of crystallization of cocoa butter sheared at $150\,\mathrm{s}^{-1}$ at 21 ℃ with and without magnetic field, revealed by a sharp increase in viscosity. The onset of crystallization was determined as the time when the viscosity of the cocoa butter reached three times the average viscosity of the liquid cocoa butter during the stationary phase at the beginning of the experiment.

4.3.2 Static Crystallization

Pre-tests of static crystallization were made in the magnet rheometer set up by crystallizing a large volume of 10 ml of cocoa butter directly in the shear cell, without installing the rheometer bob. Samples were taken with a hollow tube in periodic intervals over a period of four days and immediately analyzed with DSC. While it was possible to observe the general trend to recrystallize from form βIV to βV, curves obtained from different samples taken at the same time were not reproducible. It appears that a heterogeneous crystal transformation took place with local deviations of up to 12 h in the crystal transformation progress. It was therefore not possible to evaluate the significance of a possible magnetic field effect.

It was therefore decided to crystallize the cocoa butter in very small quantities directly in DSC crucibles. Before deciding on the sample weight to be used, DSC curves were recorded of crucibles filled with $5\,\mu$g and $20\,\mu$g without magnetic field. The

crucibles were kept at 22 °C and DSC curves were recorded every couple of hours for 3 days. Results showed that the reproducibility of the obtained crystal forms was greatly enhanced for both sample volumes. While the time dependency of the crystal morphology was similar for the two sample volumes investigated, the melting peaks were sharper and more reproducible with the 5 µg samples. Therefore, the experiments were made with 5 µg.

The results from static crystallization are shown in Fig. 4.8 to 4.11. Averaged DSC curves of up to six samples per measurement time are shown, taken over a period of three days. The measurement series at 20 °C (Fig. 4.8 and 4.9) show a peak at around 27 °C, which gradually disappears over a period of around 47 h. A second peak becomes more and more pronounced at around 30 °C to 34 °C. These two peaks represent two different crystal morphologies, and have been well described. The lower melting peak can be attributed to the βIV polymorph crystals, the higher melting peak to the βV polymorph. The observed melting temperatures are in agreement with literature. At 22 °C (Fig. 4.10 and 4.11), the βIV peak is not as clearly discernible as for the 20 °C series. Again, only the βV peak remains at the end of the measurement. The difference in the obtained DSC curves between 22 °C and 20 °C can be explained by the faster crystal transformation at higher temperatures.

Comparison of the crystallization with and without magnetic field shows no significant difference. For both crystallization temperatures, the first observed peaks represent a mixture of βIV and βV, which end up in pure βV form. The magnetic field therefore does not seem to influence the type of crystal formed. The speed of crystal transformation from βIV to βV does not seem to be significantly influenced by the magnetic field either.
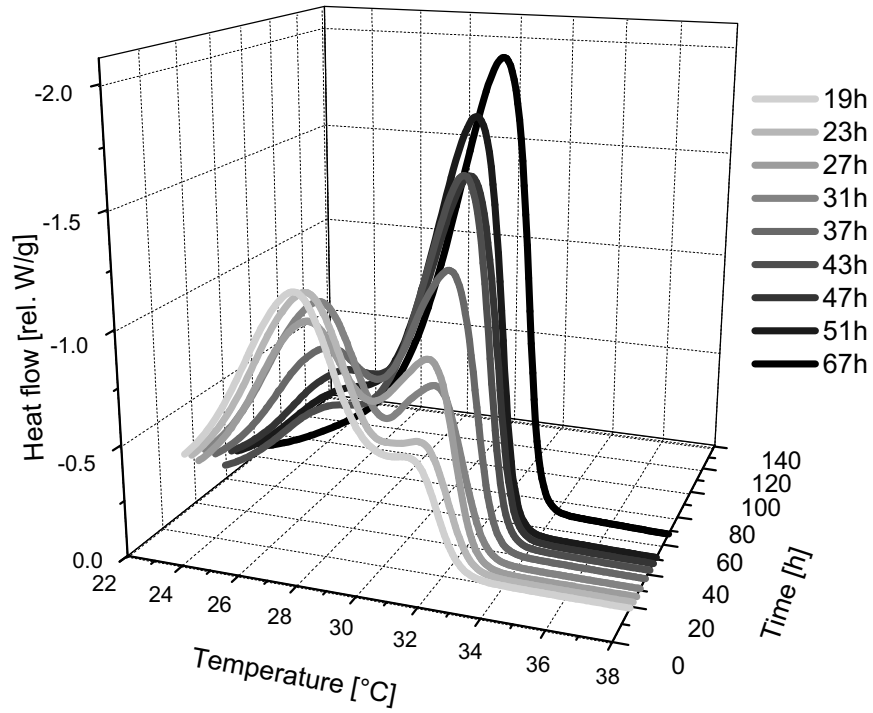
Figure 4.8: DSC curves of cocoa butter stored at 20°C at 5.66 T
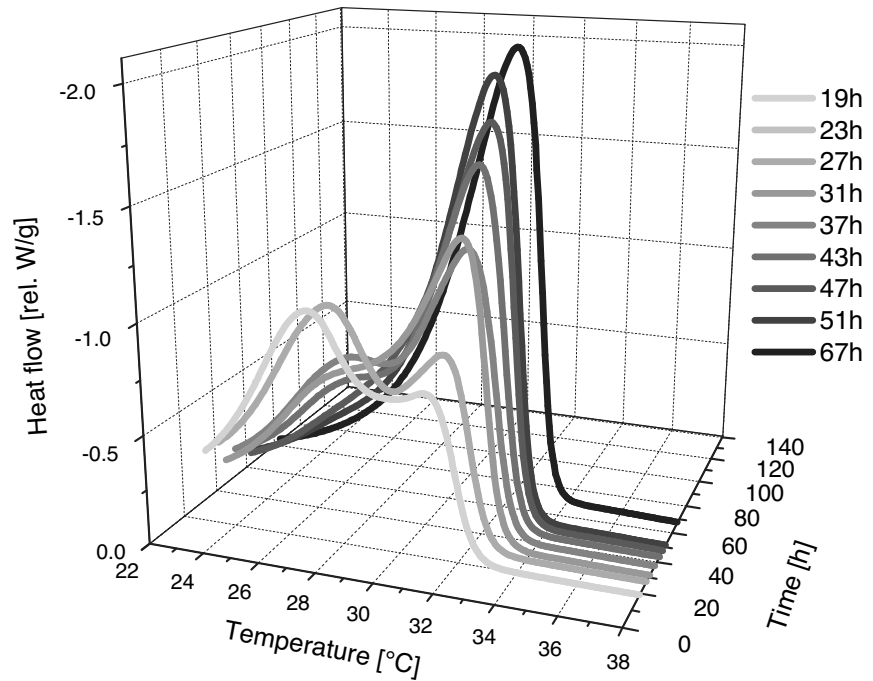
Figure 4.9: DSC curves of cocoa butter stored at 20°C at 0 T
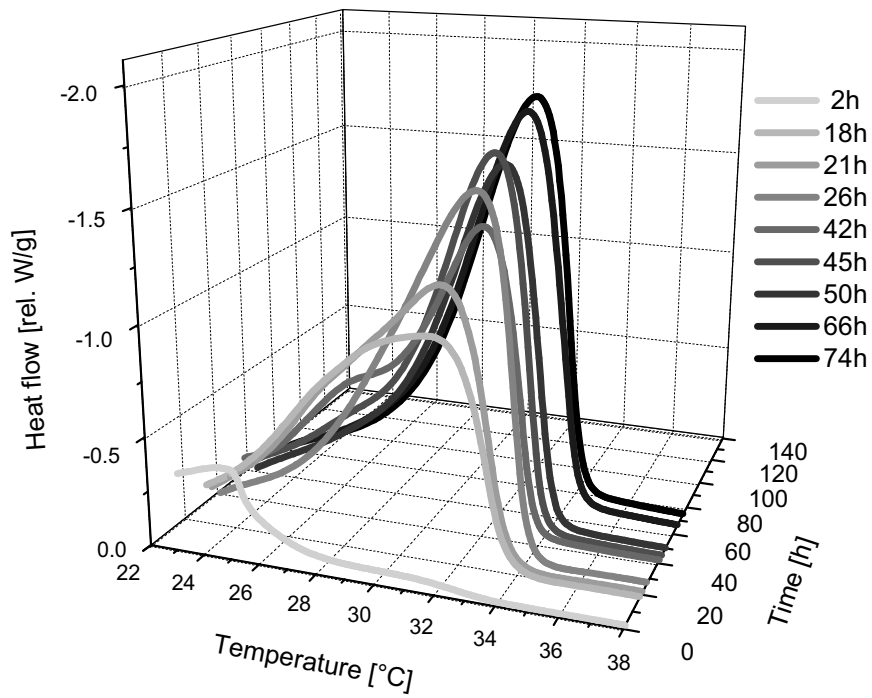
Figure 4.10: DSC curves of cocoa butter stored at 22°C and 5.66 T
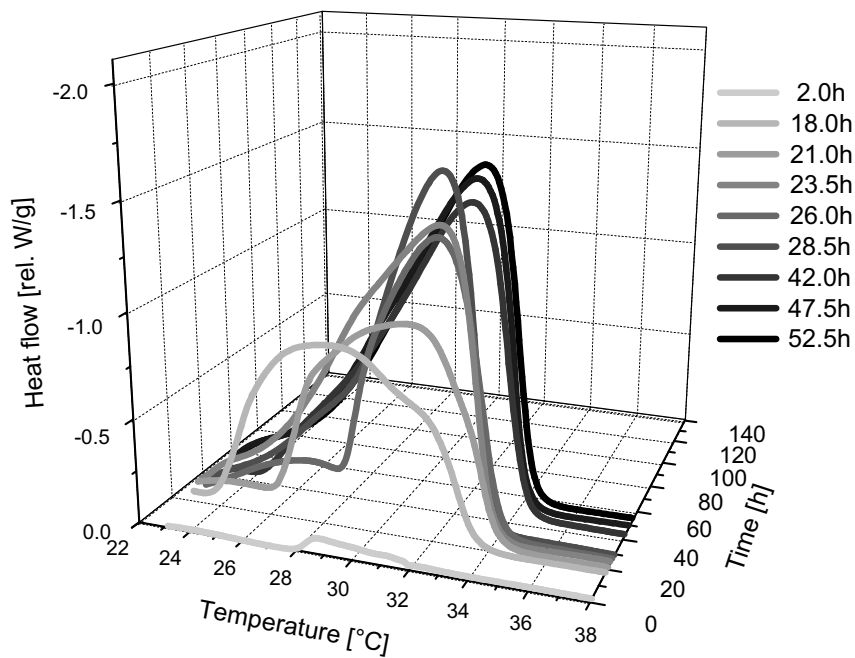
Figure 4.11: DSC curves of cocoa butter stored at 22°C and 0 T

4.4 Conclusion

The effect of a 5.66 T magnetic field on the crystallization behavior of cocoa butter was investigated. Both crystallization under shear and static crystallization measurements were made. For crystallization under shear, the speed of crystallization from a cocoa butter melt was investigated, indicated by a sharp rise in viscosity. For static crystallization tests, both the type of crystal formed during crystallization, as well as the speed of crystal transformation from one crystal polymorph to another was investigated, indicated by the melting range of the formed cocoa butter crystals obtained with DSC measurements. For the conditions investigated, no significant influence of the magnetic field was found. It is unclear, whether the heterogeneous composition of cocoa butter hindered a significant magnetic field effect because of the complexity of the crystal structures formed, or whether the experimental conditions were not suitable for a significant magnetic field interaction. The rather high viscosity of cocoa butter could have hindered a possible magnetic field effect, such as a pre-orientation of crystal nuclei. While it is known that the alkyl chains of the triglycerides exhibit an anisotropy of the diamagnetic susceptibility (Helfrich, 1973; Prosser *et al.*, 1998a; Qiu *et al.*, 1993), it is difficult to estimate the responsivity of triglycerides to magnetic fields. It is however probable that the magnetic anisotropy of individual molecules is insufficient to overcome the disorienting thermal fluctuation. It is therefore possible that the cocoa butter crystal size needed for a response to the magnetic field is attained only at a crystallization stage where the crystal morphology is already set and can no longer be influenced by the magnetic field.

Additional experiments in stronger magnetic fields, eventually coupled with a strong field gradient could be considered, as described in the introduction. Under strong field gradients, magnetic orientation of crystal nuclei could in theory be coupled with a damping of natural convection, which occurs due to density difference between the compact crystals and the liquid cocoa butter fraction (Yamaguchi and Tanimoto, 2006). As observed for crystallizing proteins, this may also have an effect on the crystal quality (Lin *et al.*, 2000).

5 Vesicles

5.1 Introduction

Magnetic field effects on biological molecules are rarely observed, due to the small diamagnetic susceptibility of individual molecules. In self-assembly systems, such as phospholipid bilayers, where the molecules are aggregated parallel to each other, the anisotropy of the diamagnetic susceptibility becomes additive (Qiu *et al.*, 1993) and a magnetic orientation perpendicular to the magnetic field becomes possible. A well known system, where this magnetic orientation has been exploited, is a bicellar mixture of long and short chain phospholipids used in NMR studies of transmembrane proteins (De Angelis and Opella, 2007; Katsaras *et al.*, 2005; Triba *et al.*, 2005; van Dam *et al.*, 2004). By doping these planar aggregates with paramagnetic lanthanides conferring a large magnetic moment, the responsiveness to magnetic fields can be enhanced (Prosser *et al.*, 1998b).

Lanthanides can be classified into two groups, depending on the sign of the magnetic anisotropy $\Delta\chi$. Phospholipids doped with a paramagnetic lanthanide from the first group (Ce^{3+}, Pr^{3+}, Nd^{3+}, Sm^{3+}, Tb^{3+}, Dy^{3+}, Ho^{3+}) have a large negative $\Delta\chi$ resulting in a preferred orientation with the long molecular axis perpendicular to the magnetic field. On the other hand, $\Delta\chi$ of phospholipids doped with Eu^{3+}, Er^{3+}, Tm^{3+} or Yb^{3+} becomes positive resulting in a preferred alignment in direction of the magnetic field. Doping phospholipids with diamagnetic lanthanum ions (La^{3+}) has no influence on the magnetic anisotropy of the phospholipids. The lanthanide cations are usually anchored to the membrane with the use of a chelator covalently bound to a phospholipid (Prosser *et al.*, 1998b). Such chelator molecules (e.g. DMPE-DTPA) have also been anchored into phospholipid vesicles. Complexed with Gd^{3+}, these vesicles have been investigated as a potential MRI contrast marker (Grant *et al.*, 1989).

In this study the effect of magnetic fields on phospholipid vesicles containing a chelator-lipid with complexed paramagnetic lanthanides was investigated. Of interest was whether the physico-chemical properties of such systems can be influenced by

magnetic fields. Possible magnetic field effects were deformation, aggregation/fusion, budding/fission, permeability and lateral segregation. For pure phospholipid vesicles, in the absence of any added lanthanides, a few such effects have been described. It has been shown for example, that vesicles can slightly be deformed and oriented in magnetic fields (Brumm *et al.*, 1992; Helfrich, 1973; Kiselev *et al.*, 2006, 2008; Reinl *et al.*, 1992). Influence of magnetic fields on permeability has been claimed by Liburdy *et al.* (1986); Tenforde and Liburdy (1988). Kurashima *et al.* (2002) reported on magnetic field induced fusion of vesicles.

Lateral lipid segregation and domain formation in the absence of magnetic fields has been described for multicomponent phospholipid vesicles, mostly prepared from mixtures of DOPC (1,2-dioleoyl-*sn*-glycero-3-phosphocholine), DPPC (1,2-dipalmitoyl-*sn*-glycero-3-phosphocholine) and Cholesterol. These systems have gained increasing interest in recent years as a model for lipid rafts in biomembranes (Anghel *et al.*, 2007; Bacia *et al.*, 2005; Baumgart *et al.*, 2003; Hartmann *et al.*, 1977; Imai, 2007; Korlach *et al.*, 1999; Lipowsky and Dimova, 2003; Masui *et al.*, 2006; Pencer *et al.*, 2005a, 2008; Seifert, 1993; Veatch and Keller, 2002; Yanagisawa *et al.*, 2007).

This work reports on investigations of different formulations of vesicles at different temperatures and under different magnetic field strengths. As standard sample vesicles composed of a mixture of $80 \, \text{mol\%}$ POPC and $20 \, \text{mol\%}$ DMPE-DTPA with complexed thulium ions (Tm^{3+}) were used. Additional formulations varied in one of the three components or in the ratio of POPC:DMPE-DTPA. Small angle neutron scattering (SANS) under magnetic field, complemented by direct observation of the structures at two different temperatures by cryo transmission electron microscopy (cryo-TEM) was used. Additional information was gained through permeability measurements with watersoluble calcein, ^{31}P NMR, dynamic light scattering (DLS) and differential scanning calorimetry (DSC).

5.2 Material and Methods

5.2.1 Material

The phospholipids, 1,2-dimyristoyl-*sn*-glycero-3-phosphocholine (DMPC), 1-palmitoyl-2-oleoyl-*sn*-glycero-3-phosphocholine (POPC), 1-stearoyl-2-oleoyl-*sn*-glycero-3-phosphocholine (SOPC) and 1,2-dimyristoyl-*sn*-glycero-3-phosphoethanolamine-diethylene-triamine-pentaacetate (DMPE-DTPA), were purchased as chloroform solutions from Avanti Polar Lipids (Alabaster, AL) and used without further purification. 1-palmitoyl-2-oleoyl-*sn*-glycero-3-phosphoethanolamine diethylene triamine pentaacetate (POPE-DTPA) was synthesized according to a modified approach described by Torchilin *et al.* (2003). $TmCl_3$ (99.9%), $LaCl_3$ (99.9%), $DyCl_3$(99.9%), calcein disodium salt (99.9%), Sepharose 4B, D_2O (99.9 atom %D) used for ^{31}P NMR samples and D_2O (99.9 atom %D, containing 0.05 wt% 3-(trimethylsilyl)propionic-2.2.3.3-d4 acid, sodium salt) used for SANS and cryo-TEM samples were from Sigma-Aldrich (Buchs, Switzerland). Stock solutions of 10 mM $TmCl_3$ and $DyCl_3$ in MeOH and of 10 mM $LaCl_3$ in MeOH/H_2O (19/1 v/v) were prepared.

5.2.2 Vesicle Preparation

After weighing the dissolved lipids and lanthanides into a round bottom flask, the chloroform and methanol were evaporated under a rotary evaporator followed by residual solvent removal under high vacuum overnight. The so formed dry lipid film was hydrated with D_2O and vortexed until a homogeneous suspension was obtained. Five repeated freeze - thaw cycles were carried out by plunging the flask into liquid nitrogen followed by slow heating above the phase transition temperature (about 40 to 45 °C). An extrusion was performed under nitrogen at room temperature with "The Extruder" from Lipex Biomembranes (Vancouver, Canada) using Nucleopore polycarbonate membranes from Sterico (Dietikon, Switzerland). The suspension was first passed 10 times through a membrane with 200 nm pores, followed by 10 times through a membrane with 100 nm pores, except for the sample with 200 nm vesicles, where the 100 nm extrusion step was omitted. All samples were prepared with a total lipid concentration of 15 mM. The standard sample consisted of a POPC:DMPE-DTPA:Lanthanide molar ratio of 4:1:1. The samples are denoted as POPC/DMPE-DTPA·Tm, POPC/DMPE-DTPA·La, or POPC/DMPE-DTPA·Dy in the text, depending on the lanthanide used, and POPC/DMPE-DTPA if no lanthanide was complexed. The sample with 200 nm vesicles and standard formulation

is denoted as POPC/DMPE-DTPA·Tm$_{200nm}$. The sample denoted as POPC/POPE-DTPA·Tm was prepared with POPE-DTPA instead of DMPE-DTPA, with the same component ratio. One sample with a DMPC:DMPE-DTPA:Tm molar ratio of 4:2:2 was prepared, denoted as DMPC/highDMPE-DTPA·Tm. One pure phosphocholine sample, POPC/DMPC with a lipid ratio of 4:1 was prepared. Samples were stored at room temperature before measurements and were stable over at least two weeks.

5.2.3 SANS

SANS experiments were performed on the SANS-I beam line at PSI, Villigen, Switzerland using a super conductive magnet with horizontal field of 8 T perpendicular to the neutron beam. The neutron wavelength was fixed at 8 Å. Data was collected on a two-dimensional ^{3}He detector at distances of 2, 6, and 18 m covering a momentum transfer q of $0.003 \leq q \leq 0.15$ Å^{-1}. After correction for background radiation, empty cell scattering and detector efficiency, the 2D intensity maps were radial averaged (Fig. 5.1c) and sectoral averaged with an opening angle of 15° perpendicular (Fig. 5.1a) and parallel (Fig. 5.1b) to the magnetic field direction.
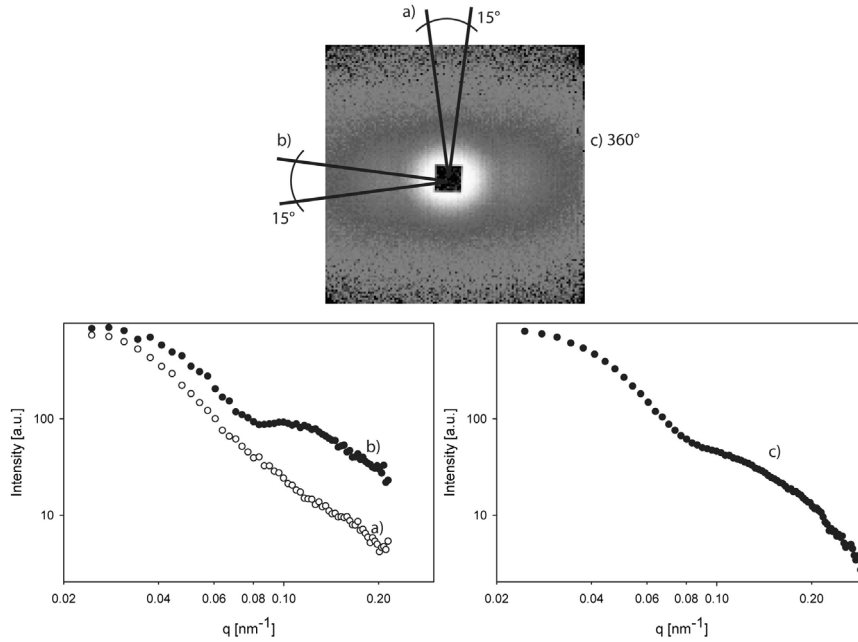
Figure 5.1: Data reduction of SANS 2D scattering pattern: radial intensity average over the full detector (c) and sectoral intensity average with an opening angle of 15° perpendicular (a) and parallel (b) to the magnetic field direction.

5.2.4 Cryo-TEM

The samples were analyzed by cryotransmission electron microscopy (cryo-TEM). A volume of $3.5\,\mu$l of the vesicular suspension was mounted onto holey carbon grids (from Quantifoil, Jena, Germany), blotted to make thin aqueous films under controlled temperature, followed by plunging into liquid ethane at the temperature of liquid nitrogen ($-196\,°$C). For samples frozen at room temperature a VitrobotTM apparatus (from the FEI company, Eindhoven, The Netherlands) was used for automatized blotting. For the samples frozen from $5\,°$C, the sample was pre-cooled in a waterbath and a manual blotting apparatus was transferred into a cold room with $5\,°$C $\pm\,0.5\,°$C. Every part of equipment coming into contact with the sample was held for at least $4\,$h in the cold room prior to sample freezing. The grids were examined at the temperature of liquid nitrogen using a cryo-holder (model 626, from Gatan, USA) and a Tecnai G2 F20 microscope (from the FEI company) equipped with a field emission gun and Tridem energy filter (from Gatan) operated at an accelerating voltage of $200\,$kV. The data were recorded by a 2048×2048 CCD camera (from Gatan).

5.2.5 ^{31}P NMR

^{31}P NMP spectra were acquired at $283\,$MHz using a Bruker Biospin $750\,$MHz spectrometer with $16.4\,$T in the bore. Temperature was adjusted with a nitrogen gas flow.

5.2.6 DSC

Differential scanning calorimetry (DSC) measurements were made with a DSC-7 calorimeter (Perkin Elmer, Waltham MA, USA) and analyzed with the Pyris version 5 software (Perkin Elmer, Waltham MA, USA). The scanning range was typically between $-5\,°$C and $45\,°$C at a scanning rate of $5\,°$C per minute. Sample weight was $4\,$mg. Repeat scans were made after equilibrating the temperature for $30\,$min. The curves were reproducible.

5.2.7 DLS

The instrument used for dynamic light scattering (DLS) experiments was a BI-200SM goniometer (Brookhaven Instruments Corporation (BIC), Holtsville, NY, USA), with a diode laser (Adlas/Coherent, Lübeck, Germany) operating at a wavelength of 532 nm. The scattering angle was set to 90°. DLS experiments measure the intensity autocorrelation function, and its decay rate determines the translational diffusion coefficient of the vesicles in the system. The hydrodynamic diameter of the vesicles can then be estimated from the translational diffusion coefficient. Data were analyzed using the MAS option of BICs particle sizing software (version 3.48). The number-weighted size distribution was used for a better comparability with size distributions gathered by cryo-TEM (Egelhaaf *et al.*, 1996). Samples were diluted to 0.1 mM total lipid concentration.

5.2.8 Permeability Measurements

For permeability measurements, vesicles were prepared with the same method as described in chapter 5.2.2, but instead of rehydrating the films with D_2O, a 50 mM calcein solution of pH 7 was used. After extrusion, size exclusion chromatography through a Sepharose 4B column was performed to remove unencapsulated calcein. As eluent a NaCl solution with the same osmolarity as the calcein solution was used (250 mOsm, around 8 g NaCl/l). Samples were kept at room temperature. For the experiments, 1 ml of the sample was divided into two thin walled glass vials. One vial was placed in a sample holder which was connected to a water bath. The circulating water was in direct contact with the glass vial. The sample holder was placed into the bore of a superconductive magnet (Cryogenic, London, UK) with adjustable magnetic field strength of up to 5.6 T. The other vial was placed into a second water bath. Temperature was logged from two sensors inserted into the glass vials. For the experiments made at 16.4 T, 1 ml of sample was divided into two NMR tubes. One was placed into the bore of the NMR magnet, the other in an external water bath.

The fluorescence of the suspension was measured with a Fluorescence Microplate Reader (Bio-Tek) at 516 nm with an excitation wavelength of 490 nm. For these measurements 50 μl or 100 μl samples were pipetted into a 96 microwell plate. Maximal fluorescence intensity I_{max} was measured after addition of 5 μl Triton X-100, which initiate building of micelles resulting in a complete release of calcein. Calcein standard curve (left) and the linearized range in the double logarithmic plot (right) is shown in Fig. 5.2.
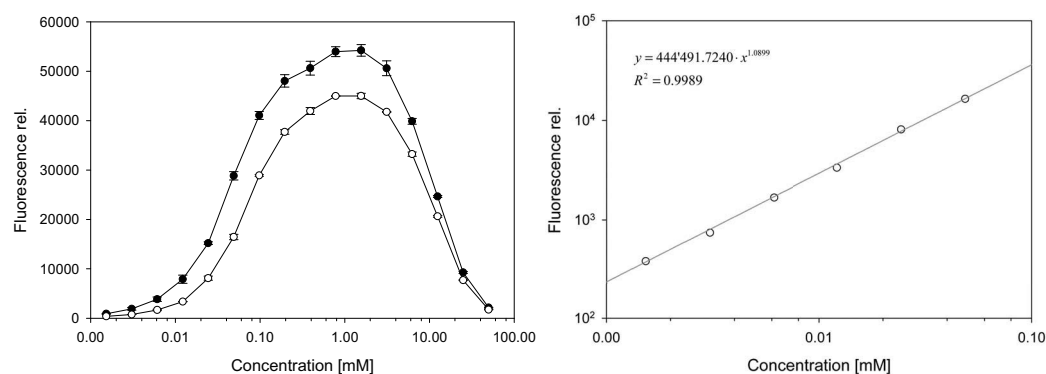
Figure 5.2: Calcein standard curve, filled circles: $100\,\mu$l; open circles: $50\,\mu$l. Double logarithmic plot shows the linearized range from $0.001\,\text{mM}$ to $0.1\,\text{mM}$ and the corresponding trend line (solid line) $y = 444'491.7240 \cdot x^{1.0899}$.

An overview over SANS, cryo-TEM, DLS and NMR measurements carried out is listed in Tab. 5.1.

Table 5.1: Overview over SANS, cryo-TEM, DLS and NMR measurements carried out.

Vesicle Formulation	SANS measurements detector position 18 m	SANS measurements additional detector positions	cryo TEM	DLS	NMR
POPC/DMPE-DTPA·Tm	30°C - 2.5°C at 8 T	6m at 30°C 8 T	22°C	22°C	
	2.5°C - 30°C at 8 T	6m and 2m at 2.5°C 8 T	5°C		
	30°C - 2.5°C at 0 T	6m at 2.5, 5 and 30°C 0 T			
	0 T - 8 T at 2.5°C				
POPC/DMPC	30°C - 2.5°C at 8 T	6m at 2.5 and 30°C 8 T	22°C 5°C	22°C	2.5°C 30°C
POPC/DMPE-DTPA·Dy	8 T - 4T at 2.5°C		22°C 5°C	22°C	
POPC/highDMPE-DTPA·Tm	2.5°C at 8 T		22°C 5°C	22°C	
POPC/POPE-DTPA·Tm	2.5°C at 8 T		22°C 5°C	22°C	
POPC/DMPE-DTPA·Tm$_{200nm}$			22°C 5°C	22°C	
POPC/DMPE-DTPA			22°C 5°C	22°C	
POPC/DMPE-DTPA·La			22°C 5°C 30°C		2.5°C 25°C 30°C

5.3 Results

5.3.1 SANS Measurements

In order to investigate whether a magnetic field has an influence on the structure of mixed phospholipid vesicles, in which one lipid is doped with a strong paramagnetic agent, SANS measurements under variable magnetic field and temperature were carried out. Most of these measurements were made of 100 nm vesicles composed of a mixture of POPC, DMPE-DTPA and Tm^{3+} in a molar ratio of 4:1:1. This suspension was considered as the standard sample. Measurements were also made on vesicles with related compositions, namely POPC/DMPE-DTPA·Dy and POPC/POPE-DTPA·Tm. POPC, DMPE-DTPA and Tm^{3+} in a molar ratio of 4:2:2 (POPC/highDMPE-DTPA·Tm) and finally a pure phospholipids sample, POPC/DMPC in a molar ratio of 4:1, were investigated as well.

POPC/DMPE-DTPA·Tm

Effect of temperature and strength of magnetic field on the scattering pattern was investigated. Fig. 5.3 shows the 2D scattering and the corresponding sectoral averaged curves for vesicles consisting of POPC/DMPE-DTPA complexed with Tm^{3+} at 8 Tesla at different temperatures, all measured with a detector position at 18 m covering a q range of 0.025 - 0.215 nm^{-1}. The molar ratio of POPC:DMPE-DTPA:Tm is 4:1:1, total lipid concentration 15 mM.

It is clearly visible that the scattering pattern is isotropic at temperatures above 17.5 °C. From 17.5 °C to 2.5 °C, the pattern becomes increasingly anisotropic. The scattering patterns are completely reversible without hysteresis, as was seen when the temperature was raised back to 30 °C. Cooling without magnetic field from 30 °C to 2.5 °C followed by ramping of the magnet to 8 T gave the same scattering pattern as shown in Fig. 5.3 H.

At 30 °C the SANS curves show an inflection at 0.08 nm^{-1}. At lower temperatures, the inflection disappears for the vertical sectoral average curves (open circles) and becomes more distinct in the horizontal sector (closed circles). Comparison of the scattering curves furthermore indicates that change in scattering pattern in vertical direction is much less pronounced than in horizontal direction.

A) 30°C
8 T

B) 22°C
8 T

C) 17.5°C
8 T

D) 15°C
8 T
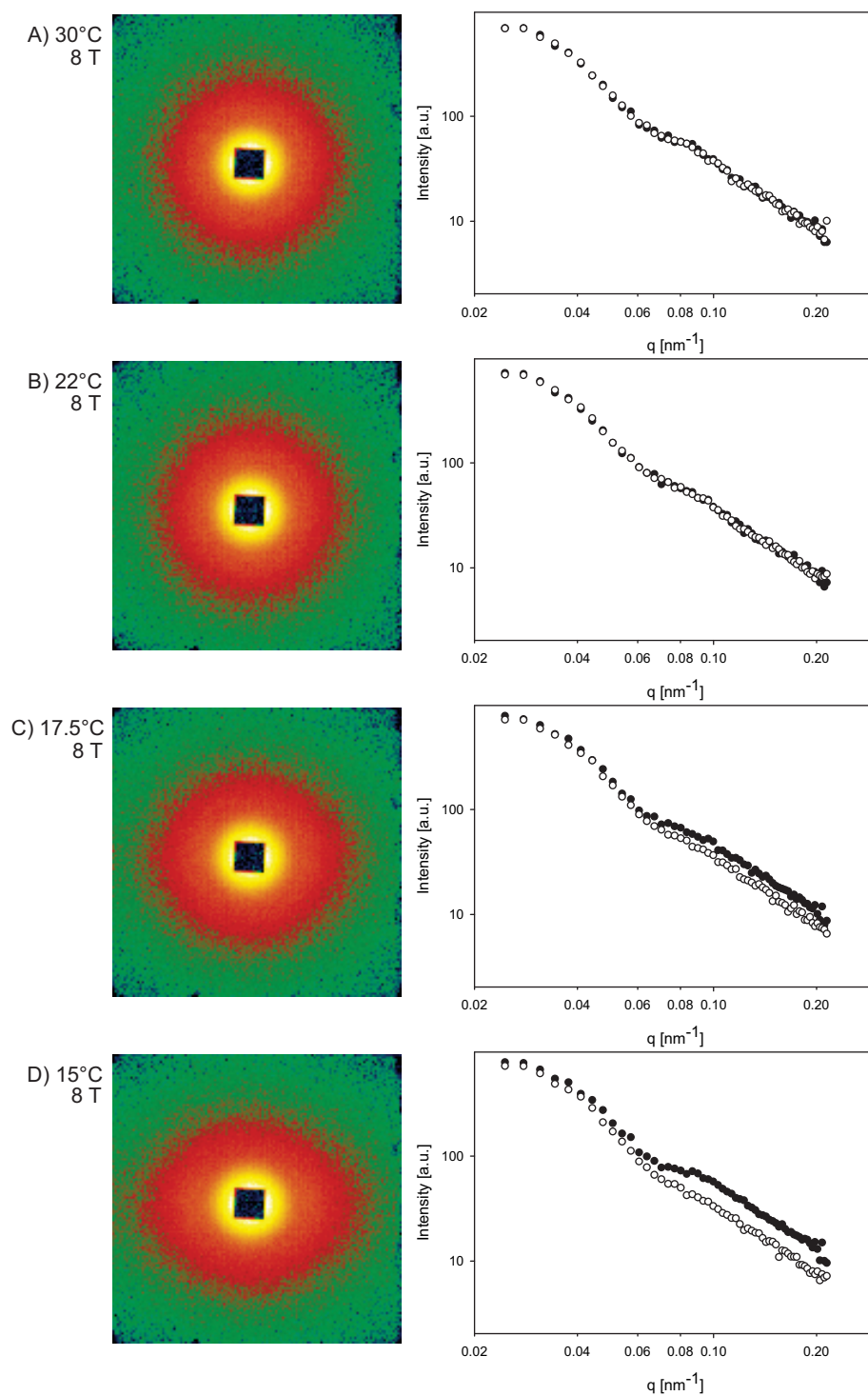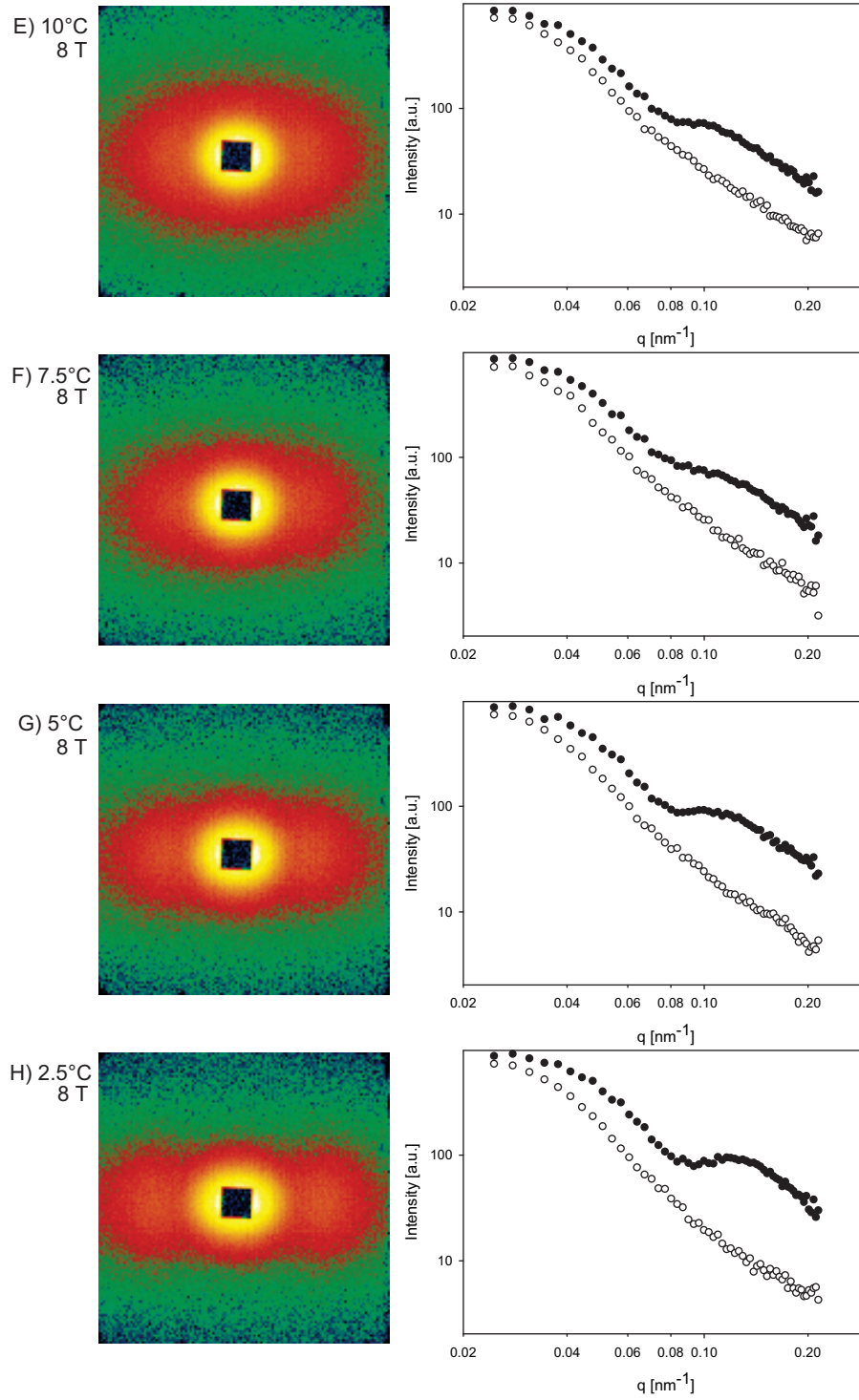
Figure 5.3

Figure 5.3: 2D SANS scattering patterns and corresponding sectoral intensity average at different temperatures and a magnetic field of 8 T of vesicles consisting of POPC/DMPE-DTPA·Tm. Open circles: Vertical 15° intensity average, closed circles: Horizontal 15° intensity average. Magnetic field direction is horizontal in the plane.

At 2.5°C the influence of the magnetic field strength was studied. Lowering the magnetic field stepwise from 8 to 0 T leads to a gradual decrease of the anisotropy in the scattering pattern ending in an isotropic pattern at 0 T (Fig. 5.4). This effect is also reversible.

Figure 5.4

Figure 5.4: 2D SANS scattering patterns and corresponding sectoral intensity average at 2.5 °C and different magnetic field strength of vesicles consisting of POPC/DMPE-DTPA·Tm. Open circles: Vertical 15° intensity average, closed circles: Horizontal 15° intensity average. Magnetic field direction is horizontal in the plane.

The POPC/DMPE-DTPA·Tm sample was also measured without magnetic field in the whole temperature range. As expected, without magnetic field the scattering patterns were isotropic at all temperatures, which is in clear contrast to the scattering patterns observed at 8 T. Fig. 5.5 shows the radial average of the isotropic scattering patterns. The two extreme temperatures, 30 °C and 2.5 °C, are marked with open and closed circles respectively. Changing the sample temperature had an effect on the whole q range. The changes in the scattering curves were complex, with all the curves intersecting at q values of 0.08 and 0.12 nm^{-1}. All these measuring results indicate, that the anisotropy is an effect of the magnetic field.

Figure 5.5: 2D SANS scattering pattern of vesicles consisting of POPC/DMPE-DTPA·Tm³⁺ at 30 °C (left) and radial averaged SANS curves at different temperatures (right), at 0 T. Open circles: 2.5 °C, closed circles: 30 °C, solid lines: temperatures in between.

POPC/highDMPE-DTPA·Tm
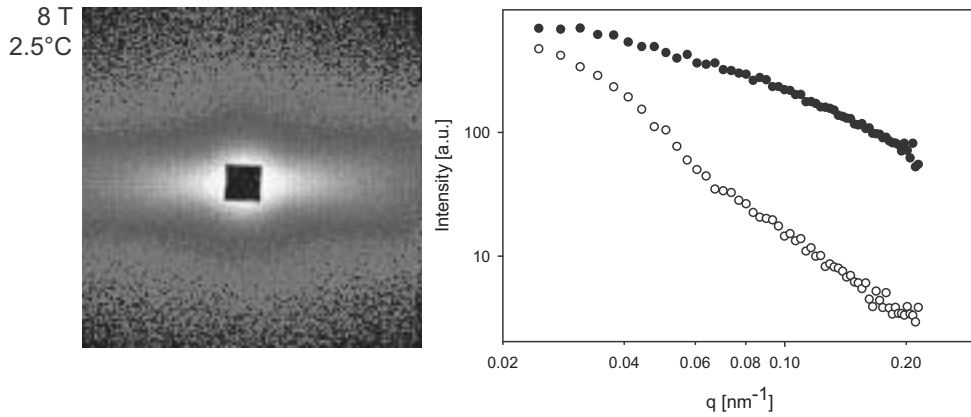
Figure 5.6: 2D SANS scattering pattern and corresponding sectoral intensity average at 2.5 °C and 8 T of vesicles consisting of POPC/highDMPE-DTPA·Tm. Open circles: Vertical 15° intensity average; closed circles: Horizontal 15° intensity average. Magnetic field direction is horizontal in the plane.

Scattering from vesicles with a higher molar ratio of 40 mol% DMPE-DTPA·Tm is clearly more anisotropic than from our standard vesicles, shown in Fig. 5.6. The measurement was carried out at 8 T and 2.5 °C, where for the standard sample the anisotropy was most pronounced. Open circles show the vertical, closed circles the

horizontal sectoral averaged scattering intensity. The molar ratio of POPC:DMPE-DTPA:Tm is 4:2:2, total lipid concentration 15 mM.

POPC/POPE-DTPA·Tm

Replacing the chelator lipid, DMPE-DTPA, with POPE-DTPA had a strong effect on the scattering anisotropy. The scattering pattern is only slightly anisotropic as shown in Fig. 5.7, measured at 8 T and 2.5 °C. The molar ratio of POPC:POPE-DTPA:Tm is 4:1:1, total lipid concentration is 15 mM.
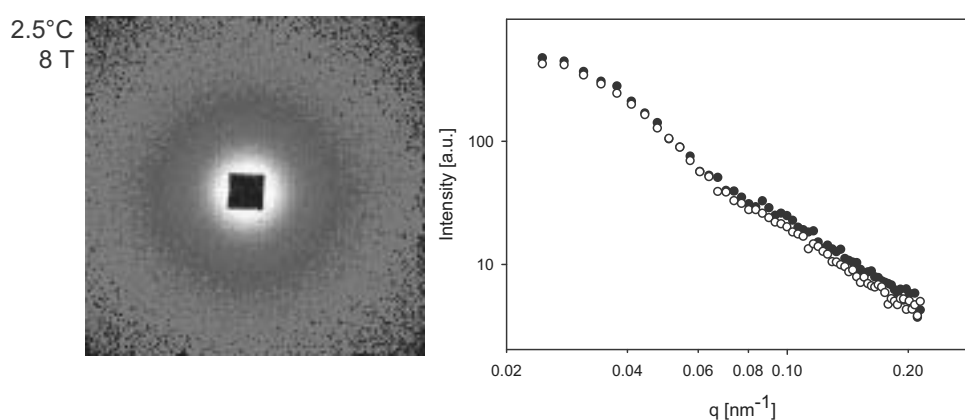
Figure 5.7: 2D SANS scattering pattern and corresponding sectoral intensity average at 2.5 °C and 8 T of vesicles consisting of POPC/POPE-DTPA·Tm. Open circles: Vertical 15° intensity average, closed circles: Horizontal 15° intensity average. Magnetic field direction is horizontal in the plane.

POPC/DMPE-DTPA·Dy
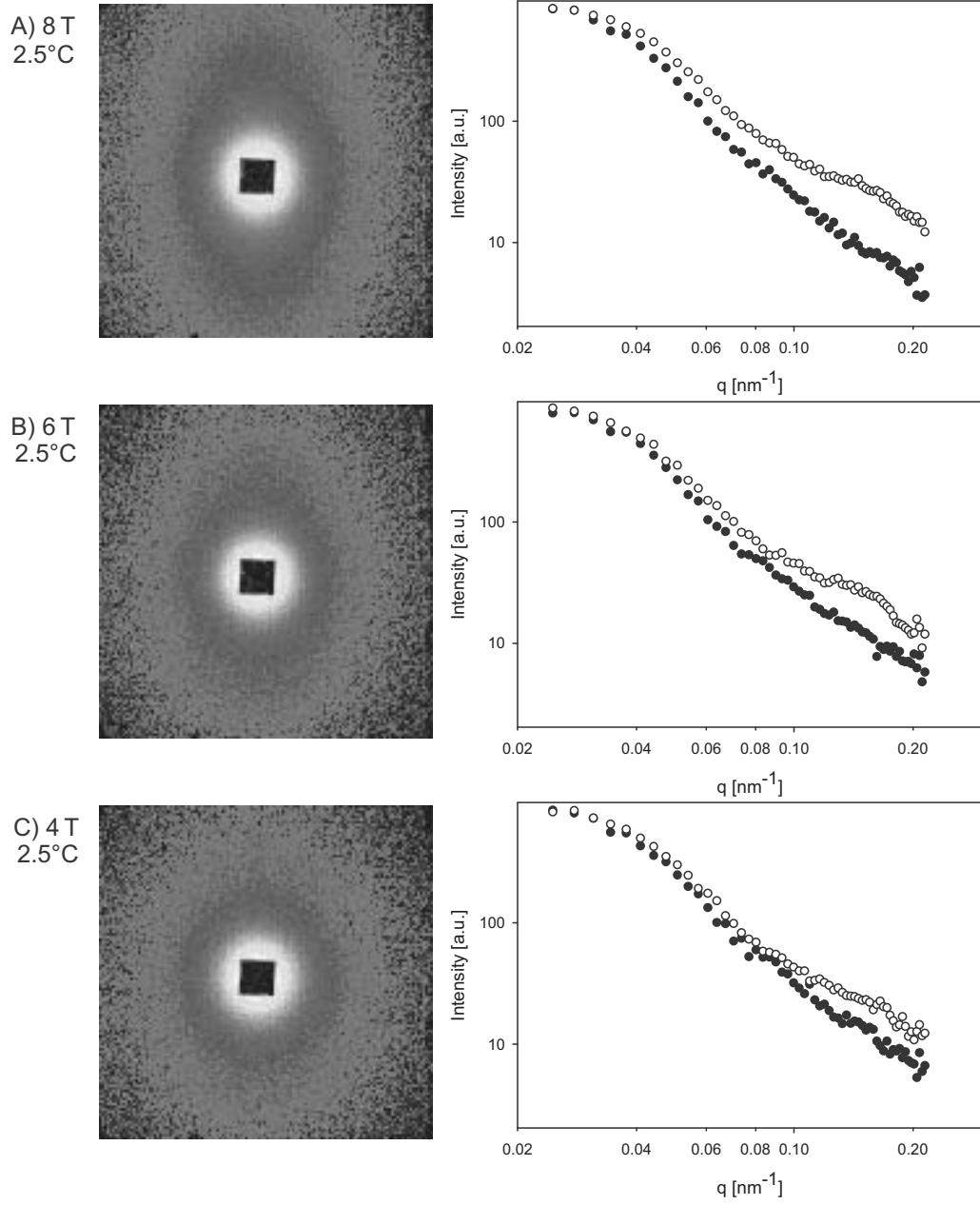
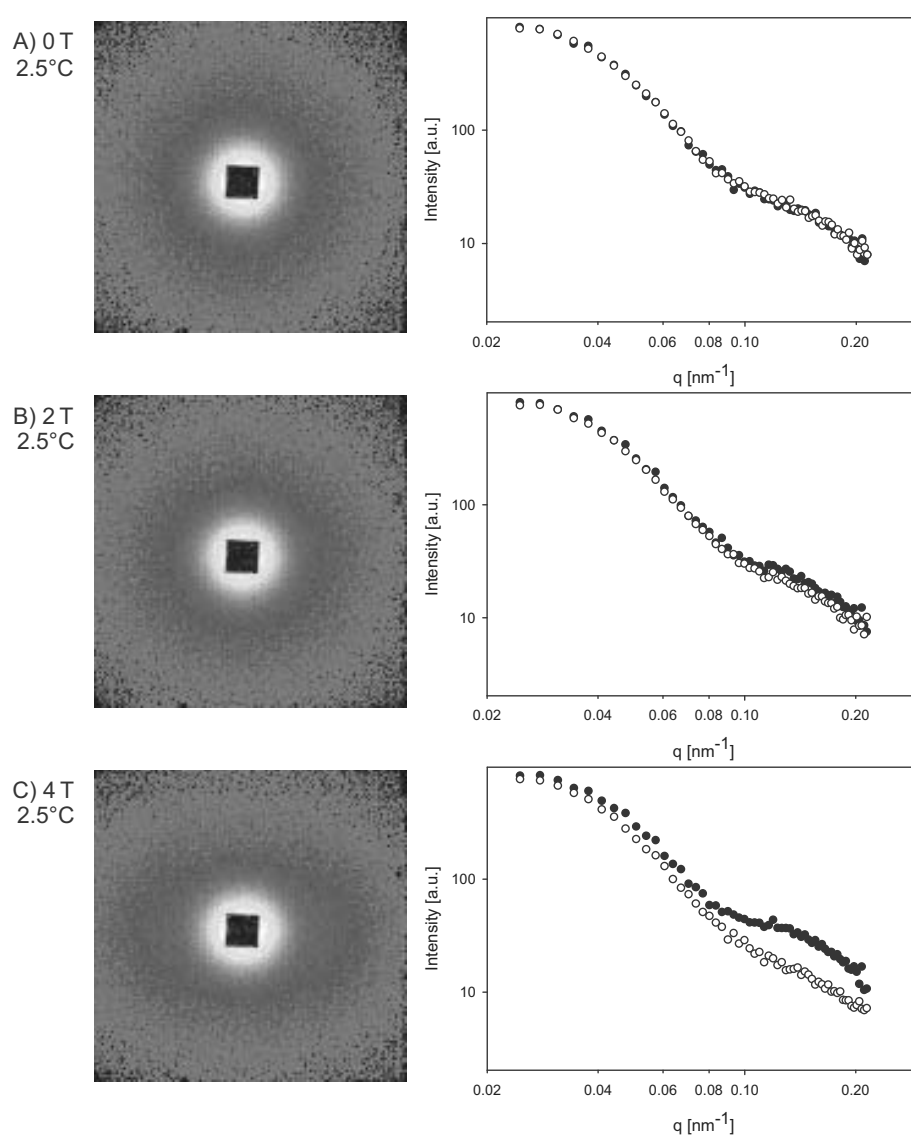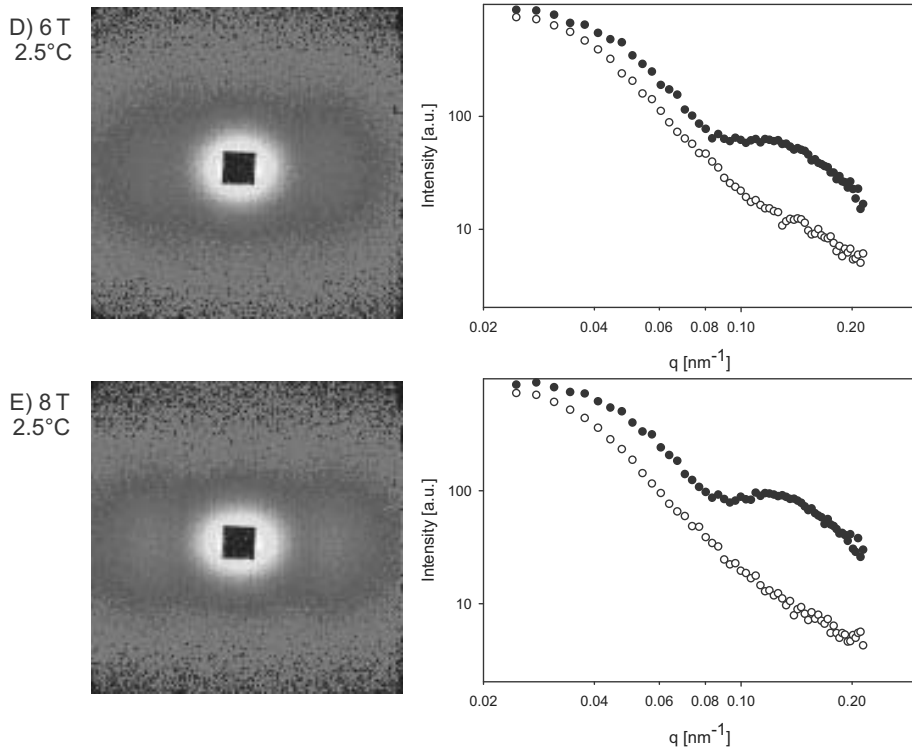Figure 5.8: 2D SANS scattering patterns and corresponding sectoral intensity average at 2.5 °C and different magnetic field strengths of vesicles consisting of POPC/DMPE-DTPA·Dy. Open circles: Vertical 15° intensity average, closed circles: Horizontal 15° intensity average. Magnetic field direction is horizontal in the plane.

DMPE-DTPA·Dy has an opposite sign of the anisotropy of the paramagnetic susceptibility than DMPE-DTPA·Tm. Of interest was whether this different magnetic property of the two lanthanides is reflected in the anisotropy of the scattering pattern. The effect of the magnetic field was investigated at 2.5 °C, where the most pronounced anisotropy was observed in the scattering pattern of POPC/DMPE-DTPA·Tm (Fig. 5.3 H). SANS data collected at 8, 6 and 4 T and 2.5 °C show that the anisotropy is still present, but is now pronounced in vertical direction (Fig. 5.8). Again the anisotropy of the scattering pattern increased with the magnetic field strength. Open circles show the vertical sectoral average and closed circles the horizontal sectoral average of the scattering intensity. The molar ratio of POPC:DMPE-DTPA:Dy was 4:1:1, the total lipid concentration was 15 mM.

POPC/DMPC

A sample where the chelator-lipid was replaced by a phosphatidylcholine with the same acyl-chains (DMPC) at the same molar ratio as the standard sample gave isotropic scattering patterns at all measured temperatures and 8 T. Fig. 5.9 shows the radial averaged intensity curves of all temperatures. Open circles show the 2.5 °C data, closed circles the 30 °C. The solid lines represent the temperatures measured in between. Unlike the curves for POPC/DMPE-DTPA·Tm (Fig. 5.5) the temperature dependent change for POPC/DMPC are mostly restricted to a q range of 0.07 to $0.1 \, \text{nm}^{-1}$.
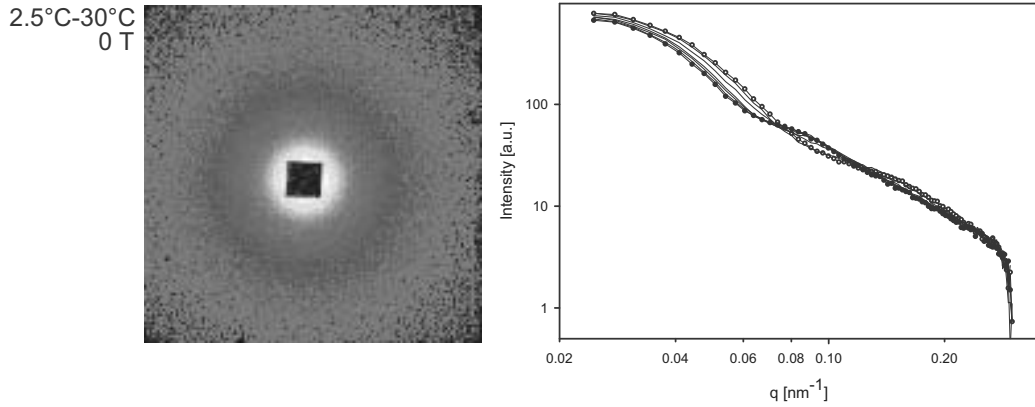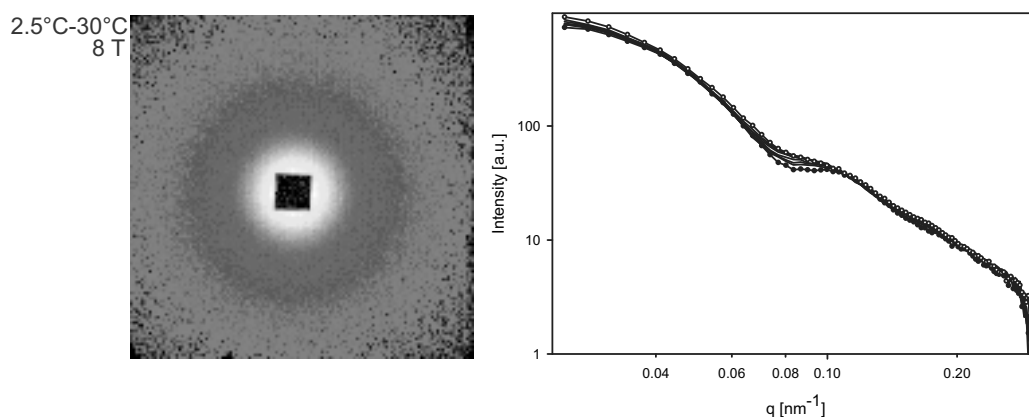

Figure 5.9: 2D SANS scattering pattern of vesicles consisting of 100 nm POPC/DMPC at 30 °C (left), and radial averaged SANS curves at different temperatures (right), at 8 T. Open circles: 2.5 °C, closed circles: 30 °C, solid lines: temperatures in between.

SANS measurements indicate that an anisotropy in the scattering pattern occurs below a critical temperature of about 22 °C for the lanthanide doped vesicle formulations. This anisotropy can only be seen above a certain magnetic field strength of about 2 T (Fig. 5.4).

5.3.2 Cryo-TEM Measurements

Cryo-TEM micrographs were taken in order to proof the existence of vesicles for all investigated samples, as well as to get information about the size distribution and the morphology of the vesicles. For POPC/DMPE-DTPA·Tm, the SANS pattern were isotropic above 17 °C and anisotropic at 17 °C and below at a magnetic field of 8 T. In order to find out whether a temperature dependent change in morphology can be seen without magnetic field, samples were frozen from room temperature, as well as from 5 °C. Fig. 5.10 shows the cryo-TEM micrographs of the standard vesicle sample POPC/DMPE-DTPA·Tm (A), vesicles of POPC/DMPE-DTPA·Tm$_{200nm}$ (B) and of POPC/highDMPE-DTPA·Tm (C). In all these samples most of the vesicles are unilamellar and relatively homogeneous in size. A few oligolamellar (arrows 1), and very few multivesicular vesicles (arrows 2) were found in all samples. As expected, the 200 nm vesicles in Fig. 5.10 B are clearly larger than the 100 nm samples and multilamellar vesicles are found (arrows 3). At closer examination the membrane of some vesicles, particularly those frozen from 5 °C looks somewhat edged, i.e. the vesicle is not perfectly spherical, but comprises flattened membrane segments. In Fig. 5.12, another micrograph of the standard sample (POPC/DMPE-DTPA·Tm) frozen from 5 °C, as well as a zoom in of the 5 °C micrograph of Fig. 5.10 A are shown. Arrows point to the above mentioned edged vesicles. Edged vesicles are also visible in Fig. 5.10 B and Fig. 5.10 C, particularly in the 5 °C micrographs.

Fig. 5.11 shows micrographs of three other vesicle samples investigated, POPC/DMPE-DTPA·Dy, POPC/DMPE-DTPA (no lanthanide), and POPC/DMPC (no chelator lipid). Again, the vesicles are rather uniform in size, mostly unilamellar, and some vesicles appear edged. Fig. 5.13 shows micrographs of vesicles prepared with a chelator bound to a phospholipid with one unsaturated acyl chain (POPE-DTPA instead of DMPE-DTPA). Some vesicles are elongated, and again most vesicles are unilamellar. It is difficult to find vesicles with clear edges.
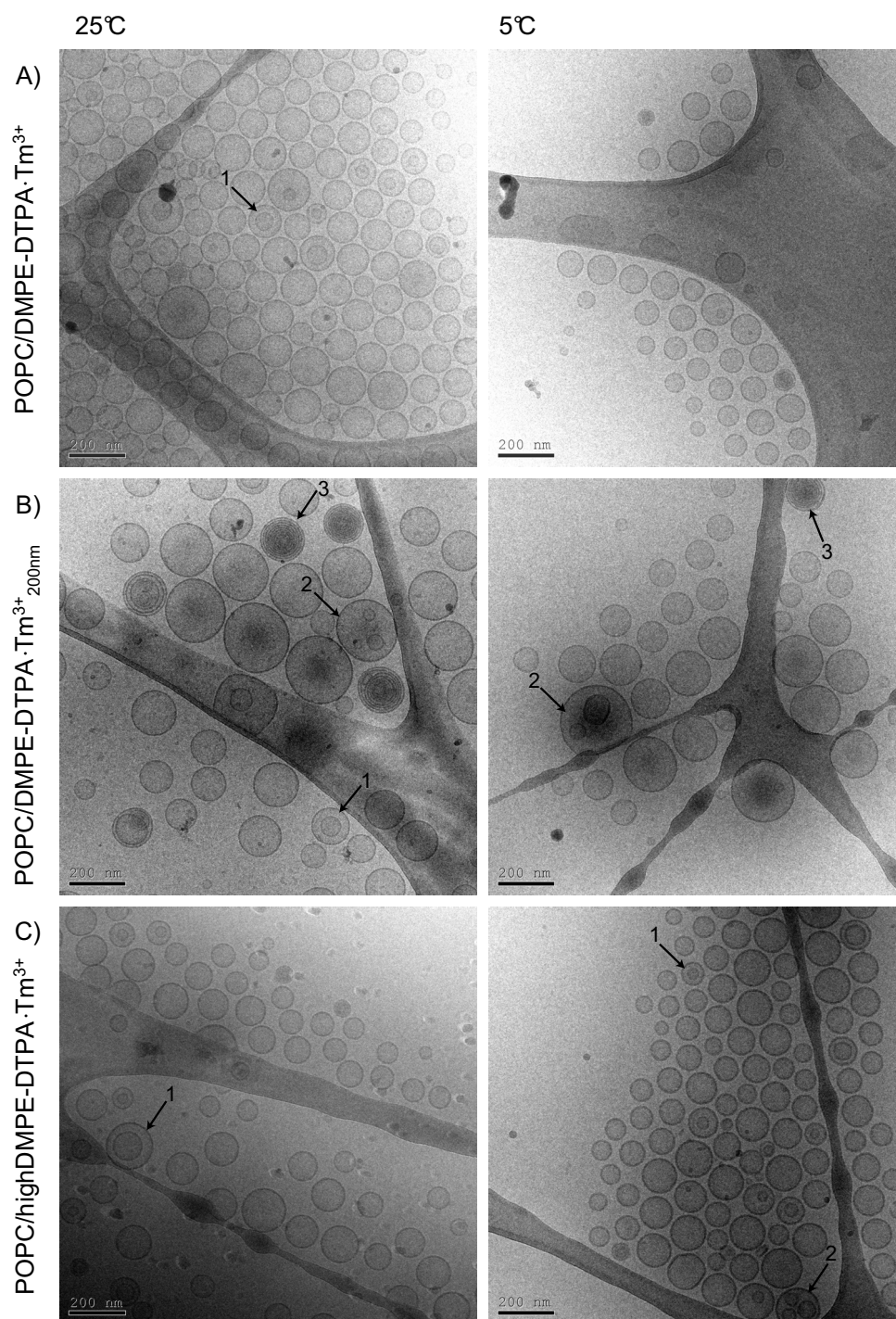
Figure 5.10: Cryo-TEM micrographs of samples shock frozen from room temperature (left column) and from 5 °C samples (right column) of vesicles consisting of POPC/DMPE-DTPA complexed with Tm^{3+}. The molar ratio of POPC:DMPE-DTPA is 4:1 in rows A-B and 4:2 in row C. Sample in B was extruded through a polycarbonate membrane with a pore size of 200 nm, samples in A and C were in addition extruded through a membrane with a pore size of 100 nm. Arrows 1 indicate oligolamellar, arrows 2 multivesicular and arrows 3 multilamellar vesicles.

63
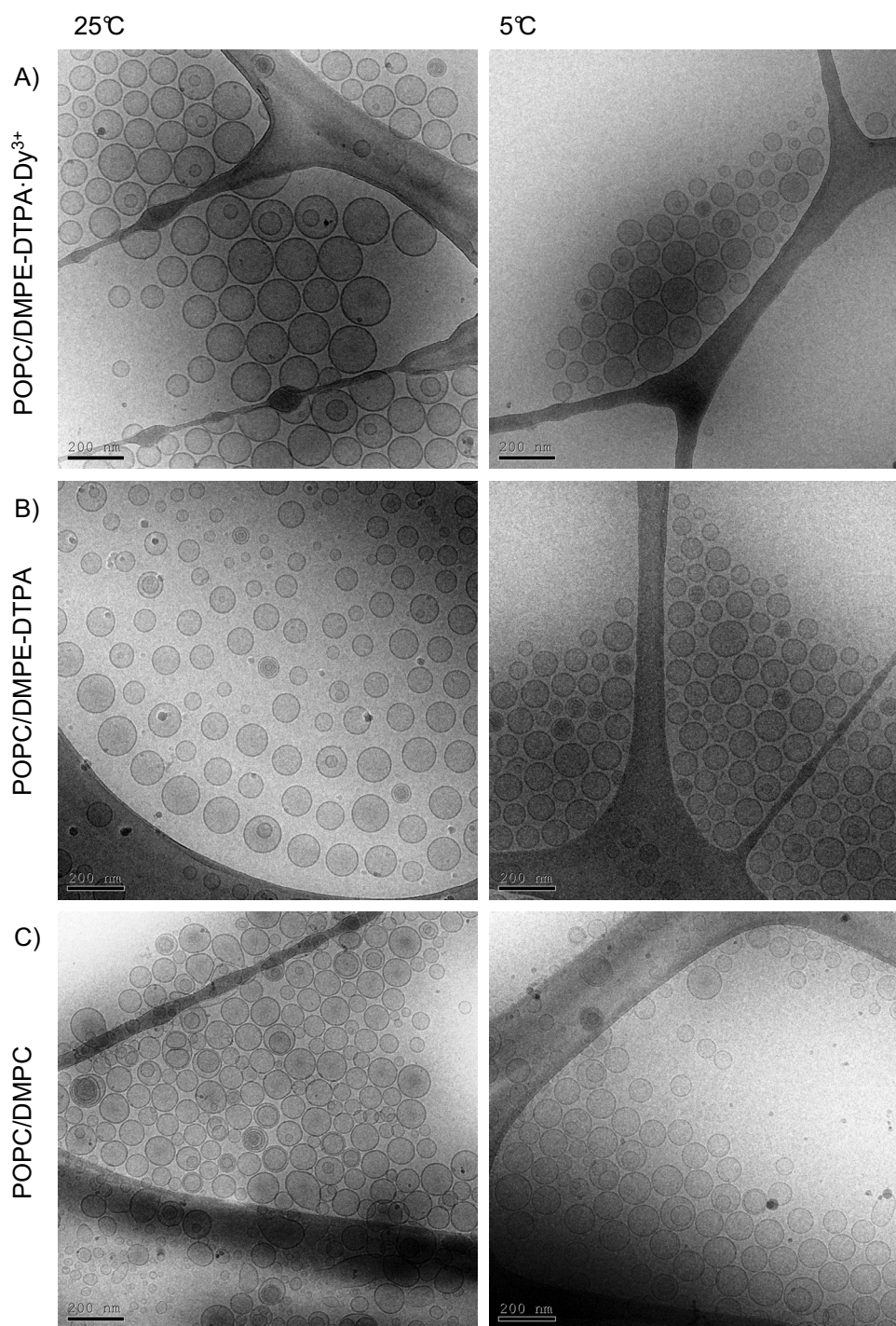
Figure 5.11: Cryo-TEM micrographs of samples shock frozen from room temperature (left column) and 5 °C samples (right column). Vesicles consisting of POPC/DMPE-DTPA complexed with Dy^{3+} (A) and without complexed lanthanides (B) are shown. Vesicles in row C are composed of POPC and DMPC. The molar ratio of the lipids was 4:1 in all three samples.
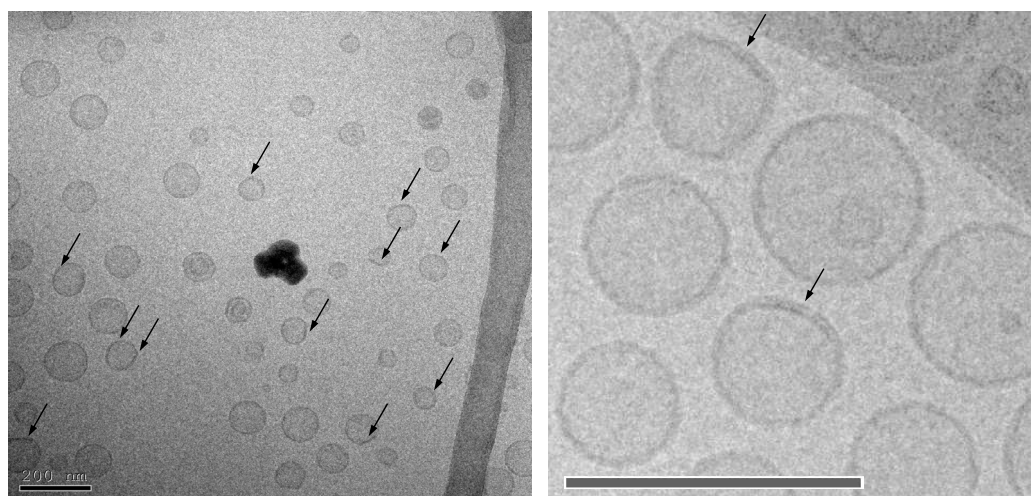
Figure 5.12: Cryo-TEM micrographs of vesicles consisting of POPC/DMPE-DTPA·Tm in a molar ratio of 4:1:1 taken from samples frozen from 5 °C. Arrows point to edges in the membrane of the vesicles. Right: Zoom of 5 °C micrograph in Fig. 5.10 A
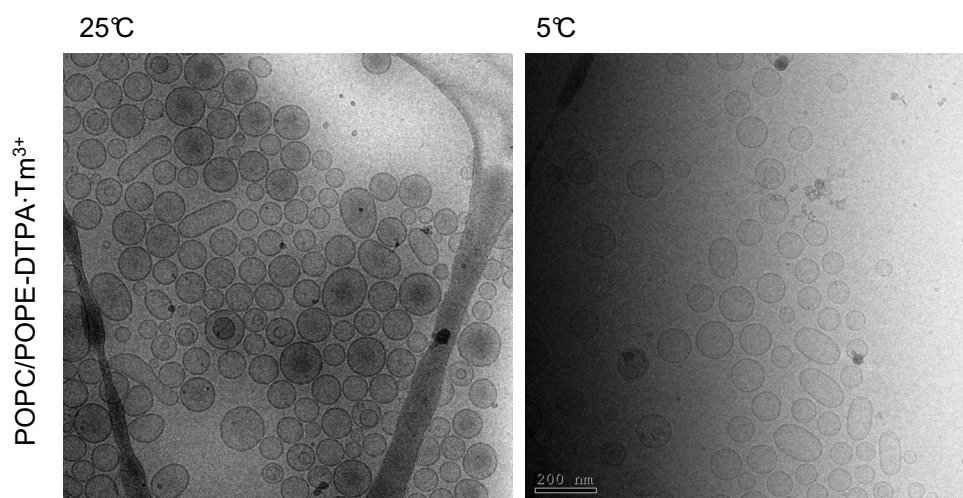
Figure 5.13: Cryo-TEM micrographs of POPC/POPE-DTPA·Tm taken from samples at room temperature (left) and at 5 °C (right).

5.3.3 ^{31}P NMR Measurements

^{31}P NMR measurements were carried out with POPC/DMPE-DTPA·La and POPC/DMPC. Lanthanum instead of thulium or dysprosium was used to prevent line shift and broadening of the NMR spectrum. Fig. 5.14 left shows the ^{31}P NMR spectra of POPC/DMPE-DTPA·La at 2.5, 25 and 30 °C. At low temperatures the spectra is a powder pattern (Fig. 5.14 C). If temperature is raised the isotropic peak becomes increasingly pronounced (Fig. 5.14 A-B). For the sample with pure phospholipids (POPC/DMPC) ^{31}P NMR spectra were taken at 2.5 and 30 °C (Fig. 5.14 right). The powder pattern is again dominant at low temperatures (Fig. 5.14 E), at 30 °C (Fig. 5.14 D) the isotropic peak is more pronounced.
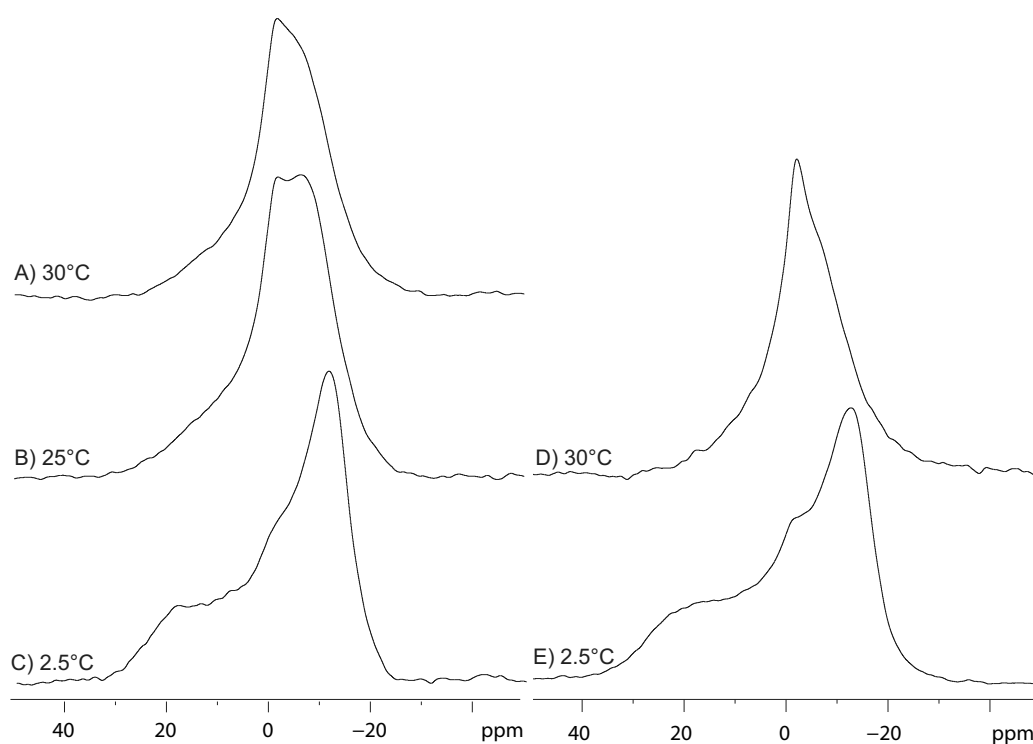
Figure 5.14: Left: ^{31}P NMR-spectra of POPC/DMPE-DTPA·La at 30 °C (A), 25 °C (B) and 2.5 °C (C). Right: ^{31}P NMR-spectra of POPC/DMPC at 30 °C (D) and 2.5 °C (E). Powder pattern dominates the spectrum at low temperature whereas at higher temperature the isotropic peak is more pronounced.

5.3.4 DSC

DSC curves were recorded for samples containing vesicles of POPC and for vesicles of a mixture of 80% POPC and 20% DMPE-DTPA·Tm. The POPC concentration was the same in both samples. Fig. 5.15 shows the two curves, separated for better distinction. Dark gray is POPC/DMPE-DTPA·Tm, light gray POPC. In the case of POPC a sharp endothermic peak is visible, whereas for POPC/DMPE-DTPA·Tm no clear peak is visible.
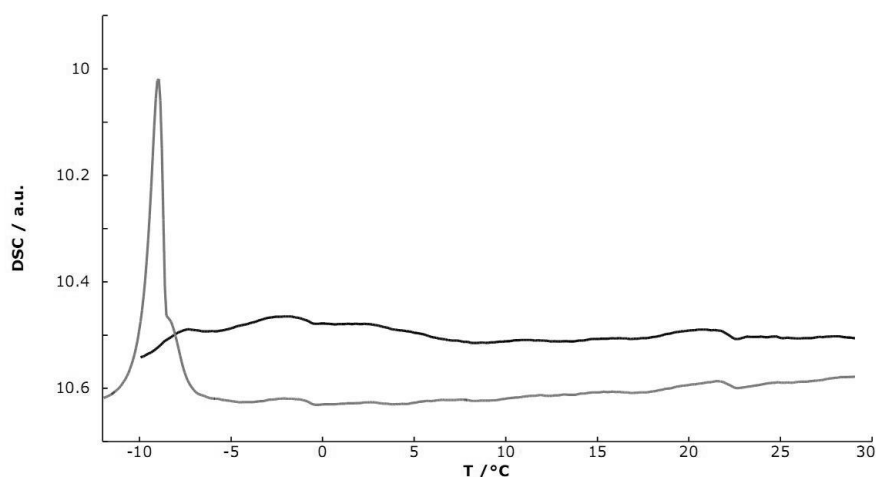
Figure 5.15: Differential scanning calorimetry curves from vesicles of POPC (gray curve) and POPC/DMPE-DTPA·Tm (black curve). The curves are separated for better distinction. Note that in a mixture of POPC with 20% DMPE-DTPA·Tm, neither POPC nor DMPE-DTPA·Tm exhibits a sharp peak. The total concentration of POPC was the same in both samples.

5.3.5 Vesicle Size Analysis from SANS and Cryo-TEM Data, Compared to DLS Measurements

The average size of the vesicles expressed by the hydrodynamic diameter was determined by dynamic light scattering (DLS) at room temperature and compared to the size determined by analyzing cryo-TEM micrographs and SANS data. Tab. 5.2 shows the DLS results for all the samples investigated. The vesicle sizes correspond qualitatively to the observed vesicle sizes in the cryo-TEM micrographs. The size of the standard sample, POPC/DMPE-DTPA·Tm was analyzed in more detail.

Table 5.2: Hydrodynamic diameter (D_H) obtained with DLS at room temperature of the vesicle samples used in SANS and cryo-TEM measurements.

Vesicle Formulation	D_H [nm]
POPC/DMPE-DTPA·Tm	108.6
POPC/DMPE-DTPA·Tm$_{200nm}$	146.2
POPC/DMPE-DTPA·Dy	111.8
POPC/highDMPE-DTPA·Tm	107.4
POPC/DMPE-DTPA	101.4
POPC/POPE-DTPA·Tm	96.6
POPC/DMPC	73.4

A detailed analysis of cryo-TEM micrographs of the POPC/DMPE-DTPA·Tm sample frozen from room temperature and from 5 °C was made. It yielded a diameter of 88.6 nm ± 24.2 nm at room temperature and a size of 82.6 nm ± 19.6 nm at 5 °C. The corresponding probability density function (q_0) and the cumulative size distribution function (Q_0) are plotted in Fig. 5.16, together with the size distribution gathered from DLS measurements. The size distribution from DLS-measurements has an average of 108.6 nm, which is slightly higher than the averages obtained from cryo-TEM micrographs. This can be explained by the underestimation of small vesicles by DLS, which was described by Egelhaaf *et al.* (1996). Cryo-TEM micrographs allow the precise determination of individual vesicles sizes, but do not average over the whole sample volume as DLS.

The SANS curves were interpreted using Guinier analysis. Guinier analysis of low q range scattering data provides the radius of gyration, R_G, following Eq. 5.1. As a vesicle represents a thin spherical shell, the radius of gyration is equivalent to the vesicle radius. In the high q range, Guinier analysis can be used to determine the thickness of the vesicle membrane. For this, the radius of gyration is first determined using Eq. 5.3, where c is a constant. As a vesicle membrane represents a local planar structure in this q range, the thickness of the membrane t is $\sqrt{12}\,R_G$ (Hjelm *et al.*, 2000). According to Eq. 5.2 a plot of the logarithm of the scattering intensity $lnI(q)$ against the square of the scattering vector q^2 gives a linear regime at small q values with the slope $-R_G^2/3$.
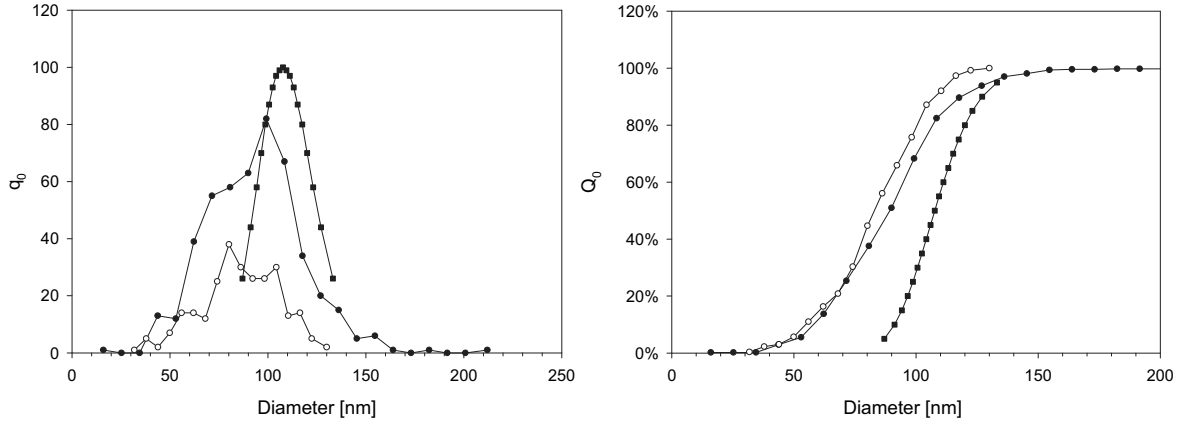
Figure 5.16: Probability density function q_0 (left) and size distribution function Q_0 (right) of vesicles consisting of POPC/DMPE-DTPA·Tm gathered from cryo-TEM micrographs analysis (circles) and from DLS measurements (squares). Temperatures are 22 °C (closed symbols) and 5 °C (open symbols).

$$I\left(q\right) = I_0 \exp\left(-\frac{1}{3}q^2 R_G^2\right) \tag{5.1}$$

$$\ln I\left(q\right) = \ln I_0 - \frac{1}{3}q^2 R_G^2 \tag{5.2}$$

$$I\left(q\right) = \frac{c}{q^2} \exp\left(-R_G^2 q^2\right) \tag{5.3}$$

Fig. 5.17 shows the Guinier approximation at the example of POPC/DMPE-DTPA·Tm at 30 °C and 0 T, yielding a diameter of 96.8 nm. The radius of gyration of POPC/DMPE-DTPA·Tm obtained from Guinier fit of the SANS curve at 22 °C is 48.3 nm, which corresponds to the vesicle size obtained with cryo-TEM and DLS (Tab. 5.3).

In Fig. 5.18 the vesicle diameters obtained from Guinier fits for different temperatures are plotted of vesicles consisting of POPC/DMPE-DTPA·Tm at 0 and 8 T and of POPC/DMPC at 8 T. For POPC/DMPE-DTPA·Tm at 0 T (Fig. 5.18, black open circles) the diameter is around 96.6 nm at 30, 22 and 17.5 °C, but decreases to 85.6 nm when temperature is lowered to 2.5 °C. The same sample at 8 T (Fig. 5.18, black closed circles) shows the same temperature dependence, with a slight deviation in the measured sizes. For POPC/DMPC at 8 T (Fig. 5.18, gray closed circles) the changes in vesicle size are less pronounced with a slight increase at lower temperatures. The observed temperature dependence was reversible.
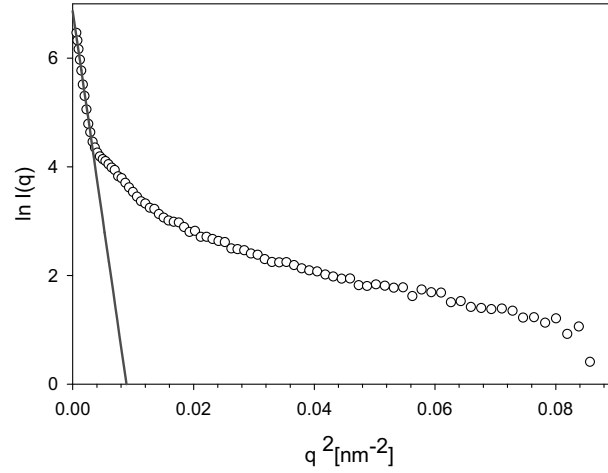
Figure 5.17: Radial averaged SANS curves of POPC/DMPE-DTPA·Tm at 30 °C and 0 T (open circles) and corresponding Guinier fit in the linear regime (solid line). The linear equation of the Guinier fit is $y = 6.8646 - 772.1882x$.
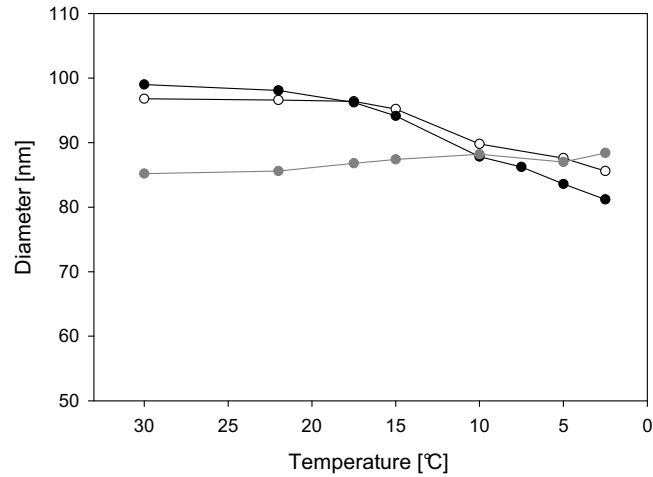
Figure 5.18: Vesicle diameter at different temperatures of POPC/DMPC (gray) and POPC/DMPE-DTPA·Tm (black) at 0 T (open symbols) and 8 T (closed symbols). The diameter of POPC/DMPE-DTPA·Tm vesicles decreases reversibly with decreasing temperature, while the diameter of POPC/DMPC vesicles stays more or less constant over the whole measured temperature range. The diameters were obtained from Guinier fits of SANS data.

In Tab. 5.3 an overview of all the vesicle diameter of the standard sample POPC/DMPE-DTPA·Tm obtained with the different measurement methods is given.

Table 5.3: Vesicle diameter of POPC/DMPE-DTPA·Tm [*nm*] obtained with cryo-TEM, SANS and DLS at different temperatures

Temperature [℃]	Cryo-TEM (0 T)	SANS (0 T)	SANS (8 T)	DLS (0T)
30		96.8	99.0	
22	88.6	96.6	98.2	108.3
17.5		96.4	96.2	
15		95.2	94.2	
10		89.8	88.0	
7.5			86.2	
5	82.6	87.6	83.6	
2.5		85.6	81.2	

Guinier fits were also made of the sectoral averaged scattering patterns at 8 T and 2.5 ℃, indicating a different vesicle diameter in magnetic field direction than perpendicular to it for POPC/DMPE-DTPA·Tm, POPC/DMPE-DTPA·Dy, and POPC/highDMPE-DTPA·Tm (Fig. 5.19).
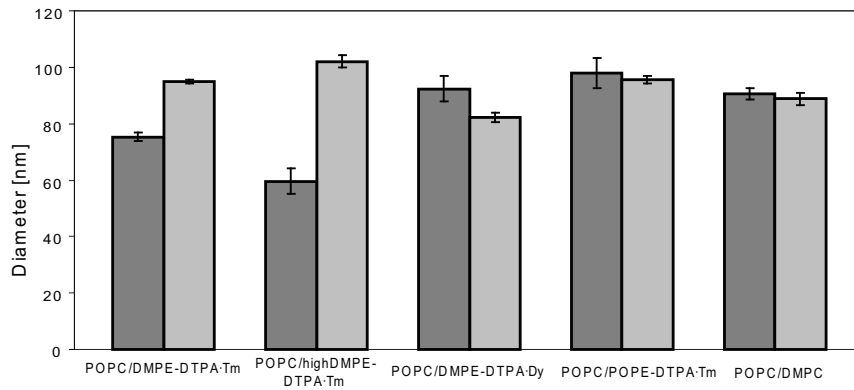
Figure 5.19: Diameters of vesicles under a magnetic field of 8 T at 2.5 ℃, derived from sectoral averaged SANS data. Diameters were obtained with Guinier analysis. Dark gray: Diameters in direction of magnetic field. Light gray: Vesicle diameters in perpendicular direction to magnetic field. Error bars indicate the fit uncertainty.
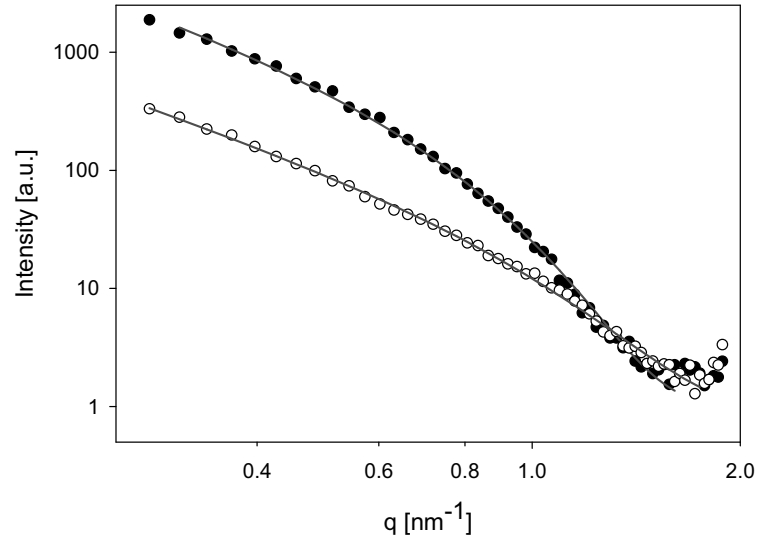
Figure 5.20: Sectoral averaged SANS curves at high q values of POPC/DMPE-DTPA·Tm at 8 T and 2.5 °C where the membrane thickness can be determined. Closed circles are in direction of magnetic field, open circles perpendicular to the field and solid lines show corresponding Guinier fits.

Guinier fits of high q scattering data, measured at detector distance of 2 m, were made to determine the membrane thickness in direction of the magnetic field and perpendicular to the field for the POPC/DMPE-DTPA·Tm sample at 2.5 °C and 8 T (Fig. 5.20). The determined membrane thickness in field direction was 4.97 nm and perpendicular to the field 3.45 nm.

5.3.6 Permeability Measurements

Table 5.4: Overview of the permeability measurements made with samples containing 50 mM of quenched calcein. Sample formulation was the same as for SANS measurements, except for POPC/DMPE-DTPA·Tm+Dy, where a 1:1 mixture of Tm^{3+} and Dy^{3+} was complexed to DMPE-DTPA. Each experiment was carried out without magnetic field as well, and the permeabilities compared. No magnetic field effect was found at any condition tested.

Vesicle Formulation	MF [T]	Temperature profile
POPC/DMPE-DTPA·Tm	5.6	12 h at 22 °C
	5.6	30 °C to 5.5 °C in 4 h, back to 22 °C in 15 min
	5.6	12 h at 17 °C
	5.6	30 °C to 17 °C back to 30 °C, 8 cycles in 5 h
	5.6	30 °C to 5.5 °C in 4 h back to 30 °C in 30 min, 4 cycles
POPC/DMPE-DTPA·Dy	5.6	12 h at 22 °C
POPC/DMPE-DTPA·Tm$_{200nm}$	5.6	12 h at 22 °C
POPC/DMPE-DTPA·Tm 25 mM	5.6	12 h at 22 °C
POPC/DMPE-DTPA	5.6	12 h at 22 °C
POPC/DMPE-DTPA·Tm+Dy	5.6	12 h at 22 °C
	5.6	12 h at 18 °C
	5.6	12 h at 25 °C
	5.6	12 h at 12 °C
	5.6	30 °C to 5.5 °C in 4 h, back to 22 °C in 15 min
	16.4	2 h at 18 °C
	16.4	2 h at 25 °C

Permeability measurements were made with a series of vesicles containing a water soluble fluorescence marker, calcein, which shows low fluorescence at high concentrations (fluorescence is quenched), and becomes fluorescent once it passes the membrane and gets diluted. By measuring the fluorescence before and after an experiment, information was obtained about a possible leakage which may have occurred. The leakage

of a sample exposed to a magnetic field was compared to the leakage of a sample which experienced the same temperature profile without magnetic field. In none of the experiments carried out a significant magnetic field effect on the permeability was observed. In Tab. 5.4 the conditions of the permeability measurements are listed.

5.4 Discussion

The magnetic field dependent anisotropy of the SANS scattering pattern clearly indicates a magnetic field effect on some of the investigated vesicle formulations. As mentioned in the introduction, the following possible magnetic field effects were considered: aggregation/fusion, budding/fission, deformation, alteration of permeability and lateral segregation. No evidence for vesicle aggregation/fusion, budding/fission, or change in permeability was found, as will be discussed below. However, the fact that an anisotropic SANS scattering pattern was obtained is a clear indication that a magnetic field induced orientation occurred. For this either the vesicle shape has to be distorted or the membrane composition has to become inhomogeneous.

A model is now proposed, which is in agreement with all experimental data: Temperature induced lipid demixing and domain formation, followed by magnetic field induced domain orientation. This model is called the oriented domain model. For our basic sample, POPC/DMPE-DTPA·Tm, a lowering of the temperature below a critical temperature of 25 °C, which is close to the phase transition temperature T_M of DMPC (Koynova and Caffrey, 1998), leads to a demixing of the two phospholipids and the formation of DMPE-DTPA·Tm rich domains. These DMPE-DTPA·Tm rich domains grow as the temperature is lowered, leading to clusters of DMPE-DTPA·Tm which have a sufficiently high magnetic susceptibility anisotropy to become oriented in a strong magnetic field. The domains align with the domain normal parallel to the magnetic field. Fig. 5.21 depicts the oriented domain model of a basically spherical vesicle containing two flat domains. The domains are assumed to consist of a DMPE-DTPA rich bilayer in the rigid crystalline-analogue state, embedded in the POPC bilayer in the fluid-analogue state. The two domains occupy an area of 20% of the total vesicle surface, in approximation of the 4:1 molar ratio of POPC:DMPE-DTPA used. Tm^{3+}, which confers a large magnetic moment to the membrane, is concentrated in the domain, making orientation with the domain normal parallel to the magnetic field possible.

The fact that an identical scattering pattern of the vesicles at 8 T and 2.5 °C (Fig. 5.3H) is obtained whether the magnetic field is turned on before or after cooling the sample, may indicate that the temperature decrease is responsible for a structural anisotropy, which can then be oriented by magnetic fields. As mentioned above, it is proposed that this structural anisotropy is caused by lateral segregation of the two lipids in the system, providing a temperature dependent miscibility of DMPE-DTPA in POPC. Temperature induced lateral segregation or demixing of multicomponent phospholipid membranes is well documented. Most literature describes ternary mixtures of two phospholipids with different phase transition temperatures and cholesterol (Anghel *et al.*, 2007; Baumgart *et al.*, 2003; Imai, 2007; Korlach *et al.*, 1999; Masui

75
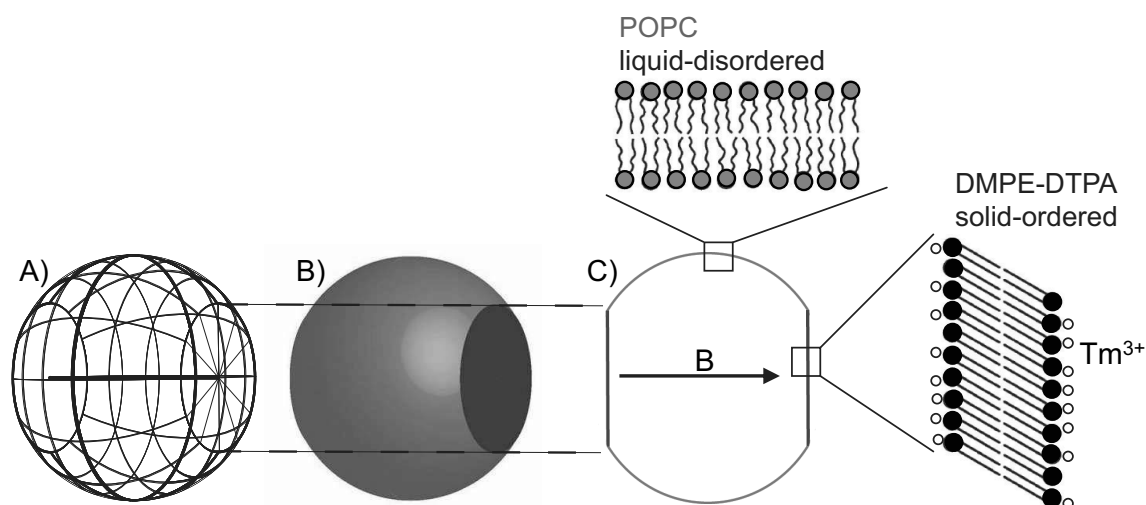
Figure 5.21: Sketch illustrating the magnetic field alignable domain model. A, B and C show three drawings of a vesicle with two flat domains. DMPE-DTPA·Tm is assumed to form solid domains (black in B and C) in a solid-ordered state, surrounded by POPC (gray in B and C) in the liquid-disordered state.

et al., 2006; Pencer et al., 2005a, 2007; Veatch and Keller, 2002; Yanagisawa et al., 2007). Three distinct phase morphologies for giant unilamellar vesicles have been detected by fluorescence microscopy (Veatch and Keller, 2002). Below a certain miscibility temperature a phase separation of the two phospholipids occurs. If cholesterol is present two coexisting liquid phases are formed. Without cholesterol the higher melting lipid forms a solid domain in a liquid phase. Such solid domains assume the form of flat plates (Lipowsky and Dimova, 2003). Lipid domains have also been found on small unilamellar vesicles by SANS using contrast matching technique with chaindeuterated phospholipids (Anghel et al., 2007; Imai, 2007; Masui et al., 2006; Pencer et al., 2005a, 2007). Hartmann et al. (1977) have shown direct visualization of lipid domains on giant vesicles by freeze-etch electron microscopy. Close observation of our cryo-TEM micrographs made evident that the vesicles are not perfectly spherical, but often show edges in the membrane (Fig. 5.12). In comparison, these edges seem to appear more frequently in 5 °C than in 22 °C micrographs (Fig. 5.10, 5.11). The only exception was POPC/POPE-DTPA·Tm, where no clear edges could be identified (Fig. 5.13). It is appears probable that demixing does not take place because only one type of fatty acid is present in this sample.

A strong indicator for lateral segregation is the difference in membrane thickness horizontal and perpendicular to the magnetic field direction at 8 T and 2.5 °C, as found by Guinier analysis of SANS data of the POPC/DMPE-DTPA·Tm sample

(Fig. 5.20). A membrane thickness of 3.45 nm parallel to the magnetic field , and of 4.97 nm perpendicular to the field was found. The bilayer thickness of POPC has been measured to be 3.82 nm (Kucerka *et al.*, 2006), which corresponds to the thickness measured for the vesicle membrane part oriented parallel to the magnetic field. The bilayer thickness of DMPC at 10 °C has been measured to be 4.43 nm by Pencer *et al.* (2005b) and the radius of DTPA complexed with the lanthanide gadolinium to be 2.95 Å (Bammer *et al.*, 2004). Without knowing the exact configuration of the DMPE-DTPA·Tm head group, it can still be expected that DMPE-DTPA in the solid ordered state forms a significantly thicker bilayer than POPC the liquid disordered state, corresponding with the determined thickness differences parallel and perpendicular to the magnetic field.

According to our model, the anisotropy of the SANS pattern has two origins. Firstly, the scattering length density of DMPE-DTPA·Tm is different from the one of POPC. The scattering length density of DMPE-DTPA·Tm in solid ordered state was estimated to be 1.10×10^{10} cm^{-2} (Bammer *et al.*, 2004; Knoll *et al.*, 1981; Nagle and Tristram-Nagle, 2000; Tristram-Nagle *et al.*, 2002) and of POPC in the liquid disordered state to be 2.51×10^9 cm^{-2} (Pencer *et al.*, 2008; Vacklin *et al.*, 2005). Therefore, demixing of the lipids yields anisotropic scattering. Secondly, the average vesicle diameter seen by SANS in horizontal direction is smaller than in vertical direction, due to the flattened curvature of the domains, increasing the anisotropy of the neutron scattering. Size information of the vesicles in the magnetic field was gathered by Guinier approximation of the SANS data. Fig. 5.18 shows that the Guinier size of the vesicles follows the same temperature dependence with and without magnetic field, with a maximal difference of 5 % at 2.5 °C. Guinier fits of sectoral averaged SANS curves of samples with an anisotropic scattering pattern clearly show a different vesicle diameter in direction of the magnetic field compared to the vesicle diameter perpendicular to the magnetic field (Fig. 5.19). This is a clear indication that the samples are not perfectly spherical at low temperatures.

Some theoretical considerations can be made to compare the obtained Guinier vesicle diameters perpendicular and parallel to the magnetic field with the expected diameter reduction due to rigid domains, which represent flat membrane segments. Fig. 5.22 shows a sketch of a vesicle with one flat domain. For the vesicles consisting of POPC/DMPE-DTPA·Tm and POPC/DMPE-DTPA·Dy we assumed that the area of the domain, A_{Domain}, accounts for 20 % of the total vesicle surface, $A_{Vesicle}$, and 40 % for POPC/highDMPE-DTPA·Tm, according to the amount of chelator-lipid (DMPE-DTPA) in the samples. Using Eq. 5.4 - 5.6, and assuming a vesicle radius r_v of 50 nm, the short vesicle radius in direction of the domain r_s can be calculated.

$$A_{vesicle} = 4\pi r_v^2 \tag{5.4}$$

$$A_{domain} = \pi r_d^2 \tag{5.5}$$

$$r_v^2 = r_d^2 + r_s^2 \tag{5.6}$$

According to the magnetic field alignable domain model (Fig. 5.21), the domains doped with Tm^{3+} orient with their normal parallel to the magnetic field, resulting in a reduced diameter in this direction ($d_\parallel = r_s + r_v$ assuming one domain, $d_\parallel = 2\,r_s$ assuming two domains). In contrast, for domains doped with Dy^{3+}, the short diameter would be perpendicular to the magnetic field as shown in Tab. 5.5.

Table 5.5: Comparison of Guinier vesicle diameters parallel $d_\parallel$ and perpendicular $d_\perp$ to the magnetic field with expected diameters assuming one or two flat domains, which are oriented in the magnetic field. For POPC/highDMPE-DTPA·Tm, the assumption of one flat domain leads to a domain radius r_d of 63.2 nm, which is larger than the vesicle radius, making this assumption less probable. Guinier diameter were obtained by fitting sectoral averaged SANS data at 2.5 °C and 8 T perpendicular and parallel to the magnetic field.

	POPC/DMPE-DTPA·Tm vesicle diameter [nm]		POPC/highDMPE-DTPA·Tm vesicle diameter [nm]		POPC/DMPE-DTPA·Dy vesicle diameter [nm]	
	$d_\perp$	$d_\parallel$	$d_\perp$	$d_\parallel$	$d_\perp$	$d_\parallel$
assuming 1 domain	100	72.4	-	-	72.4	100
assuming 2 domains	100	77.4	100	44.8	77.4	100
Guinier diameter	95.1	75.3	102.1	59.6	82.2	92.4

For vesicles consisting of POPC/DMPE-DTPA·Tm the theoretically assumed reduction of the diameter parallel to the magnetic field is in good agreement with the obtained Guinier diameter. For POPC/highDMPE-DTPA·Tm the theoretical short vesicle radius assuming two flat domains (44.8 nm) is smaller than the obtained Guinier diameter (59.6 nm). This could indicate that more than two domains are formed with increasing amount of DMPE-DTPA·Tm.

For POPC/DMPE-DTPA·Dy, the Guinier-fit diameters were 92.4 and 82.2 nm, in this case the smaller diameter was measured perpendicular to the magnetic field.
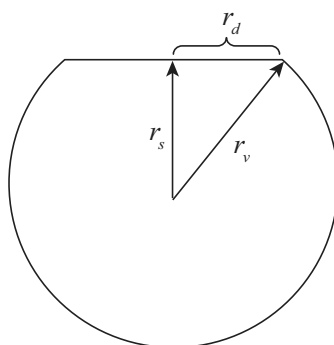
Figure 5.22: Sketch of a vesicle with one flat domain, r_v is the vesicle radius, r_d the domain radius and r_s the short vesicle radius in direction of the domain.

Comparison of Fig. 5.8A to Fig. 5.3H shows that the scattering pattern of DMPE-DTPA·Dy is not identical to the scattering pattern of DMPE-DTPA·Tm rotated by 90°, as the anisotropy is less pronounced. According to our model, the POPC/DMPE-DTPA·Dy sample undergoes the same temperature driven domain formation, with the domain normal oriented perpendicular to the magnetic field. This explains the 90° shift in the anisotropy of the scattering pattern. Domains oriented with their normal perpendicular to the magnetic field have an additional degree of freedom, as they can rotate around an axis parallel to the magnetic field. This could explain the less pronounced scattering anisotropy of POPC/DMPE-DTPA·Dy compared to POPC/DMPE-DTPA·Tm. The POPC/highDMPE-DTPA·Tm sample shows a much more pronounced anisotropy, indicating larger and more pronounced domain formation (Fig. 5.6). Domain formation may also occur for POPC/DMPC, and POPC/DMPE-DTPA, as edges in the cryo-TEM micrographs indicate (Fig. 5.11 B and C), but they can not be oriented without lanthanides (see isotropic scattering pattern for POPC/DMPC in Fig. 5.9). In POPC/POPE-DTPA·Tm, no evidence of domain formation is found (SANS: Fig. 5.7, cryo-TEM: Fig. 5.13). This could be due to the fact that the temperatures investigated are above the phase transition temperatures of both lipids, which is below 0 ℃. A sample consisting of DMPC/DMPE-DTPA·Tm, where the phase transition temperature is around room temperature, has been shown to form flat disks and is discussed in chapter 6.

NMR was used to confirm that the sample morphology is purely vesicular at the temperatures where anisotropic SANS patterns were obtained, and that no structures were formed which had evaded the cryo-TEM analysis. ^{31}P NMR spectra of POPC/DMPE-DTPA·Tm and POPC/DMPE-DTPA·Dy were difficult to interpret because of line shift and broadening (data not shown). Instead, spectra recorded of POPC/DMPE-DTPA·La are shown, where the diamagnetic La^{3+} was complexed to the chelator instead of Tm^{3+} or Dy^{3+}. This sample lost its magnetic orientabil-

ity, and gave spectra similar to those of POPC/DMPC. ^{31}P NMR measurements of POPC/DMPE-DTPA·La were made at 2.5 °C, 25 °C and 30 °C and of POPC/DMPC at 2.5 °C and 30 °C (Fig. 5.14). For both samples a powder pattern with very small isotropic contribution at 0 ppm was obtained at 2.5 °C, which is in agreement with the purely vesicular structure found with cryo-TEM. At 25 °C and 30 °C the isotropic peak becomes more dominant, representing faster lipid motion. For POPC/DMPE-DTPA·La NMR spectra were recorded in the following order: 25 °C, 2.5 °C, 25 °C, 30 °C, 25 °C. The three spectra at 25 °C were identical, indicating that no irreversible structure changes happened during heating or cooling of the sample, confirming the reversibility of the SANS measurements.

As mentioned above, the following potential magnetic field effects have not been observed: aggregation/fusion, budding/fission and alteration of permeability. Fusion, fission or aggregation would lead to a change in size distribution. The size distribution was monitored with DLS, SANS and cryo-TEM. SANS and cryo-TEM results indicate a slight decrease in vesicle size when temperature is lowered (cryo-TEM Fig. 5.16, SANS Fig. 5.18), contradicting fusion and aggregation. Significant aggregation, fusion or fission of vesicles would have lead to a more drastic size change and were not observed in the cryo-TEM pictures. DLS measurements before and after SANS measurements show that no irreversible change in size distribution had occurred (Tab. 5.2 lists results before SANS measurements). It appears improbable that fusion, fission or aggregation would be totally reversible. Furthermore, fusion and fission could not have explained the structural anisotropy required for magnetic orientation.

Budding vesicles would also represent an anisotropic structure. Even though no proof against magnetic field induced budding for our samples can be given, no result was found supporting it. While temperature induced budding has been observed for giant vesicles (Baumgart *et al.*, 2003), budding is not likely to happen for small unilamellar vesicles with the highly curved membrane due to energetical reasons (Lipowsky and Dimova, 2003). Additionally, no hint for budding of vesicles without magnetic field can be found in cryo-TEM micrographs (Fig. 5.10, 5.11, 5.13).

The anisotropy required for magnetic orientation could have been explained by vesicle aggregates with a non spherical over all shape, but has not been observed, as mentioned above. Another possible explanation for the anisotropy could have been the deformation of vesicles from spherical to ellipsoidal shape. Comparison of cryo-TEM micrographs at 5 °C and at room temperature show no temperature induced ellipsoidal deformation of any sample investigated, contradicting a possible magnetic field orientation after ellipsoidal deformation caused by low temperatures (Fig. 5.10, 5.11). Some ellipsoidal vesicles consisting of POPC/POPE-DTPA·Tm were found at both temperatures (Fig. 5.13), however no significant anisotropy in scattering pattern was found for this sample (Fig. 5.7). Fitting of SANS data with a ellipsoidal shell

form factor could not satisfyingly describe the SANS curves.

Leakage measurements of calcein through the vesicle membrane showed no effect of the magnetic field on membrane permeability. Lowering the temperature below room temperature increased the permeability of all the samples tested. Leakage occurs preferentially at packing defects in the bilayer structure (Ono *et al.*, 2002). Such defects are found at the edges of domains. The fact that the magnetic field has no influence on the permeability of the vesicles indicates that the domain formation itself is not influenced by the magnetic field, but by temperature. The domains could then reposition themselves in the POPC membrane to achieve a lowest energy state, with an orientation in the magnetic field depending on the lanthanide used.

A mathematical form factor for oriented flat domains in spherical vesicles is under preparation and will be used to fit the SANS data in order to test the oriented domain model.

5.5 Conclusion

The results presented in this chapter show that vesicles consisting of mixtures of POPC and DMPE-DTPA complexed with paramagnetic lanthanides (Tm^{3+}, Dy^{3+}) react to magnetic fields at low temperatures. This reactivity originates from a temperature dependent demixing of the two lipids, leading to solid domains of DMPE-DTPA·Lanthanide surrounded by POPC in fluid-analogue state. The domains have the shape of flat disks and assemble the large magnetic moments conferred by the lanthanides. The whole domain thus becomes orientable in the magnetic field. The direction of alignment can be selected by the type of lanthanide used. The domains orient with their normal perpendicular to the field with dysprosium, and parallel to the field with thulium.

6 Bicelles

6.1 Introduction

Bilayered micelles, or "bicelles" are an important system for the study of membrane proteins with high resolution NMR. The term "bicelle" is used in this work to denote a small disk like aggregate, usually formed by a mixture of a long chain phospholipid and a detergent or short chain phospholipid (Katsaras *et al.*, 2005). The most common bicelle formulation is DMPC/DHPC, where DMPC (1,2-dimyristoyl-*sn*-glycero-3-phosphocholine) forms the flat part of the disk and DHPC (1,2-dihexanoyl-*sn*-glycero-3-phosphocholine) covers the edge (Katsaras *et al.*, 2005). In addition to these bilayered disks, mixtures of DMPC and DHPC can form other morphologies, depending on temperature, molar ratio of DMPC:DHPC and lipid concentration (Harroun *et al.*, 2005; Katsaras *et al.*, 2005; Nieh *et al.*, 2001, 2002; Triba *et al.*, 2005, 2006; van Dam *et al.*, 2004, 2006). The origin of the different morphologies lies primarily in the temperature and concentration dependence of the miscibility of the two lipids (Triba *et al.*, 2005). As the temperature is raised, DHPC becomes increasingly soluble in DMPC, in consequence, less DHPC is available to cover the edges of the bicelles. As a result much larger structures are formed, such as chiral nematic ribbons or perforated lamellar sheets (Katsaras *et al.*, 2005; Soong and Macdonald, 2008).

These types of structures are suitable to be aligned in magnetic fields. The force causing the alignment of the system is the anisotropy of the diamagnetic susceptibility of the phospholipids, resulting in a preferred orientation with the long molecular axis perpendicular to the magnetic field (Qiu *et al.*, 1993). The orientation of a single molecule is opposed by the thermal fluctuation kT. In a bilayer, where the molecules are mostly aggregated parallel to each other, the magnetic anisotropy becomes additive and macroscopic orientation of the aggregates in magnetic fields is feasible (Qiu *et al.*, 1993).

The magnetic orientability can be influenced by doping the membrane with paramagnetic lanthanides possessing a large magnetic moment (Binnemans and Gorller-Walrand, 2002; Nieh *et al.*, 2002; Prosser *et al.*, 1998b). As such, the lanthanides

are often anchored to the membrane by a complexing agent (DTPA, diethylenetri-aminepentaacetate) which is covalently bound to a phospholipid head group (DMPE-DTPA).

While DMPC/DHPC is the most widely studied system, related bicellar formulations have been investigated as well. It has been shown that bicelle formation is still observed if the chain length of the two saturated lipids is varied to some extend (De Angelis and Opella, 2007; Hare *et al.*, 1995; Triba *et al.*, 2006; Wang *et al.*, 1998; Whiles *et al.*, 2002). Furthermore addition of small amounts of the monounsaturated lipid POPC does not hinder the formation of bicellar structures (De Angelis and Opella, 2007; Triba *et al.*, 2006). Moreover it is possible to replace the short chain phospholipid DHPC by the bile salt analogue CHAPSO (3-[(3-cholamidopropyl)dimethylammonio]-2-hydroxy-1-propanesulfonate) (Sanders and Prestegard, 1990). By adding small amounts of charged lipids, such as DMPG (1,2-dimyristoyl-*sn*-glycero-3-[phospho-rac-(1-glycerol)]), the long term colloidal stability can be enhanced (Prosser *et al.*, 1998b). The pH stability was increased by using ether-linked phospholipids (Aussenac *et al.*, 2005; Cavagnero *et al.*, 1999; Ottiger and Bax, 1999). Formation of bicelles has also been found for mixtures of phosphatidyl-cholines and polethyleneglycol-conjugated lipids (PEG-lipids) (Johansson *et al.*, 2005, 2007; Johnsson and Edwards, 2003; Sandstrom *et al.*, 2008). In such systems the PEG-lipids are located preferably in the highly curved edges of the disk, whereas the phospholipids, often with cholesterol, form the planar part of the disk (Johansson *et al.*, 2007; Johnsson and Edwards, 2003).

This chapter reports on an investigation of a mixture of DMPC and DMPE-DTPA which contained complexed lanthanide ions. The two phospholipids used here - DMPC and DMPE-DTPA - have the same acyl-chain length, but differ in head-group size. The system was studied with small angle neutron scattering (SANS) measurements, cryo-transmission electron microscopy (cryo-TEM) and ^{31}P NMR-spectroscopy. The SANS measurements were performed in a magnetic field of 8 T, at temperatures ranging from 2.5 to 30 °C with DMPE-DTPA which contained complexed thulium ions (Tm^{3+}). For the NMR measurements, Tm^{3+} was replaced by the diamagnetic lanthanum ion (La^{3+}) in order to prevent line shift and broadening (Prosser *et al.*, 1998b).

It was found that after appropriate preparation steps, i.e. extrusion through a polycarbonate membrane followed by a cooling step, bicelles formed from the phospholipid mixtures, without any need for a short chain lipid to cover the bicelle edge.

6.2 Materials and Methods

6.2.1 Materials

The phospholipids, 1,2-dimyristoyl-*sn*-glycero-3-phosphocholine (DMPC) and 1,2-dimyristoyl-*sn*-glycero-3-phosphoethanolamine-diethylene-triamine-pentaacetate (DMPE-DTPA), were purchased as chloroform solution from Avanti Polar Lipids (Alabaster, AL) and used without further purification. $TmCl_3$ (99.9%), $LaCl_3$ (99.9%), D_2O (99.9 atom % D) used for samples containing Tm^{3+} and D_2O (99.9 atom % D, containing 0.05 wt.% 3-(trimethylsilyl)propionic-2.2.3.3-d4 acid, sodium salt) used for sample containing La^{3+} were from Sigma-Aldrich (Buchs, Switzerland). Stock solutions of 10 mM $TmCl_3$ in MeOH and of 10 mM $LaCl_3$ in MeOH/H_2O (19/1 v/v) were prepared.

6.2.2 Bicelle Preparation

After weighing the lipid solution and lanthanides into a round bottom flask, chloroform and methanol were evaporated under a rotary evaporator followed by residual solvent removable under high vacuum overnight. The so formed dry lipid film was hydrated with D_2O and vortexed until a homogeneous suspension was obtained. Since La^{3+} was not completely dispersed, the pH of the suspension was adjusted to 7 with 0.1 M NaOH in H_2O. Five repeated freeze - thaw cycles were carried out by plunging the flask into liquid nitrogen followed by slow heating above the phase transition temperature (about 40 to 45 ℃). The extrusion was performed under nitrogen at 40 ℃ with "The Extruder" from Lipex Biomembranes (Vancouver, Canada) and Nucleopore polycarbonate membranes from Sterico (Dietikon, Switzerland) (Mui *et al.*, 2003; Walde and Ichikawa, 2001). The suspension was first passed 10 times through a membrane with 200 nm pores, followed by 10 times through a membrane with 100 nm pores. If samples were prepared without extrusion large lamellar structures were formed, even after freeze - thaw cycles. All samples were prepared with a DMPC:DMPE-DTPA:Lanthanide ratio of 4:1:1 and a total lipid concentration of 15 mM. The samples are denoted as DMPC/DMPE-DTPA·Tm or DMPC/DMPE-DTPA·La in the text. Samples were stored at room temperature before measurements and were stable over at least one week.

6.2.3 Cryo-TEM

The samples were analyzed by cryo transmission electron microscopy (cryo-TEM). A volume of $3.5\,\mu$l of the bicellar suspension was mounted onto holey carbon grids (from Quantifoil, Jena, Germany), blotted to make thin aqueous films under controlled temperature, followed by plunging into liquid ethane at the temperature of liquid nitrogen. For samples frozen from room temperature and from $30\,°C$ a VitrobotTM apparatus (from the FEI company, Eindhoven, The Netherlands) was used. For the samples frozen from $5\,°C$, the sample was pre-cooled in a water bath and the manual blotting apparatus was transferred into a cold room with $5\,°C \pm 0.5\,°C$. Every part of equipment coming into contact with the sample was held for at least $4\,$h in the cold room prior to sample freezing. The grids were examined at the temperature of liquid nitrogen using a cryo-holder (model 626, from Gatan, USA) and a Tecnai G2 F20 microscope (from the FEI company) equipped with a field emission gun and Tridem energy filter (from Gatan) operated at an accelerating voltage of $200\,$kV. The data were recorded by a 2048×2048 CCD camera (from Gatan).

6.2.4 SANS

SANS experiments were performed on the SANS-I beam line at PSI, Villigen, Switzerland using a super conductive magnet with horizontal field of $8\,$Tesla perpendicular to the neutron beam. The neutron wavelength was fixed at $8\,$Å. Data were collected on a two-dimensional ^{3}He detector at distances of 2, 6, and $18\,$m covering a momentum transfer q of $0.003 \leq q \leq 0.15\,$Å^{-1}. After correction for background radiation, empty cell scattering and detector efficiency, the 2D intensity maps were radial averaged and sectoral averaged with an opening angle of $15\,°$ perpendicular and parallel to the magnetic field direction. Data was fitted with a form factor for partly aligned flat cylinders.

6.2.5 SANS Model for Partly Aligned Flat Cylinders

The scattering intensity of a flat cylinder $I_{cyl}(q)$ with a given orientation γ relative to the scattering vector is given by Eq. 6.1 (Hayter and Penfold, 1984).

$$I_{cyl}(q,\gamma) = \left(2\pi R^2 L \Delta\eta \frac{J_1\left(qR\sin\gamma\right)}{qR\sin\gamma} \frac{\sin\left(\frac{qL}{2}\cos\gamma\right)}{\frac{qL}{2}\cos\gamma}\right)^2 \tag{6.1}$$

where γ is the angle between the scattering vector $\vec{q}$ and the cylinder axis $\vec{n}$. L is the length of the cylinder, R its radius, $\Delta\eta$ the scattering length density contrast relative to the solvent and $J_1(x)$ is the first order Bessel function of the first kind. γ can be calculated (see Fig. 6.1) from the orientation (θ,ϕ) of the cylinder and the direction of the scattering vector ψ in the plane of the detector by Eq. 6.2.

$$\cos\gamma = \frac{\vec{q} \cdot \vec{n}}{|\vec{q}|\,|\vec{n}|} = \begin{pmatrix} \cos\psi \\ 0 \\ \sin\psi \end{pmatrix} \cdot \begin{pmatrix} \cos\theta \\ \sin\theta\sin\phi \\ \sin\theta\cos\phi \end{pmatrix} = \cos\psi\cos\theta + \sin\psi\sin\theta\cos\phi \quad (6.2)$$

If the orientation distribution of the orientation vector $\vec{n}$ is described by $p(\theta,\phi)$ the scattering intensity is given by Eq. 6.3

$$I_{cyl}(q) = \int_0^\pi \int_0^{2\pi} d\theta d\phi \sin(\theta)\, p(\theta,\phi) \left(2\pi R^2 L\Delta\eta \frac{J_1(qR\sin\gamma)}{qR\sin\gamma} \frac{\sin\left(\frac{qL}{2}\cos\gamma\right)}{\frac{qL}{2}\cos\gamma} \right)^2 \quad (6.3)$$

For this form factor it is assumed that the orientation distribution is independent of ϕ, i.e. $p(\theta,\phi) = p(\theta)$ and that $p(\theta) = p(\pi\text{-}\theta)$, which means that turning the cylinder by 180° results in the same scattering intensity. Instead of assuming a special parameterization of $p(\theta)$ the orientation distribution was expanded in terms of Legendre polynomials $P_l(\cos\theta)$

$$p(\theta) = \sum_{l=0,\text{even}}^{\infty} \frac{2l+1}{2} \langle P_l \rangle P_l(\cos\theta) \quad (6.4)$$

Due to the symmetry $p(\theta) = p(\pi\text{-}\theta)$ all terms with odd values for l are zero and only the even terms need to be considered. During our analysis it turned out that it was sufficient to consider only the terms $l = 0$ and 2. As $\int_0^\pi p(\theta)\sin\theta d\theta = 1$ the zero order parameter is $\langle P_0 \rangle = 1$, so that $\langle P_2 \rangle$ is the only fit parameter of the orientation distribution. $\langle P_2 \rangle$ can vary between -1/2 (perfectly aligned in the direction $\theta = \pi$) and 1 (perfectly aligned in the direction $\theta = 0$). The Legendre polynomial $\mathrm{P}_2(\cos\theta)$ is defined as $\mathrm{P}_2(\cos\theta) = \frac{1}{2}\left(3\cos^2\theta - 1\right)$.
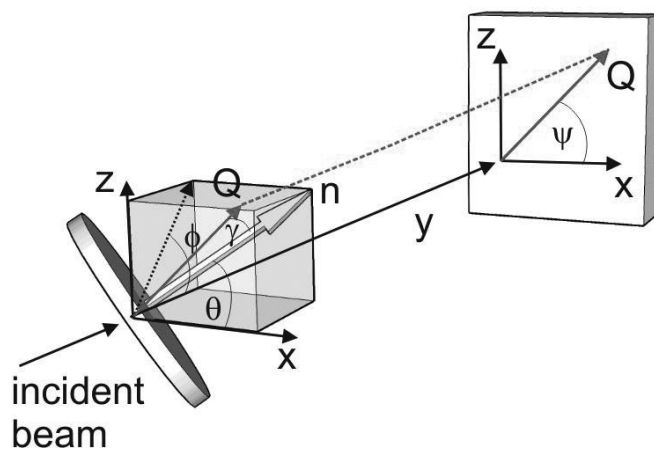
Figure 6.1: Sketch which defines the angles of the orientation $\vec{n}$ of partly aligned disks relative to the scattering vector $\vec{q}$.

6.2.6 ^{31}P NMR

^{31}P NMP spectra were acquired at 283 MHz using a Bruker Biospin spectrometer operating with a 16.4 T field. Temperature was adjusted with a flow of cold nitrogen gas, heated to the appropriate temperature.

6.3 Results and Discussion

In the context of a study of possible effects of magnetic fields on phospholipid vesicles (chapter 5), it was found that a mixture of DMPC and DMPE-DTPA with complexed lanthanides in a molar lipid ratio of 4:1 and a lipid concentration of 15 mM in water forms non vesicular structures. These structures were now investigated using SANS, cryo-TEM and NMR-spectroscopy. SANS and cryo-TEM are complementary methods for structure determination of self-assembly systems. While SANS yields average information over the whole sample volume, cryo-TEM is a model independent measurement method, whereby individual objects can be observed directly.

6.3.1 Cryo-TEM Measurements

Cryo-TEM micrographs were taken of a mixture of DMPC and DMPE-DTPA with complexed thulium (DMPC/DMPE-DTPA·Tm). Fig. 6.2 shows small disks of phospholipids (bicelles), which are randomly oriented. Some of the bicelles are seen edge-on (*a* in Fig. 6.2) or face-on (*b* in 6.2) The bicelles have a radius of roughly 20 nm.

Cryo-TEM micrographs of DMPC/DMPE-DTPA·La frozen from 22 °C are shown in Fig. 6.3. The presence of bicelles is again obvious. Fig. 6.3 A is taken at a tilting angle of 0° whereas the sample in Fig. 6.3 B was tilted at 30°. The ice crystal (arrow *b*) in both micrographs can be taken as a reference point, the bicelle next to it (arrow *a*) is seen edge-on in Fig. 6.3 A and face-on in Fig. 6.3 B. Fig. 6.4 shows a sketch to clarify how the two micrographs in Fig. 6.3 were obtained. The solid line in Fig. 6.3A is parallel to the tilting axis of the sample holder. By tilting the sample holder the projection of the electron beam through the sample changes, exposing surfaces which were not visible without tilting. For example, the bicelle shown with arrow (*a*) is seen edge-on in Fig. 6.3A. By tilting the sample holder, the outline of the projection becomes ellipsoidal, thus proving the disk shape of the object. In comparison, the spherical ice particles indicated by arrow (*b*) do not change significantly in the tilted projection, neither would e.g. a spherical vesicle.

Micrographs taken from DMPC/DMPE-DTPA·La frozen from 30 °C show bicelles corresponding in shape and size to those shown in Fig. 6.3 (data not shown).
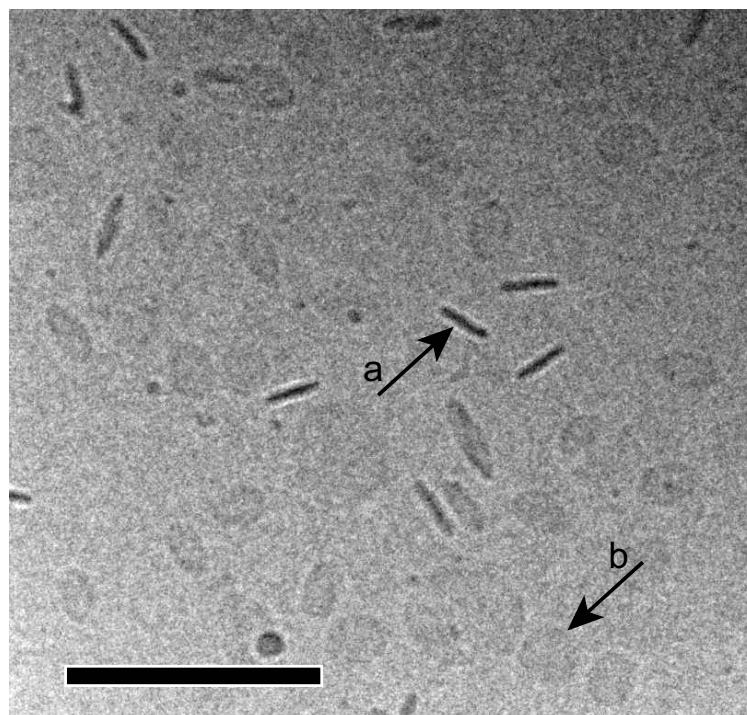
Figure 6.2: Cryo-TEM micrograph of the sample used for SANS measurements showing bicelles formed by DMPC/DMPE-DTPA complexed with Tm^{3+} at 5 °C. Arrows point to bicelles edge-on (*a*) and face-on (*b*). Scale bar = 200 nm.
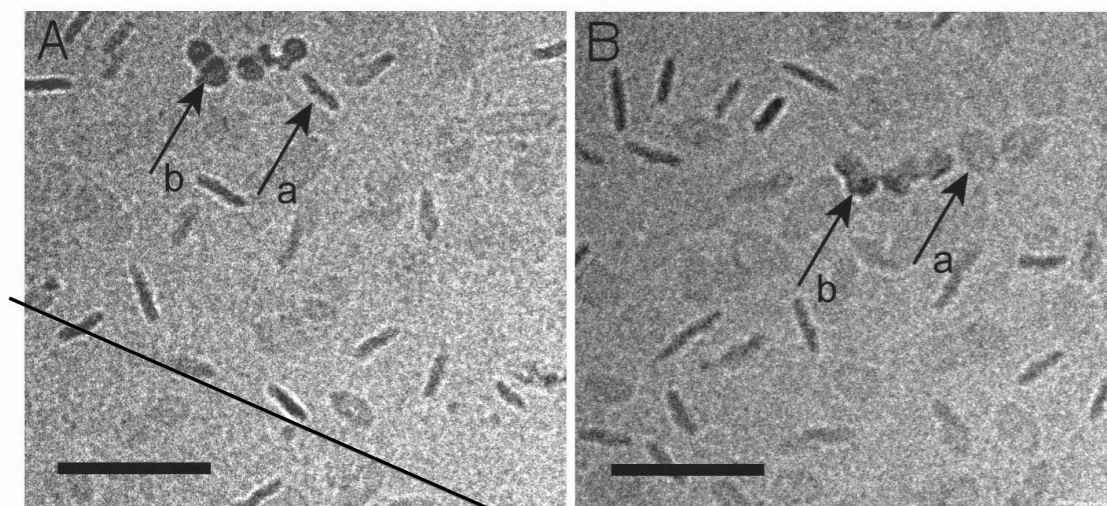
Figure 6.3: Cryo-TEM micrographs of bicelles formed by DMPC/DMPE-DTPA·La at 22 °C. A is taken at 0° tilting angle and B was taken at a tilting angle of 30° around the axis shown by the solid line. Arrow (*a*) points to the same bicelle edge-on (A) and face-on (B). Arrow (*b*) points to a contamination of ice crystal as reference point. Scale bar = 100 nm.
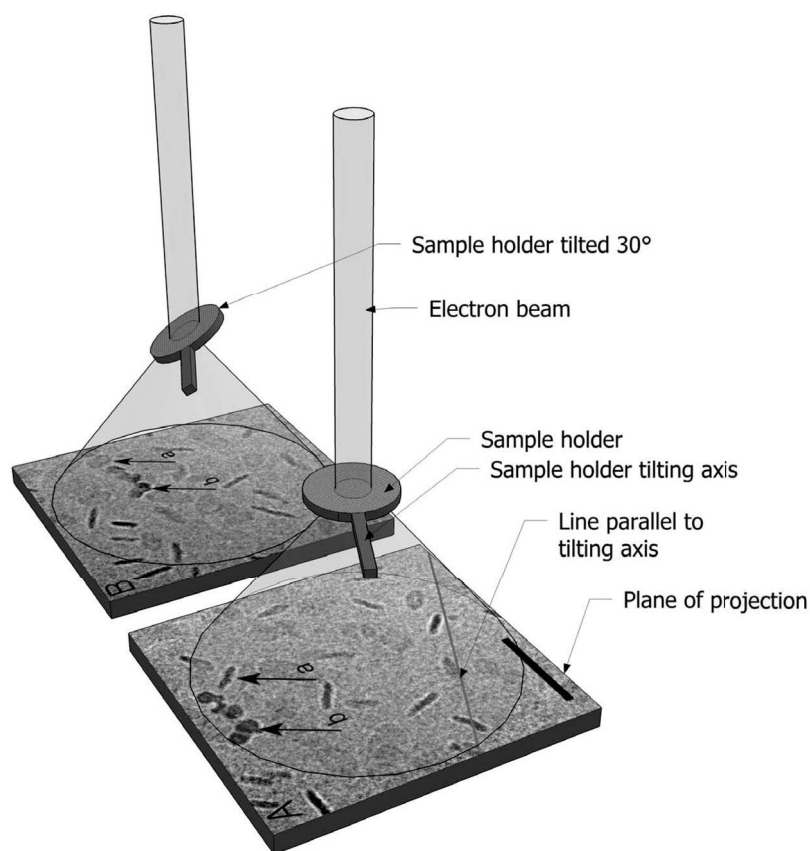
Figure 6.4: Sketch illustrating how the two cryo-TEM micrographs in Fig. 6.3 were obtained. The solid line is parallel to the tilting axis of the sample holder. By tilting the sample holder by 30° the projection of the electron beam through the sample changes, exposing surfaces which were not visible without tilting. For example, the bicelle shown with arrow (*a*) is seen edge-on in Fig. 6.3 A. By tilting the sample holder, the outline of the projection becomes ellipsoidal, thus proving the disk shape of the object. In comparison, the spherical ice particles indicated by arrow (*b*) do not change significantly in the tilted projection.

The importance of the extrusion step during preparation is illustrated in Fig. 6.5. Fig. 6.5 A shows a mixture of DMPC/DMPE-DTPA·Tm after rehydration and before the freeze-thaw cycles, Fig. 6.5 B show the same sample after five freeze-thaw cycles, before extrusion. Predominantly large lamellar structures are seen in both micrographs, and no bicelles are found. The small structures in Fig. 6.5 A could be either ice contamination from the freezing procedure or phospholipid micelles, which are destroyed in the following freeze-thaw cycles.
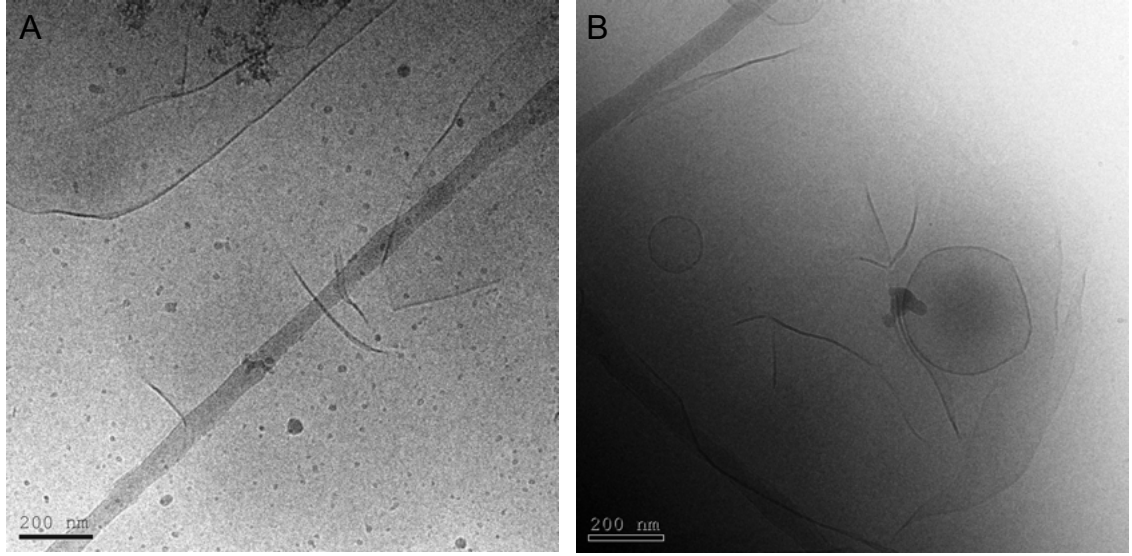
Figure 6.5: Cryo-TEM micrograph of a mixture of DMPC/DMPE-DTPA·Tm at 22 °C. (A) is taken from a sample after rehydration and before the freeze-thaw cycles, (B) after the freeze-thaw cycles but before the extrusion step. Scale bar = 200 nm.

6.3.2 SANS Measurements

SANS measurements were made with the same sample of DMPC/DMPE-DTPA·Tm as used for cryo-TEM. The experiments were carried out in presence of a magnetic field of 8 T. After an initial measurement at 30 °C the temperature was lowered step-wise to 2.5 °C. Measurements were made at 30, 22, 17.5, 15, 10, 7.5, 5 and 2.5 °C respectively. The SANS curves were fitted with a model for partly aligned flat disks (chapter 6.2.5), in accordance to the bicelle structures observed with cryo-TEM and to the slight anisotropy of the SANS pattern, which clearly indicates an orientation in the magnetic field. Fig. 6.6 shows the SANS sectoral intensity average of DMPC/DMPE-DTPA·Tm at 2.5 °C and 8 T from overlayed curves from 18 m, 6 m, and 2.5 m detector distance, as well as the corresponding fit. The bicelle radius R for the best fit was 17.1 nm and bilayer thickness L was 4.3 nm, in agreement with the size of the bicelles found by cryo-TEM. The second order parameter of the Legendre polynomial series P_2 for the best fit was 0.058. The corresponding orientation distribution (inset Fig. 6.6) indicates that the probability of bicelles oriented with the normal parallel to the magnetic field ($\theta = 0$) is slightly higher than the probability of an orientation perpendicular to the magnetic field ($\theta = \pi/2$).
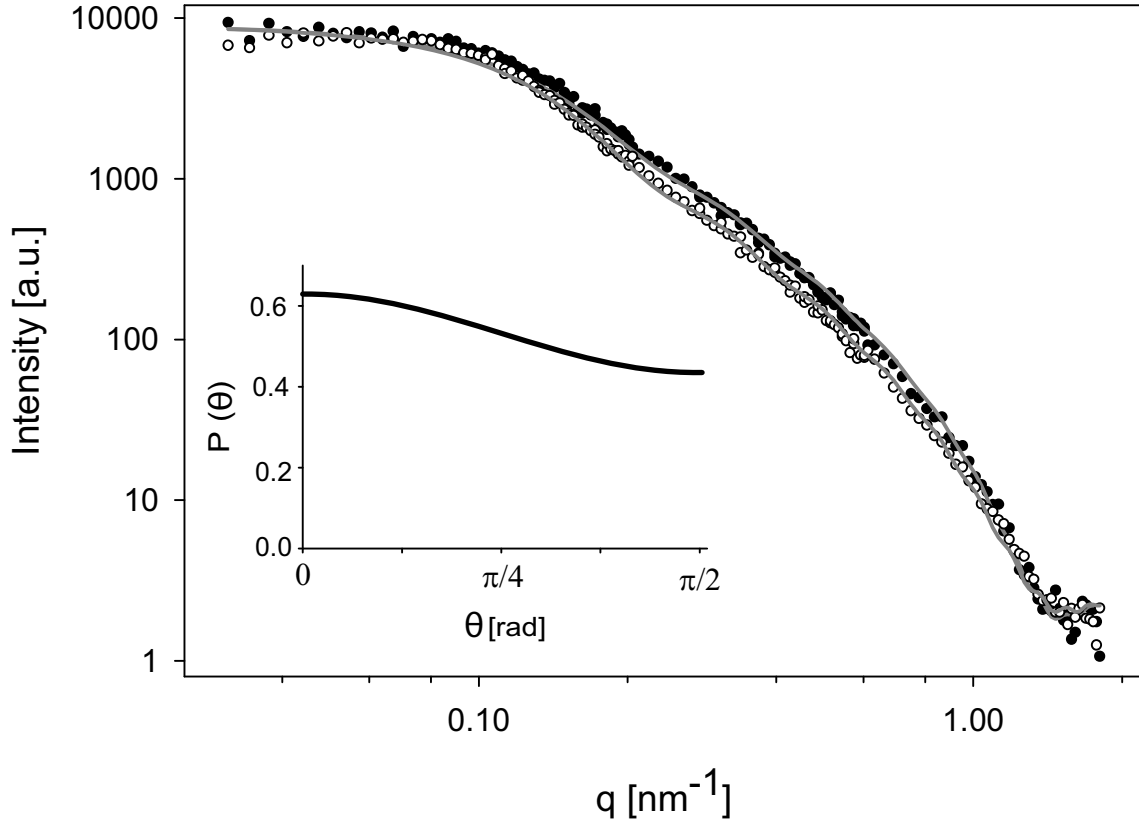
Figure 6.6: Sectoral averaged SANS curves of DMPC/DMPE-DTPA·Tm at 2.5 °C and corresponding fit with a model for partly aligned flat cylinders. Filled symbols mark the 15° horizontal sector in direction of the magnetic field and open symbols the 15° vertical sector perpendicular to the magnetic field. Fit results indicate an orientation with the bilayer normal parallel to the magnetic field as shown in the orientation distribution (inset).

At temperatures between 2.5 °C and 22 °C SANS measurements were made at 18 m detector distance only. While this q-range contains information about the overall size of the bicelles, no information is given about the thickness of the bicelle and an exact fit of the orientation is not possible. Guinier fits at all temperatures showed no significant difference in the bicelle radius and no particular trend was observed. At 30 °C additional SANS measurements were carried out with detectoral distance of 6 m. Like at 2.5 °C, these resulting sectoral averaged SANS curves could be fitted to a model for partly aligned flat cylinders. The bicelle radius R for the best fit was 18.5 nm, bilayer thickness L 3.9 nm and 2nd order parameter of the Legendre polynome series P_2 for the best fit was 0.031. The result indicates that at 30 °C bicelles are slightly bigger and less thick than at 2.5 °C, as can be expected for lipids

in the fluid-analogue state above $T_m = 25\,°C$ (Caffrey and Hogan, 1992; Koynova and Caffrey, 1998). Faster lipid motion at higher temperatures can explain the less pronounced orientation.

6.3.3 ^{31}P NMR Measurements

^{31}P NMR spectra were recorded from the sample analyzed by cryo-TEM shown in Fig. 6.3 (DMPC/DMPE-DTPA·La). Diamagnetic La^{3+} instead of paramagnetic Tm^{3+} was used in order to prevent shifts and broadenings of the NMR line. The spectra shown in Fig. 6.7 were recorded in sequence from top to bottom. All spectra showed a single broad resonance at the position of the isotropic chemical shift. This is in contrast to what would be expected for i) oriented structures or ii) larger entities such as vesicles. The first measurement (Fig. 6.7 A), taken at room temperature right after extrusion, shows an isotropic peak at $-1\,ppm$. Cooling the sample to $5\,°C$ increased the width (Fig. 6.7 B), typical for slower phospholipid motion at this temperature. Reheating the sample (Fig. 6.7 C) resulted in a spectrum differing from the one recorded before the cooling step (Fig. 6.7 A). The peak is now considerably narrower, indicating that an irreversible change in the size of the bicelles occurred. If the cooling cycle is performed outside of a magnetic field in a water bath (10 h at $5\,°C$) an identical NMR-spectrum as the one shown in (Fig. 6.7 C) is obtained. This size reduction of the bicelles by a cooling step is supported by size evaluation of cryo-TEM micrographs. Bicelle radius in the micrograph of a sample before the cooling step were $20\pm8\,nm$ whereas bicelles in the micrographs of the sample after the cooling step had a size of $18\pm5\,nm$. Heating the sample to $40\,°C$ (Fig. 6.7D) and cooling it back to room temperature did not lead to any further changes in the NMR-spectrum (comparison of Fig. 6.7C and Fig. 6.7E). All NMR spectra recorded are in agreement with small bicelles, whose rates of tumbling determine the width of the resonance. Cooling the sample to $5\,°C$ for around 10 h led to a homogenization and a slight size reduction of the bicelles.

Structural information obtained with all three methods used, SANS, cryo-TEM and ^{31}P NMR is consistent with small dispersed disk in a aqueous mixture of DMPC/DMPE-DTPA complexed with either Tm^{3+} or La^{3+}. Important for the preparation is an extrusion at $40\,°C$. Furthermore a cooling step at $5\,°C$ can help to homogenize the disks to an average size of $35\,nm$. Samples with thulium can be oriented in a magnetic field ($8\,T$), as shown with SANS, whereas samples with lanthanum show no orientation in the magnetic field as shown with NMR.
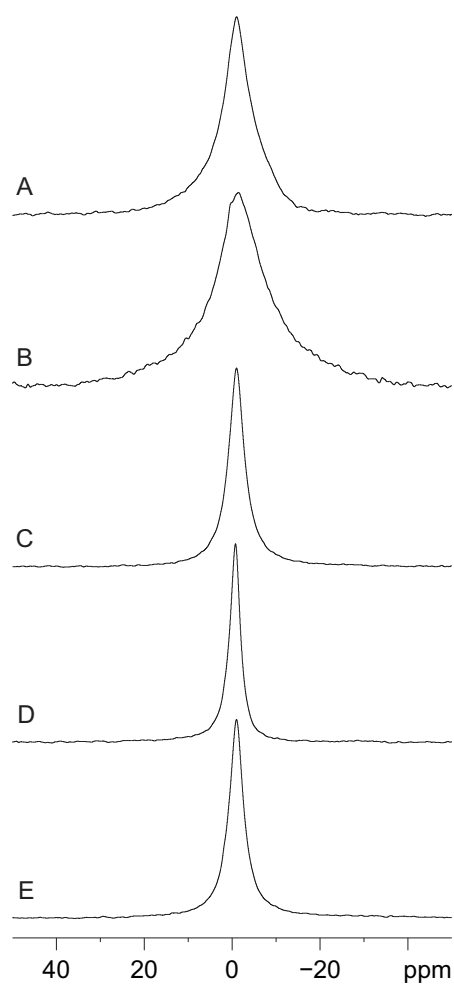
Figure 6.7: ^{31}P NMR spectra of DMPC/DMPE-DTPA·La bicelles at (A) T = 22 ℃, right after extrusion step, (B) 5 ℃, (C) 22 ℃, (D) 40 ℃, (E) 22 ℃. The difference in peak width between (A) and (D) indicates the irreversible decrease of the bicelle size. Heating of the sample up to 40 ℃ causes no irreversible change in the 22 ℃ spectra (comparison C and E). The isotropic peak at −1 ppm correspond with small and fast tumbling bicelles.

6.4 Conclusion

In this chapter, it is shown that bicelles can be formed from a mixture of DMPC and DMPE-DTPA·Lanthanide. Usually, phospholipid bicelles consist of a long chain phospholipid plane with a short chain lipid covering the edges (Katsaras *et al.*, 2005). Here, bicelles are shown which are formed with only one type of fatty acid tail, myristoyl. The necessary local curvature to cover the edge of the bilayer disk is most likely induced by the large headgroup of DMPE-DTPA complexed with either Tm^{3+} or La^{3+} (Fig. 6.8).
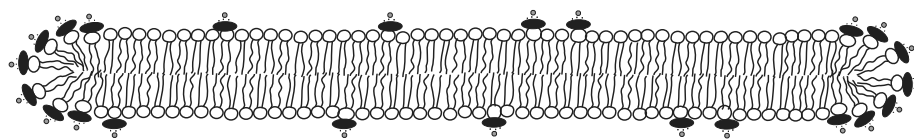
Figure 6.8: Sketch of a bicelle formed by a mixture of DMPC, building the bilayered center of the disk and DMPE-DTPA complexed with Tm^{3+} covering the edges.

The method of preparation, including extrusion through a polycarbonate membrane followed by a cooling step, is essential to obtain the bicelles. The so formed bicelles are stable over a temperature range of 2.5 °C to 30 °C for at least one week as shown with SANS and cryo-TEM. SANS data obtained in a magnetic field of 8 T indicate that bicelles with thulium attached to DMPE-DTPA are slightly orientable with the bilayer normal parallel to the magnetic field.

7 Concluding Remarks and Outlook

Within the scope of this work, a magnet rheometer laboratory was set up (chapter 3) and used to investigate the influence of strong magnetic fields on biomolecular assemblies formed by two types of glycerol based lipids. The first was a triacylglyceride mixture in the form of cocoa butter, the second was phosphatidylcholine forming vesicles and bicelles. The experiments made in the rheometer laboratory were complemented by a number of other investigative methods, such as SANS under magnetic field, ^{31}P NMR, DSC, DLS and cryo-TEM. As explained in the introduction, molecular assemblies are more promising to react to magnetic fields than individual molecules, because of the randomizing thermal fluctuation, kT, which has to be overcome.

Cocoa butter was crystallized under different conditions in a magnetic field. At the conditions tested, no significant influence on the crystal type or crystallization kinetics was found (chapter 4). It is unclear, whether a magnetic field effect is not observed because of the heterogeneous composition of cocoa butter, or whether the experimental conditions were not suitable for a significant magnetic field interaction. The results however indicate, that magnetic field crystallization of cocoa butter may not be promising for industrial application, as the experimental conditions were set close to industrial tempering conditions. However, additional experiments in stronger magnetic fields coupled with strong field gradients could be considered, as described in the introduction. Under these conditions, magnetic orientation of crystal nuclei could in theory be coupled with a damping of natural convection, which occurs due to density difference between the compact crystals and the liquid cocoa butter fraction. As observed for crystallizing proteins, this may have an effect on the crystal quality. Simulations of the magnetic field generated by the superconductive magnet used in the magnet rheometer set up (chapter 3.2.2) yielded a maximal field gradient $B\nabla B$ of $150\,\mathrm{T^2 m^{-1}}$ close to the upper end of the bore, which corresponds to a reduction of gravity of about $0.1\,\mathrm{g}$. A new magnet would be needed to achieve significant magnetic field gradients.

Combination of strong magnetic fields and strong field gradients could also be used to further investigate the phospholipid structures, where a clear magnetic field effect was found. Field gradients would induce an additional stress on the membrane, because the lipids doped with paramagnetic lanthanides would be attracted in direction of the field gradient, and the diamagnetic phosphatidylcholine background molecules would be repulsed.

It was shown that vesicles composed of POPC and DMPE-DTPA with chelated lanthanides form magnetic field orientable domains at certain temperatures (chapter 5). The direction of orientation depends on the type of lanthanide used. An interesting continuation of this work would be to form giant vesicles with the same composition as the vesicles investigated here. Giant vesicles have a much larger aggregation number, and therefore can be expected to be more responsive to magnetic fields. The use of giant vesicles would open up other possibilities. They are large enough to be seen with light microscopy, which could allow direct observation in magnetic fields. With the use of micro manipulators, asymmetric giant vesicles could be formed by injecting one type of lanthanide into the vesicle, and adding another from the outside. By using lanthanides with opposite sign of $\Delta\chi$, additional stresses could be applied to the membrane.

Chapter 6 reports on a new bicellar structure formed of DMPC and DMPE-DTPA with complexed lanthanides. This disk like planar structure slightly orients in magnetic fields. Related structures composed of a long chain and a short chain phospholipid have been shown to orient in magnetic fields as well (see references in chapter 6), but only when forming large lamellar phases or at very high total lipid concentrations. Bicellar phases are used to orient trans membrane proteins for NMR measurements. Could such structures be used for other applications?

Mixtures of DMPC and DHPC have exhibited a wealth of different morphologies, some of them orientable in magnetic fields. Fig. 7.1 shows an overview of currently accepted morphologies. The complexity of DMPC/DHPC phase diagrams is due to the temperature dependent miscibility of the two lipids, and the relatively high solvability of DHPC in water. For some formulations, doping with Tm^{3+} led to the formation of an interesting smectic mesophase composed of large lamellar structures which orient in magnetic fields (Katsaras *et al.*, 2005; Nieh *et al.*, 2002; Prosser *et al.*, 1998c) (7.1 C). Follow up work could investigate, whether such structures could be modified to exhibit e.g. anisotropic optical or electrical properties, or be used to direct mass transport. Optimized properties to look for would be orientability at lower field strengths, increased rigidity, and less complex phase diagrams.

The here presented novel bicellar structure, formed with all myristoyl fatty acid tails, could represent a first step in this direction. Further investigation of this system would help to gain a better understanding of the bicelle forming mechanism, allowing for a more directed development of novel structures.
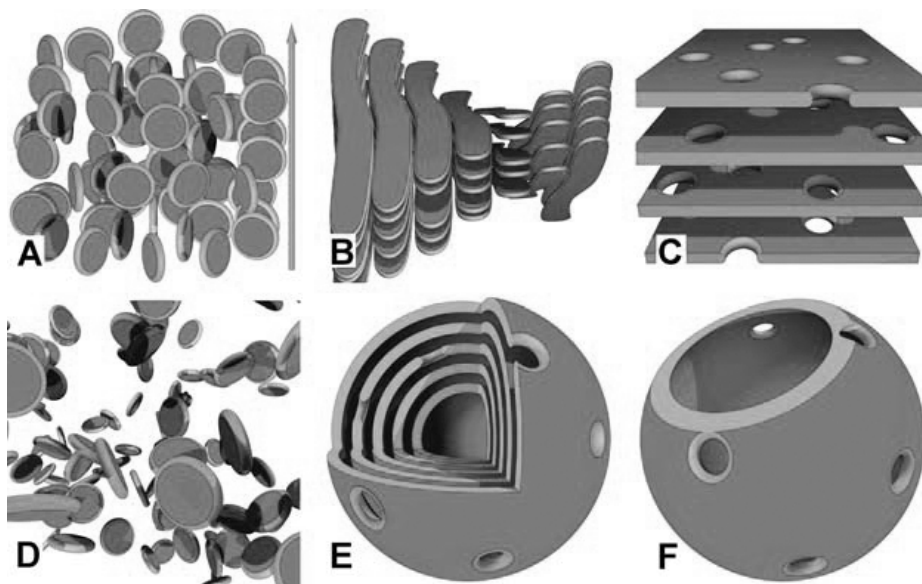

Figure 7.1: Different morphologies found for DMPC/DHPC lipid mixtures, adapted from Katsaras *et al.* (2005). (*A*) A nematic phase of bicelles oriented with the bilayer normals perpendicular to the externally applied magnetic field (arrow). This type of orientation has only been observed for high total lipid concentrations, and is believed to be due to a sterical interaction between the bicelles. (*B*) A cholesteric or chiral nematic phase, where bicellar layers twist in a helical formation. The high viscosity observed in this phase is due to the entanglement of the elongated bilayered micelles. (*C*) Positively aligned extended perforated lamellae, or smectic phases, can form for systems doped with a lanthanide with $\Delta \chi \gg 0$ such as Tm^{3+}. The lamellar sheets are believed to be interspersed with holes rimmed by DHPC. The appearance of this phase is opaque and fluid. (*D*) An isotropic dispersion of bicelles. In this phase the bilayered micelles are randomly distributed in the water solvent, exhibiting no long range positional or orientational order. The solution is generally of low viscosity and colorless. (*E*) Multilamellar and (*F*) unilamellar vesicles, with holes rimmed by DHPC.

It would be of interest to further widen the search for magnetic field orientable structures. New types of chelator lipids were already successfully synthesized in this work.

In a further step, the synthesis of lipids with additional desired properties for bicelle formation could be envisaged. For example, trials to optimize the system with respect to rigidity and orientability in magnetic fields could be made with a polymerizable (crosslinking) lipid, containing a chelator molecule covalently bound to the head group.

Bibliography

Anghel, V. N. P., N. Kucerka, J. Pencer, and J. Katsaras: *Scattering from laterally heterogeneous vesicles. II. The form factor.* Journal of Applied Crystallography, 40:513–525, 2007.

Aussenac, F., B. Lavigne, and E. J. Dufourc: *Toward bicelle stability with ether-linked phospholipids: Temperature, composition, and hydration diagrams by H-2 and P-31 solid-state NMR.* Langmuir, 21(16):7129–7135, 2005.

Bacia, K., P. Schwille, and T. Kurzchalia: *Sterol structure determines the separation of phases and the curvature of the liquid-ordered phase in model membranes.* Proceedings of the National Academy of Sciences of the United States of America, 102 (9):3272–3277, 2005.

Bammer, R., A. J. de Crespigny, D. Howard, S. Seri, Y. Hashiguchi, A. Nakatani, and M. E. Moseley: *A comparative evaluation of CH3-DTPA-Gd (NMS60) for contrast-enhanced magnetic resonance angiography.* Magnetic Resonance Imaging, 22(5): 619–624, 2004.

Baumgart, T., S. T. Hess, and W. W. Webb: *Imaging coexisting fluid domains in biomembrane models coupling curvature and line tension.* Nature, 425(6960):821–824, 2003.

Beckett, S.T.: *Industrial Chocolate Manufacture and Use.* Blackie, A. & P., 2nd edition, 1994.

Beckett, S.T.: *Process for controlling the solidification or crystallization of fats and fat-containing foods*, PCT/EP1999/009567, 2002.

Binnemans, K. and C. Gorller-Walrand: *Lanthanide-containing liquid crystals and surfactants.* Chemical Reviews, 102(6):2303–2345, 2002.

Bolliger, S., B. Breitschuh, M. Stranzinger, T. Wagner, and E. J. Windhab: *Comparison of precrystallization of chocolate.* Journal of Food Engineering, 35(3):281–297, 1998.

Bolliger, S., Y. T. Zeng, and E. J. Windhab: *In-line measurement of tempered cocoa butter and chocolate by means of near-infrared spectroscopy.* Journal of the American Oil Chemists Society, 76(6):659–667, 1999.

Brumm, T., A. Mops, C. Dolainsky, S. Bruckner, and T. M. Bayerl: *Macroscopic orientation effects in broadline NMR-spectra of model membranes at high mgnetic-field strength - a method preventing such effects.* Biophysical Journal, 61(4):1018–1024, 1992.

Caffrey, M. and J. Hogan: *Lipidat - a database of lipid phase-transition temperatures and enthalpy changes - DMPC data subset analysis.* Chemistry and Physics of Lipids, 61(1):1–109, 1992.

Cavagnero, S., H. J. Dyson, and P. E. Wright: *Improved low pH bicelle system for orienting macromolecules over a wide temperature range.* Journal of Biomolecular NMR, 13(4):387–391, 1999.

D'Arceuil, H. E., A. J. de Crespigny, L. Pelc, D. Howard, M. Alley, S. Seri, Y. Hashiguchi, A. Nakatani, and M. E. Moseley: *An MRA study of vascular stenosis in a pig model using CH3-DTPA-Gd (NMS60) and Gd-DTPA.* Magnetic Resonance Imaging, 22(9):1243–8, 2004.

De Angelis, A. A. and S. J. Opella: *Bicelle samples for solid-state NMR of membrane proteins.* Nature Protocols, 2(10):2332–2338, 2007.

Dimick, P. S. and D. M. Manning: *Thermal and compositional properties of cocoa butter during static crystallization.* Journal of the American Oil Chemists Society, 64(12):1663–1669, 1987.

Egelhaaf, S. U., E. Wehrli, M. Muller, M. Adrian, and P. Schurtenberger: *Determination of the size distribution of lecithin liposomes: A comparative study using freeze fracture, cryoelectron microscopy and dynamic light scattering.* Journal of Microscopy-Oxford, 184:214–228, 1996.

Foubert, I., P. Vanrolleghem, O. Thas, and K. Dewettinck: *Influence of chemical composition on the isothermal cocoa butter crystallization.* Journal of Food Science, 69(9):478–487, 2004.

Grant, C. W. M., S. Karlik, and E. Florio: *A liposomal MRI contrast agent - phosphatidylethanolamine DTPA.* Magnetic Resonance in Medicine, 11(2):236–243, 1989.

Hare, B. J., J. H. Prestegard, and D. M. Engelman: *Small angle x-ray scattering studies of magnetically oriented lipid bilayers.* Biophysical Journal, 69(5):1891–1896, 1995.

Harroun, T. A., M. Koslowsky, M. P. Nieh, C. F. de Lannoy, V. A. Raghunathan, and J. Katsaras: *Comprehensive examination of mesophases formed by DMPC and DHPC mixtures.* Langmuir, 21(12):5356–5361, 2005.

Hartmann, W., H. J. Galla, and E. Sackmann: *Direct evidence of charge-induced lipid domain-structure in model membranes.* Febs Letters, 78(2):169–172, 1977.

Hayter, J. B. and J. Penfold: *Use of viscous shear alignment to study anisotropic micellar structure by small-angle neutron-scattering.* Journal of Physical Chemistry, 88(20):4589–4593, 1984.

Helfrich, W.: *Lipid bilayer spheres - deformation and birefringence in magnetic-fields.* Physics Letters A, 43(5):409–410, 1973.

Himawan, C., V. M. Starov, and A. G. F. Stapley: *Thermodynamic and kinetic aspects of fat crystallization.* Advances in Colloid and Interface Science, 122(1-3):3–33, 2006.

Hjelm, R. P., C. D. Schteingart, A. F. Hofmann, and P. Thiyagarajan: *Structure of conjugated bile salt-fatty acid-monoglyceride mixed colloids: Studies by small-angle neutron scattering.* Journal of Physical Chemistry B, 104(2):197–211, 2000.

Hong, F. T.: *Magnetic-field effects on biomolecules, cells, and living organisms.* Biosystems, 36(3):187–229, 1995.

Imai, H.: *Domain growth dynamics on vesicle.* Reports of the Institute of Fluid Science, Tohoku University, 19:1–5, 2007.

Johansson, E., C. Engvall, M. Arfvidsson, P. Lundahl, and K. Edwards: *Development and initial evaluation of PEG-stabilized bilayer disks as novel model membranes.* Biophysical Chemistry, 113:183–192, 2005.

Johansson, E., A. Lundquist, S. Zuo, and K. Edwards: *Nanosized bilayer disks: Attractive model membranes for drug partition studies.* Biochimica et Biophysica Acta-Biomembranes, 1768:1518–1525, 2007.

Johnsson, M. and K. Edwards: *Liposomes, disks, and spherical micelles: Aggregate structure in mixtures of gel phase phosphatidylcholines and poly(ethylene glycol)-phospholipids.* Biophysical Journal, 85:3839–3847, 2003.

Katsaras, J., T. A. Harroun, J. Pencer, and M. P. Nieh: *"Bicellar" lipid mixtures as used in biochemical and biophysical studies.* Naturwissenschaften, 92(8):355–366, 2005.

Kiselev, M. A., E. V. Zemlyanaya, V. K. Aswal, and R. H. H. Neubert: *What can we learn about the lipid vesicle structure from the small-angle neutron scattering experiment?* European Biophysics Journal with Biophysics Letters, 35(6):477–493, 2006.

Kiselev, M. A., T. Gutberlet, A. Hoell, V. L. Aksenov, and D. Lombardo: *Orientation of the DMPC unilamellar vesicle system in the magnetic field: SANS study.* Chemical Physics, 345(2-3):181–184, 2008.

Kleinert, J.: *Cocoa butter and chocolate: The correlation between tempering and structure.* Revue Internationale Chocolat, 25:386–399, 1970.

Knoll, W., J. Haas, H. B. Stuhrmann, H. H. Fuldner, H. Vogel, and E. Sackmann: *Small-angle neutron scattering of aqueous dispersions of lipids and lipid mixtrues - a contrast variation study.* Journal of Applied Crystallography, 14:191–202, 1981.

Korlach, J., P. Schwille, W. W. Webb, and G. W. Feigenson: *Characterization of lipid bilayer phases by confocal microscopy and fluorescence correlation spectroscopy.* Proceedings of the National Academy of Sciences of the United States of America, 96(15):8461–8466, 1999.

Koynova, R. and M. Caffrey: *Phases and phase transitions of the phosphatidylcholines.* Biochimica et Biophysica Acta, 1376(1):91–145, 1998.

Kucerka, N., S. Tristram-Nagle, and J. F. Nagle: *Structure of fully hydrated fluid phase lipid bilayers with monounsaturated chains.* Journal of Membrane Biology, 208(3):193–202, 2006.

Kurashima, H., H. Abe, and S. Ozeki: *Magnetic-field-induced deformation of lipid membranes.* Molecular Physics, 100(9):1445–1450, 2002.

Liburdy, R. P., T. S. Tenforde, and R. L. Magin: *Magnetic field-induced drug permeability in liposome vesicles.* Radiation Research, 108(1):102–111, 1986.

Lin, S. X., M. Zhou, A. Azzi, G. J. Xu, N. I. Wakayama, and M. Ataka: *Magnet used for protein crystallization: Novel attempts to improve the crystal quality.* Biochemical and Biophysical Research Communications, 275(2):274–278, 2000.

Lipowsky, R. and R. Dimova: *Domains in membranes and vesicles.* Journal of Physics-Condensed Matter, 15(1):31–45, 2003.

Maret, G. and K. Dransfeld: *Biomolecules and polymers in high steady magnetic-fields.* Topics in Applied Physics, 57:143–204, 1985.

Masui, T., M. Imai, and N. Urakami: *Microdomain formation in model biomembranes.* Physica B-Condensed Matter, 385:821–823, 2006.

Mazzanti, G., S. E. Guthrie, E. B. Sirota, A. G. Marangoni, and S. H. J. Idziak: *Orientation and phase transitions of fat crystals under shear.* Crystal Growth & Design, 3(5):721–725, 2003.

Mazzanti, G., A. G. Marangoni, and S. H. J. Idziak: *Modeling phase transitions during the crystallization of a multicomponent fat under shear.* Physical Review E, 71(4), 2005.

Mehrle, Y. E.: *Solidification and contraction of confectionery systems in rapid cooling processing.* PhD thesis, Diss. ETH Zurich No. 15546, Laboratory for Food Process Engineering, 2007.

Miura, A., A. Kusanagi, S. Kobayashi, S. Tokairin, and Z. Jin: *Effect of static magnetic field on crystallization of triacylglycerols.* IEEE Transactions on Applied Superconductivity, 14(2):1588–1591, 2004.

Mui, B., L. Chow, and M. J. Hope: *Extrusion technique to generate liposomes of defined size.* Methods in Enzymology, 367:3–14, 2003.

Nagle, J. F. and S. Tristram-Nagle: *Structure of lipid bilayers.* Biochimica et Biophysica Acta-Reviews on Biomembranes, 1469(3):159–195, 2000.

Nieh, M. P., C. J. Glinka, S. Krueger, R. S. Prosser, and J. Katsaras: *SANS study of the structural phases of magnetically alignable lanthanide-doped phospholipid mixtures.* Langmuir, 17(9):2629–2638, 2001.

Nieh, M. P., C. J. Glinka, S. Krueger, R. S. Prosser, and J. Katsaras: *SANS study on the effect of lanthanide ions and charged lipids on the morphology of phospholipid mixtures.* Biophysical Journal, 82(5):2487–2498, 2002.

Ono, A., K. Takeuchi, A. Sukenari, T. Suzuki, I. Adachi, and M. Ueno: *Reconsideration of drug release from temperature-sensitive liposomes.* Biological & Pharmaceutical Bulletin, 25(1):97–101, 2002.

Ottiger, M. and A. Bax: *Bicelle-based liquid crystals for NMR-measurement of dipolar couplings at acidic and basic pH values.* Journal of Biomolecular NMR, 13(2):187–191, 1999.

Pencer, J., T. Mills, V. Anghel, S. Krueger, R. M. Epand, and J. Katsaras: *Detection of submicron-sized raft-like domains in membranes by small-angle neutron scattering.* European Physical Journal E, 18(4):447–458, 2005a.

Pencer, J., M. P. Nieh, T. A. Harroun, S. Krueger, C. Adams, and J. Katsaras: *Bilayer thickness and thermal response of dimyristoylphosphatidylcholine unilamellar vesicles containing cholesterol, ergosterol and lanosterol: A small-angle neutron scattering study.* Biochimica et Biophysica Acta-Biomembranes, 1720(1-2):84–91, 2005b.

Pencer, J., V. N. P. Anghel, N. Kucerka, and J. Katsaras: *Scattering from laterally heterogeneous vesicles. III. Reconciling past and present work.* Journal of Applied Crystallography, 40:771–772, 2007.

Pencer, J., A. Jackson, N. Kucerka, M. P. Nieh, and J. Katsaras: *The influence of curvature on membrane domains.* European Biophysics Journal with Biophysics Letters, 37(5):665–671, 2008.

Peschar, R., M. M. Pop, D. J. A. De Ridder, J. B. van Mechelen, R. A. J. Driessen, and H. Schenk: *Crystal structures of 1,3-distearoyl-2-oleoylglycerol and cocoa butter in the beta(V) phase reveal the driving force behind the occurrence of fat bloom on chocolate.* Journal of Physical Chemistry B, 108(40):15450–15453, 2004.

Prosser, R. S., J. A. Losonczi, and I. V. Shiyanovskaya: *Use of a novel aqueous liquid crystalline medium for high-resolution NMR of macromolecules in solution.* Journal of the American Chemical Society, 120(42):11010–11011, 1998a.

Prosser, R. S., V. B. Volkov, and I. V. Shiyanovskaya: *Novel chelate-induced magnetic alignment of biological membranes.* Biophysical Journal, 75(5):2163–2169, 1998b.

Prosser, R. S., V. B. Volkov, and I. V. Shiyanovskaya: *Solid-state NMR studies of magnetically aligned phospholipid membranes: taming lanthanides for membrane protein studies.* Biochemistry and Cell Biology-Biochimie et Biologie Cellulaire, 76 (2-3):443–451, 1998c.

Qiu, X. X., P. A. Mirau, and C. Pidgeon: *Magnetically induced orientation of phosphatidylcholine membranes.* Biochimica et Biophysica Acta, 1147(1):59–72, 1993.

Reinl, H., T. Brumm, and T. M. Bayerl: *Changes of the physical-properties of the liquid-ordered phase with temperature in binary-mixtures of DPPC with cholesterol - a H-2-NMR, Ft-Ir, DSC, and Neutron-Scattering Study.* Biophysical Journal, 61 (4):1025–1035, 1992.

Sanders, C. R. and J. H. Prestegard: *Magnetically orientable phospholipid-bilayers containing small amounts of a bile-salt analog, chapso.* Biophysical Journal, 58(2): 447–460, 1990.

Sanders, C. R. and R. S. Prosser: *Bicelles: a model membrane system for all seasons?* Structure, 6(10):1227–1234, 1998.

Sandstrom, M. C., E. Johansson, and K. Edwards: *Influence of preparation path on the formation of discs and threadlike micelles in DSPE-PEG(2000)/lipid systems.* Biophysical Chemistry, 132:97–103, 2008.

Scholz, F., E. Boroske, and W. Helfrich: *Magnetic-anisotropy of lecithin membranes - a new anisotropy susceptometer.* Biophysical Journal, 45(3):589–592, 1984.

Seifert, U.: *Curvature-induced lateral phase segregation in 2-component vesicles.* Physical Review Letters, 70(9):1335–1338, 1993.

Simon, M. D. and A. K. Geim: *Diamagnetic levitation: Flying frogs and floating magnets (invited).* Journal of Applied Physics, 87(9):6200–6204, 2000.

Soong, R. and P. M. Macdonald: *Diffusion of PEG confined between lamellae of negatively magnetically aligned bicelles: Pulsed field gradient H-1 NMR measurements.* Langmuir, 24(2):518–527, 2008.

Stapley, A. G. F., H. Tewkesbury, and P. J. Fryer: *The effects of shear and temperature history on the crystallization of chocolate.* Journal of the American Oil Chemists Society, 76(6):677–685, 1999.

Tenforde, T. S. and R. P. Liburdy: *Magnetic deformation of phospholipid-bilayers - effects on liposome shape and solute permeability at prephase transition-temperatures.* Journal of Theoretical Biology, 133(3):385–396, 1988.

Torchilin, V. P., V. Weissig, F. J. Martin, T. D. Heath, and R. R. C. New: *Liposomes: A Practical Approach, Second Edition.* Torchilin, V. P. and Weissig, V., 2003.

Triba, M. N., D. E. Warschawski, and P. F. Devaux: *Reinvestigation by phosphorus NMR of lipid distribution in bicelles.* Biophysical Journal, 88(3):1887–1901, 2005.

Triba, M. N., P. F. Devaux, and D. E. Warschawski: *Effects of lipid chain length and unsaturation on bicelles stability. A phosphorus NMR study.* Biophysical Journal, 91(4):1357–1367, 2006.

Tristram-Nagle, S., Y. F. Liu, J. Legleiter, and J. F. Nagle: *Structure of gel phase DMPC determined by X-ray diffraction.* Biophysical Journal, 83(6):3324–3335, 2002.

Vacklin, H. P., F. Tiberg, and R. K. Thomas: *Formation of supported phospholipid bilayers, via co-adsorption with beta-D-dodecyl maltoside.* Biochimica et Biophysica Acta-Biomembranes, 1668(1):17–24, 2005.

Dam, L. van, G. Karlsson, and K. Edwards: *Direct observation and characterization of DMPC/DHPC aggregates under conditions relevant for biological solution NMR.* Biochimica et Biophysica Acta-Biomembranes, 1664(2):241–256, 2004.

Dam, L. van, G. Karlsson, and K. Edwards: *Morphology of magnetically aligning DMPC/DHPC aggregates-perforated sheets, not disks.* Langmuir, 22(7):3280–3285, 2006.

Veatch, S. L. and S. L. Keller: *Lateral organization in model lipid membranes containing cholesterol.* Molecular Biology of the Cell, 13:359–359, 2002.

Wakayama, N. I.: *Effects of a strong magnetic field on protein crystal growth.* Crystal Growth & Design, 3(1):17–24, 2003.

Walde, P. and S. Ichikawa: *Enzymes inside lipid vesicles: Preparation, reactivity and applications.* Biomolecular Engineering, 18(4):143–177, 2001.

Wang, H., M. Eberstadt, E. T. Olejniczak, R. P. Meadows, and S. W. Fesik: *A liquid crystalline medium for measuring residual dipolar couplings over a wide range of temperatures.* Journal of Biomolecular NMR, 12(3):443–446, 1998.

Whiles, J. A., K. J. Glover, R. R. Vold, and E. A. Komives: *Methods for studying transmembrane peptides in bicelles: Consequences of hydrophobic mismatch and peptide sequence.* Journal of Magnetic Resonance, 158(1-2):149–156, 2002.

Windhab, E. J.: *New developments in crystallization processing.* Journal of Thermal Analysis and Calorimetry, 57(1):171–180, 1999.

Yamaguchi, M. and Y. Tanimoto: *Magneto-Science.* Springer, 2006.

Yanagisawa, M., M. Imai, T. Masui, S. Komura, and T. Ohta: *Growth dynamics of domains in ternary fluid vesicles.* Biophysical Journal, 92(1):115–125, 2007.

Zeng, Y.: *Impf- und Scherkristallisation von Schokoladen.* PhD thesis, Diss. ETH Zurich No. 13798, Laboratory for Food Process Engineering, 2000.

Curriculum Vitae

Paul Beck

date of birth	March, 29, 1979
place of birth	Thalwil/ZH
citizen of	Switzerland and France

2004-2009	Ph.D. student and research assistant at the Laboratory of Food Process Engineering, ETH Zurich, Switzerland
2005-2007	Post graduate studies: Master of Advanced Studies in Management, Technology, and Economics/BWI (MAS MTEC) at ETH Zurich Diploma thesis at Chocolats Heidi, Bucharest/Romania: Optimization of warehouse management and order handling
1999-2004	Graduate studies in Food Science and Technology at ETH Zurich Diploma thesis: Production of 3-hydroxypropionaldehyde using free and immobilized cells of Lactobacillus reuteri
	Industrial placements for several months: -George Fischer Piping Systems, Kingsgrove/Australia -Coop Panofina, Wallisellen -Wander AG, Neuenegg
1995-1999	Kantonsschule Baden
1996-1997	High school exchange year in Nebraska City, NE, USA